CHALMERS
UNIVERSITY OF TECHNOLOGY

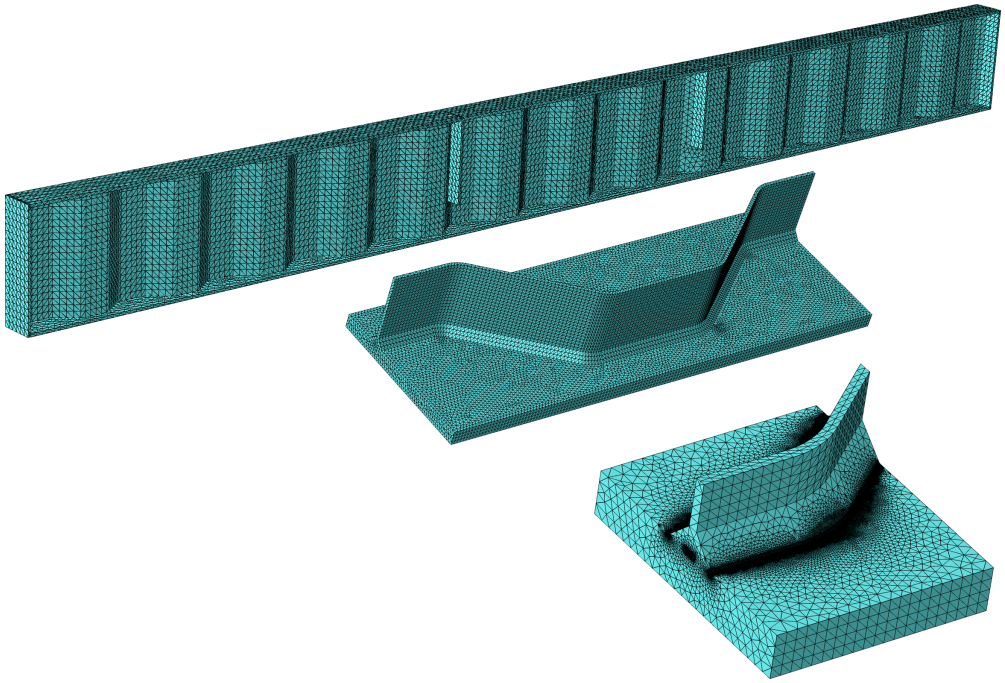

Fatigue Strength of Bridge Girders with Corrugated Web

Master's thesis in Master Program Structural engineering and Building technology

ALICE EMME
ELSA SVENSSON

Department of Architecture and Civil Engineering
CHALMERS UNIVERSITY OF TECHNOLOGY
Master's thesis ACEX30
Gothenburg, Sweden 2024

Master's thesis ACEX30

Fatigue Strength of Bridge Girders with Corrugated Web

ALICE EMME
ELSA SVENSSON

CHALMERS
UNIVERSITY OF TECHNOLOGY

Department of Architecture and Civil Engineering
Division of Structural Engineering
Light Weight Structures Group
Chalmers University of Technology
Gothenburg, Sweden 2024

Fatigue Strength of Bridge Girders with Corrugated Web
ALICE EMME
ELSA SVENSSON

Supervisor: PhD student Fatima Hlal, Department of Architecture and Civil Engineering
Examiner: Professor Mohammad Al-Emrani, Department of Architecture and Civil Engineering

Department of Architecture and Civil Engineering
Division of Structural Engineering
Light Weight Structures Group
Chalmers University of Technology
SE-412 96 Gothenburg
Telephone +46 31 772 1000

Cover: Contour plot of global-, structural hot-spot stress- and effective notch stress model meshed.

Typeset in LaTeX
Department of Architecture and Civil Engineering
Gothenburg, Sweden 2024

Fatigue Strength of Bridge Girders with Corrugated Web
ALICE EMME
ELSA SVENSSON
Department of Architecture and Civil Engineering
Division of Structural Engineering
Light Weight Structures Group
Chalmers University of Technology

Abstract

Corrugated steel web girders are emerging as a potential choice for bridge construction due to their material-saving advantages. Fatigue frequently causes failure in constructions subjected to cyclic loading, such as bridges. However, thus far, the Eurocode has not addressed the fatigue strength of bridge girders with corrugated webs, particularly the welding detail between the web and the flange. This thesis thereby investigates the fatigue life of the flange-to-web weld detail in these girders, employing local approaches such as structural hot-spot stress and effective notch stress method. The objective is to compare the results obtained from these local approaches with those derived from the nominal stress method. Subsequently, a fatigue strength class is recommended for each design approach. Moreover, the effect of various corrugation parameters such as the corrugation angle and bending radius on the fatigue life of corrugated web girders have been examined.

The Master's thesis began by collecting data from previous fatigue experiments conducted on corrugated web girders. Specimens identical to the experiment have been modelled in Abaqus for a numerical analysis investigating the nominal-, structural hot-spot- and effective notch stress for all specimens. To simulate the structural behaviour of the experimental girders, a mesh convergence and validation study have been performed separately on each of the specimens. The FE modelling has been described and further results derived.

Based on the results of the numerical analysis the nominal-, structural hot-spot- and effective notch stresses have been compared against each other. Concluding that a decrease in the scatter appears when using structural hot-spot stress compared to the nominal stress method. However, looking at the effective notch stress the scatter increased again. Further, a proposal of the detail category for each stress method has been presented. Lastly, the geometric parameters including corrugation angle and bending radius, have been analyzed. Based on the results, the conclusion was that the corrugation angle's geometrical effects are more considerable compared to the bending radius.

Keywords: Corrugated web, Fatigue, Fatigue life, Nominal stress, Structural hot-spot stress, Effective notch stress, Corrugation angle, Bending radius

Utmattningskapacitet hos stålbalkar med korrugerad livplåt
ALICE EMME
ELSA SVENSSON
Institution för Arkitektur och Samhällsbyggnadsteknik
Konstruktionsteknik och Byggnadsteknologi
Lättviktskonstruktioner
Chalmers Tekniska Högskola

Sammanfattning

Tack var de korrugerade livplåts balkarnas material besparande fördelar förekommer dessa mer och mer som ett potienellt val i brokonstruktioner idag. Broar utsätts ständigt för cyklisk belastning som ger upphov till utmattningsbrott i konstruktionen. Däremot, har inte Eurocode någon information om utmattningskapaciteten på balkar med korrugerad livplåt, och speciellt svetsen mellan livplåten och flänsen. Mastersuppsatsen undersöker därmed utmattningskapaciteten av svetsen mellan livet och flänsen hos dessa balkar med hjälp av de lokala metoderna strukturell hot-spot och “effective notch stress” metoden. Målet är att jämföra resultaten erhållna från dessa lokala metoder med resultaten från nominella stress metoden. Därefter rekommenderas en detaljkategori för varje spänningsmetod. Dessutom, kommer effekten av korrugeringsvinkel och böjradie på utmattningskapaciteten för korrugerade livplåts balkar undersökas.

Mastersuppsatsen började med att samla in data från tidigare utmattningsexperiment utförda på korrugerad livplåts balkar. Identiska balkar från experimenten har modellerats i Abaqus för en numerisk analys som undersöker den nominella, strukturella hot-spot- och "effective notch stress” metoden för samtiliga experiment. Med en konvergensstudie och valideringsstudie som utförts separat på varje experiment har det strukturella beteendet hos balkarna efterliknats. FE-modelleringen har beskrivits och resultat har framtagits.

Baserat på resultaten som framtagits från den numeriska analysen har spänningen från den nominella, strukturella hot-spot- och "effective notch stress” metoden jämförts med varandra. En minskning av spridningen uppkom vid användning av den strukturella hot-spot-spänning- i jämförelse med den nominella spänningsmetoden. Däremot, framkom det att spridningen från "effective notch stress” metoden ökade igen. Dessutom har ett förslag på detaljkategori angetts för varje spänningsmetod. Även de geometriska parametrarna; korrugeringsvinkel och böjradie, har analyserats. Där det visade sig att korrugeringsvinkeln har en större påverkan på utmattningskapaciteten i jämförelse med böjradien.

Nyckelord: Korrugerad livplåt, Utmattning, Utmattningskapacitet, Nominell spänning, Strukturell hot-spot metoden, "Effective notch stress" metoden, Korrugeringsvinkel, Böjradie

Acknowledgements

This Master's thesis is performed at Chalmers University of Technology, Department of Architecture and Civil Engineering and Light Weight Structures. The thesis has been carried out between January to June 2024, and the majority of the work has been performed at Chalmers.

This project would not have been possible without the support of many people. First we would like to thank our supervisor PhD candidate Fatima Hlal for guidance and support throughout the project. You have shown great interest and involvement by being available and quickly answering our questions. Further you, have been giving us clear descriptions and support in the FE-modeling.

We would also like to thank our supervisor and examiner Prof. Mohammad Al-Emrani for your enthusiasm and support. Through you we have received deeper knowledge regarding fatigue and your insightful comments have made us more curios and interested in the subject.

It has been such a great time working with you guys, thank you for everything.

Lastly, we would like to thank our opponent and friend Rauan Al-Emrani for great feedback during the project. We would also like to thank our friends for enjoyable lunch breaks during the spring.

Gothenburg, June 2024
Alice Emme and Elsa Svensson,

Contents

List of Figures

List of Tables

Nomenclature

Glossary

CAFL - Constant Amplitude Fatigue Limit
CW - Corrugated web
CWG - Corrugated web girder
CWT - Corrugated web T-shaped specimen
DC - Detail category
ENS - Effective Notch Stress method
FAT - Stress range at $2 \cdot 10^6$ million cycles
FE - Finite Element
FEA - Finite Element analysis
FEM - Finite Element method
FW - Flat web
GWAM - Gas Metal Arc Welding
IIW - International Institute of Welding
OFAT - One Factor At a Time
S-N curve - Stress-Fatigue life curve
S-point - Stress-point
SCF - Stress concentration factor
SHSS - Structural Hot-Spot Stress method
STD - Standard deviation
TW - Trapezoidal web

Greek letters

α - Inclined angle between the flange and horizontal axis
$\Delta\sigma_{nom}$ - Nominal stress range
$\Delta\sigma_R$ - Normal stress fatigue strength
$\Delta\sigma_x$ - Normal stress
$\Delta\tau_R$ - Shear stress fatigue strength
$\Delta\tau_{xy}$ - Shear stress
θ - Corrugation angle
σ - Stress
$\sigma_{0.4t}$ - Stress at reference point 0.4t
$\sigma_{0.9t}$ - Stress at reference point 0.9t
$\sigma_{1.0t}$ - Stress at reference point 1.0t
$\sigma_{1.4t}$ - Stress at reference point 1.4t
σ_{11} - Stress component in x-direction
$\sigma_\perp$ - Perpendicular stress component
σ_{bend} - Bending stress
σ_{ENS} - Stress from investigated area from ENS-model
σ_{global} - Stress from investigated area in global model
σ_{nom} - Nominal membrane stress
σ_{notch} - Notch stress
σ_{SHSS} - Structural Hot-spot stress

Roman letters

A - Cross section area
C - Non-dimensional factor for different corrugation shapes
D - Damage
L_0 - Effective length
M - Bending moment
M_t^{corr} - Transverse bending moment from C-factor method
M_t^{sin} - Transverse bending moment for sinusoidal corrugated web
$M_{z,max}$ - Maximum transverse bending moment
N - Axial force
R - Bending radius
S_{11} - Longitudinal stress component in x-direction in the global coordinate system
S'_{11} - Longitudinal stress component in x-direction in the local coordinate system
S'_{12} - Shear stress in the local coordinate system
$S_{principal}$ - Maximum principal stress
$S_{VonMises}$ - von Mises stress
$U3$ - Deflection in z-direction
V_z - Shear force
W - Bending resistance

a_0 - Edge fold length
a_1 - Parallel fold length
a_2 - Inclined fold length
a_3 - Corrugation depth
a_4 - Projected length along horizontal axis
a_{max} - Maximum value between the edge fold and inclined fold
a_w - Weld throat thickness
$b_{f,bottom}$ - Bottom flange width
$b_{f,top}$ - Top flange width
h_w - Web height
l_{eff} - Effective length of the girder
n - Number of corrugation waves
p_y - Uniformly distributed load
r - Effective notch radius
$t_{f,bottom}$ - Bottom flange thickness
$t_{f,top}$ - Top flange thickness
t_w - Web thickness
z - Position of the cross section along z-axis

1 Introduction

In this chapter, the background, aim and objective, methodology and limitations for this Master's thesis will be presented.

1.1 Background

The development of bridge girders has resulted in the need for increased stiffness and buckling resistance to obtain more durable structures while optimizing the material usage. A possible way to achieve increased out-of-plane stiffness and shear capacity is the use of corrugated webs instead of conventional stiffened plate girders. With regards to the corrugation, the web can both be deeper and have reduced thickness without the need for stiffeners, which makes the corrugated web beams more material efficient. Beams with corrugated webs offer the potential to attain the desired structural capacity with less use of materials. The weight for the corrugated web girders can be reduced by 30% (Ibrahim et al., 2006a). Therefore, the beam with corrugated web is of interest in bridge design.

Despite all the advantages mentioned, there is a lack of information regarding the fatigue behaviour of corrugated web girders in the design standards. Chenung and Li (2003) mention that in general, 80-90% of metal structural failure are caused by fatigue. Despite the risk of fatigue failure, the fatigue strength of bridge girders with corrugated web is unexplored in the current design standard (EN1993-1-9, 2005). The fatigue strength of corrugated web girder is expected to be a function of the corrugation parameters and the nominal stress. Getting insight into the effect of the corrugation parameter and the load effects to derive one (or multiple) fatigue detail categories for the web-to-flange weld detail is of high importance for the design procedure of this type of bridge girders. Therefore, the local approaches, including structural hot-spot stress- and effective notch stress methods are of interest.

1.2 Aim and Objective

This Master's thesis aims to evaluate the fatigue strength of the welding detail between the web and the flange of bridge girders with corrugated web. Based on previous laboratory experiments, a numerical analysis have been employed to evaluate the nominal stress method and the local approaches; structural hot-spot stress- and effective notch stress method. Through these methods, the following questions will be examined:

- What detail category can be used for corrugated web girders?
- What is the effect on fatigue strength from various corrugation parameters such as the corrugation angle and bending radius?
- Which of the three stress methods nominal stress, structural hot-spot stress method, or effective notch stress method is the most representative of the fatigue life of corrugated web girders?

The objective of this thesis is to compare the results obtained from the local approaches with the result derived from the nominal stress method.

1.3 Methodology

The Master's thesis began with a literature study to research the "state-of-the-art" regarding the subject of corrugated web girders and fatigue. Henceforth gain more knowledge of the different fatigue design methods nominal stress- and local approaches; structural hot-spot stress- and effective notch stress method.

Furthermore, previous data from fatigue experiments and numerical analyses performed on beams with corrugated webs has been gathered and analysed. Some of the experimental girders have been further investigated through a numerical analysis using the finite element software Abaqus. The stress methods including nominal stress-, structural hot-spot stress- and effective notch stress methods were investigated and compared. The result of the numerical analysis is presented and further discussed. The conclusions are then stated from the results.

1.4 Limitations

The limitations of this Master's thesis are that a specific welded detail has been analysed, the weld between the corrugated web and the bottom flange. The girders have been subjected to fatigue loads acting on bridges. The application of the suggested detail categories at the end is limited to the studied parameters included in the previously conducted tests.

2 Literature study

The corrugated web concept originated in 1920. Due to the shear resistance of the corrugated web, this concept provides an economical structural solution for bridges (Rodriguez, 2000). The following chapter contains the "state-of-the-art" where deeper knowledge about the corrugated web girders is discussed. Further, the topic of fatigue is presented and how these methods can be implemented on the corrugated web girders.

2.1 Introduction to fatigue

When designing steel girders today, both static- and dynamic loading have been taken into account. Even though the steel structure can withstand all the static loads, the risk of failure is possible due to fatigue. 80-90% of metal structural failures are caused by fatigue (Chenung & Li, 2003). The sudden failure associated with fatigue leads to catastrophic accidents and substantial economic losses (Al-Emrani, 2023).

As mentioned above, it is crucial to validate fatigue for steel structures. Fatigue failure can be described as a permanent local change in the material that is subjected to various stresses and strains, which consequently can lead to formation of cracks or fracture. These fatigue cracks start at a detail in the girder where the stress is significantly larger. The geometric stress concentrations appear where the stress flow is disturbed due to a change in the geometry. Welding is a typical detail where stress concentrations appear in the structure since they both contain local stress raisers like weld defects and residual stresses from the welding process. Even though weld defects are not considered in fatigue analyses, the welded details are the areas where stress concentrations often occur and the detail where the fatigue analysis should be investigated (Al-Emrani, 2023).

Guidance on how to investigate the fatigue behaviour of a steel structure can be found in Eurocode, (EN1993-1-9, 2005) and the international association named International Institute of Welding (IIW) (Jonsson et al., 2016). For each detail, the relevant fatigue strength is obtained for different detail categories. These detail categories further generate S-N curves which together with the range of stress concentration present the number of cycles to failure, and following the fatigue life of the detail can be obtained (Al-Emrani, 2023).

2.2 Introduction to corrugated web for bridge girders

The advantages that corrugated web geometry entails have been used in bridge construction since 1980 in Europe and Japan (Abbas et al., 2007a). Using corrugating results in increased out-of-plane stiffness and shear capacity of the web. Besides the structural performance, this has resulted in the web being higher and having a reduced thickness. The bridge girders are constantly exposed to loads varying regularly or stochastically in time during a large number of cycles, which consequently leads to the emergence of fatigue failure (Eriksson, 2010). Therefore, this section contains an analysis of the fatigue behaviour of the girders, more specifically the weld between the lower flange and the corrugated web.

2.2.1 Corrugations shapes

The corrugation in the web is made mainly in two different shapes, including sinusoidal and trapezoidal. The difference between the sinusoidal and trapezoidal geometry is the wave shape which can affect the emergence of stress concentrations. A sinusoidal-shaped corrugation has a smooth transition between the waves, while a trapezoidal-shaped corrugation has waves composed of parallel and inclined folds. Figure 2.1 presents the trapezoidal corrugation, along with the parameters mentioned below. Other corrugation shapes, such as triangular and rectangular corrugation, are also common, as shown in the same figure.

The parameters that influence the structural behavior of the girder are the following;

h_w, web height
t_w, web thickness
a_w, weld throat thickness
$t_{f,top}$, top flange thickness
$b_{f,top}$, top flange width
$t_{f,bottom}$, bottom flange thickness
$b_{f,bottom}$, bottom flange width

Especially for the trapezoidal corrugation the following parameters are used to describe the geometry;

θ, corrugation angle
a_1, parallel fold length
a_2, inclined fold length
a_3, corrugation depth
a_4, projected length of the inclined fold along horizontal axis
R, bending radius
L_0, effective length

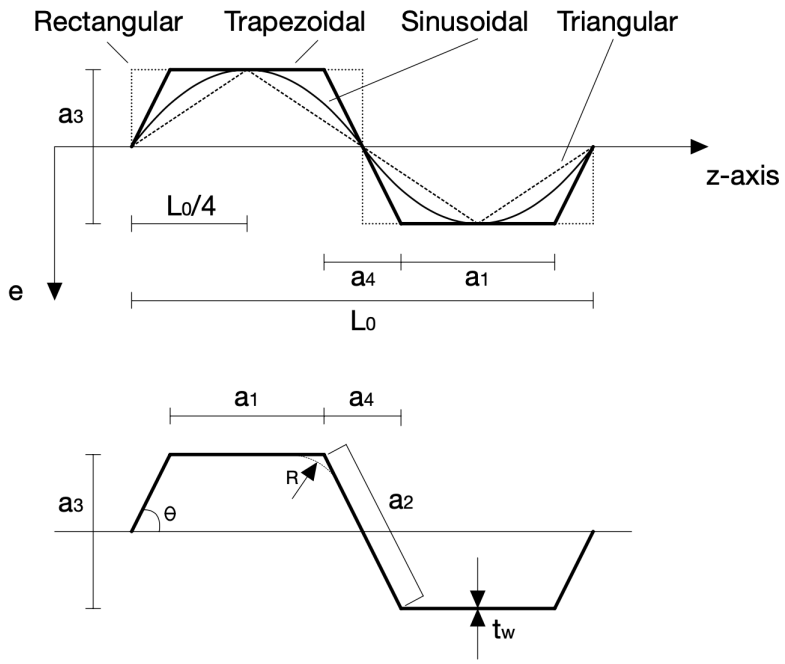

Figure 2.1: *Different corrugation profiles.*

2.2.2 Stress distribution and transverse bending

The geometry of the corrugated web (CW) affects the moment distribution from different loading conditions. The girder with corrugated web loaded with in-plane bending and shear will both deflect in-plane and twist out-of-plane (Abbas et al., 2007a). Therefore, the girder obtains a moment distribution from the in-plane loading and the transverse bending of the flange. However, a girder with CW subjected to axial loading does not carry any notable axial stresses (Abbas et al., 2007a). Therefore, the web contribution to the bending capacity can be neglected. It is assumed that the bending moment is carried by the flanges only. This behaviour of the corrugated web is known as the "accordion effect".

The stress distribution in the girder with corrugated web occurs from in-plane bending and out-of-plane twisting of the girder (Abbas et al., 2007a). The entire stress state in the corrugated web girder can be determined by super-positioning of the stresses due to in-plane bending, transverse bending due to shear flow and out-of-plane local transverse bending due to uneven web contribution to the normal stresses. The in-plane behavior can be treated by conventional beam theory while the out-of-plane twisting is considered as a flange transverse bending problem.

As a result of the shear force in the CW at the shear zone, a shear flow occurs in the flanges and affects the bending moment resistance. The shear flow in the CW generates additional normal stresses in the flanges and the direction of the shear flow follows the corrugation of the web, see Figure 2.2.

In order to analyse the transverse bending moment for corrugated web girders with piecewise folds (trapezoidal, rectangular, triangular, etc.) Abbas et al. (2007b) present a method to consider this phenomenon, the fictitious load method. In this method, a fictitious transverse load is applied to the flange, which results in transverse shear and transverse bending. This method confirmed the experimental results regarding the behaviour of the flange subjected to transverse bending (Abbas et al., 2007b). With the fictitious load method, each flange can be analysed using conventional beam theory.

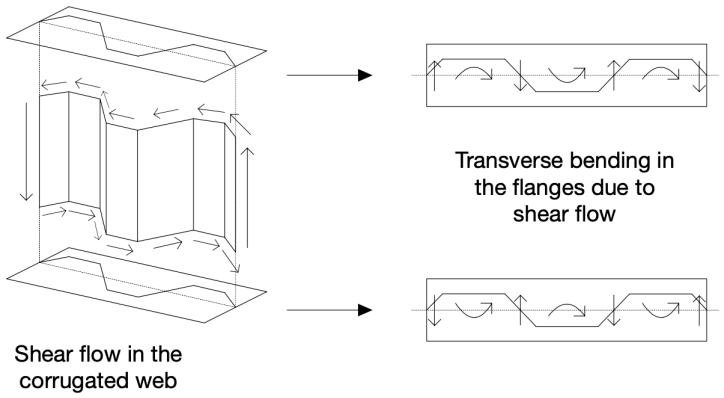

Figure 2.2: *Shear flow in the flanges and flanges analysed with conventional beam theory.*

The in-plane behaviour is treated using the conventional beam theory, while the twisting behaviour is considered with flange transverse bending. In order to determine the transverse bending moment, the trapezoidal corrugated web is replaced by a sinusoidal corrugated web (Abbas et al., 2007b). In the case of uniformly distributed load, an analytical solution is given by Equation 2.1.

$$M_t^{sin} = \frac{p_y \cdot L_0^2 \cdot a_3}{2 \cdot h_w} \cdot \{\frac{1}{\Pi^2} \cdot [(1 - 2 \cdot \frac{z}{L_0}) \cdot \Pi \cdot c_\xi + 2 \cdot s_\xi + (\Pi \cdot c_\Pi - 2 \cdot s_\Pi + \Pi) \cdot \frac{z}{L_0} - \Pi]\} \tag{2.1}$$

where,

p_y , uniformly distributed load	Π , $2 \cdot \pi \cdot n$
L_0 , span of the girder	c_ξ , $\cos(2 \cdot \pi \cdot n \cdot \frac{z}{L_0})$
a_3 , corrugation depth	c_Π , $\cos(2 \cdot \pi \cdot n)$
h_w , web height	s_ξ , $\sin(2 \cdot \pi \cdot n \cdot \frac{z}{L_0})$
n , number of corrugation waves	s_Π , $\sin(2 \cdot \pi \cdot n)$
z , position of the cross section along the z-axis	

In order to determine the transverse bending moment for other corrugations Abbas et al. (2007b) introduced a simplified analytical method called the C-factor method. This method was developed based on the combination of the principle of virtual work and the fictitious load method. The relationship between the transverse bending moment of the flange is directly related to the geometry of the corrugated web and an accumulated area function. The ratio of the area under one half wave of a given corrugation profile and a sinusoidal profile, with the same wavelength and corrugation depth results in a non-dimensional factor C. This C-factor is applied according to Equation 2.2, and converts the transverse bending moment for other corrugations. In Table 2.1 the different C-factors for each corrugation are presented.

$$M_t^{corr} = C \cdot M_t^{sin} \tag{2.2}$$

Table 2.1: *C-factor for web corrugations (Abbas et al., 2007b).*

Corrugation	Area under half a wavelength, $\int_0^{L_0} e\,dz$	C-factor
Sinusoidal	$\frac{a_3 L_0}{2\pi}$	1
Trapezoidal	$\frac{a_3}{2}[a_1 + a_4/2]$	$\pi[\frac{a_1+a_4/2}{L_0}]$
Triangular	$\frac{a_3 L_0}{8}$	$\pi/4$
Rectangular	$\frac{a_3 L_0}{4}$	$\pi/2$

The transverse bending moment is a result from the shear flow in the corrugated web. Where the inclined part of the web intersects with the z-axis (Figure 2.3) the maximum transverse bending moment, $M_{z,max}$ occurs (Baláž & Koleková, 2012). Baláž and Koleková studied the transverse bending of CW beams in 2012, based on their analysis the authors derived the approximated formula for $M_{z,max}$ given by Equation 2.3.

$$M_{z,max} = \frac{V_z}{4h_w} \cdot a_3 \cdot (2a_{max} + a_4) \tag{2.3}$$

where, $a_{max} = max(a_0, a_1)$.

This formula was developed to facilitate the design of corrugated web girders in Eurocode 3.

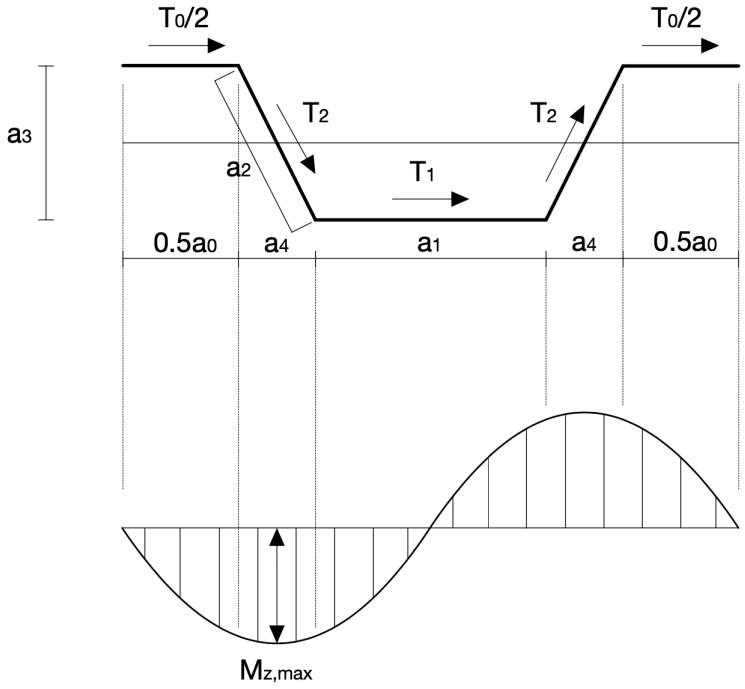

Figure 2.3: *Maximum transverse bending from shear flow.*

Kövesdi et al. (2012) performed a numerical study and compared it to the previous design method implemented in Eurocode (EN1993-1-5, 2006), to develop an enhanced method to determine the transverse bending moment from the shear flow in the corrugated web. The flange is assumed to be a beam loaded in bending, shear and normal forces originating from the shear flow. For the girder to be in equilibrium the web should start and end with an inclined fold consisting of a full number of wavelengths in between the two ends (Kövesdi et al., 2012). In the study, four different girder geometries, support and loading conditions were analysed. The most unfavourable combination was a girder with support and loading at the middle of the inclined fold with full corrugation waves between the support and loading points. Based on the numerical results compared to results obtained from Baláž and Kalekovás equation (Equation 2.3) it was noted that the transverse bending moment could be the double value in the most unfavourable case. Kövesedi et al. (2012) then proposed Equation 2.4 to enhance previous design method.

$$M_{z,max} = \frac{V_z}{2h_w} \cdot a_3 \cdot (2a_1 + a_4) \tag{2.4}$$

The equation was derived from the shear flow in Figure 2.4. Firstly, the equation for the bending moment at the point in the middle of the inclined fold was derived and then simplified resulting in Equation 2.4 (Kövesdi et al., 2012).

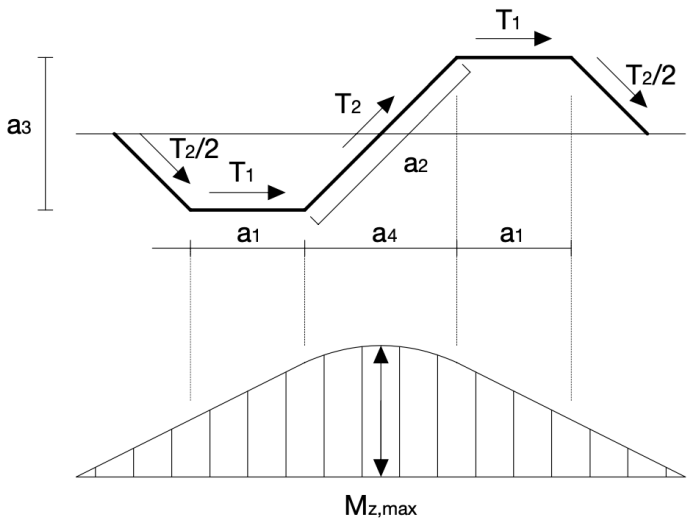

Figure 2.4: *Maximum transverse bending from shear flow for the most unfavourable case.*

The behaviour of the trapezoidal corrugated web differs from the conventional flat plate web due to its geometry. The out-of-plane stiffness increases as a result of the corrugation, however, the flexural in-plane stiffness is lower due to the accordion effect. Experimental and analytical studies have been performed that show a decrease in flexural capacity of 10-20% between flat web (FW) and trapezoidal web (TW) (Elamary et al., 2017). This indicates the accordion effect and the fact that the corrugated web has a negligible effect on the bending stiffness.

2.2.3 Fatigue strength of corrugated web girders

In order to increase the fatigue life of bridge girders, engineers have sought alternative designs for conventional methods. By using web corrugation instead of transverse stiffeners welded to the flange, the fatigue life can increase by 47% (Ibrahim et al., 2006b).

In Eurocode, there are many recommendations for how to calculate the fatigue life of standard steel details (EN1993-1-9, 2005). However, there is no information that covers the inclined fold weld that is placed between the flange and the web in a trapezoidal corrugated web girder. But it can be expected that the detail category (DC) for the inclined weld ends up between the DC125 for a longitudinal weld (Table 8.2 in (EN1993-1-9, 2005)) and DC80 for a transversal weld (Table 8.4 in (EN1993-1-9, 2005)), see Figure 2.5. More specific information about the DC can not be obtained from Eurocode but is instead derived analytically.

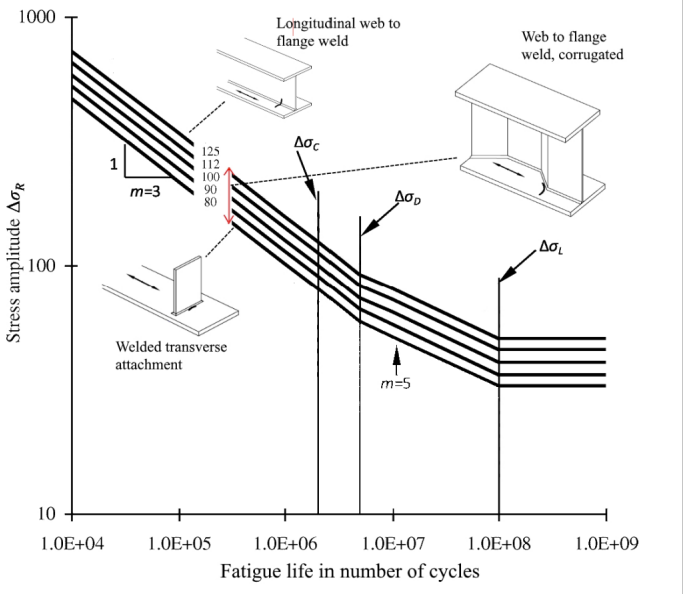

Figure 2.5: *S-N curves and detail category span of a corrugated web (Lindqvist & Nilsson, 2016).*

Save and Åkermo (2020) have, through numerical- and experimental analyses, obtained S-N curves that correspond to the inclined fold weld in corrugated web girders. They investigated whether the geometry and loading situation influence the stress concentration. By analyzing the geometric parameters like weld thickness, bending radius, and corrugation angle, an S-N curve with a fixed slope of 1:3, fulfilling a 95% confidence limit, was derived to represent the fatigue class. The DC120 was obtained for the inclined fold weld in corrugated web girders using the nominal stress method.

Using the nominal stress method and DC120 gives a conservative result, while other methods like the structural hot-spot stress method and the effective notch stress method should be used to calculate a more accurate stress and fatigue class of the detail (Save & Åkermo, 2020).

The location in the corrugated web girder where the stress concentration is significantly higher appears at the S-point (Stress-point). Through experimental analyses several authors (Ibrahim, 2001), (Wang et al., 2013b), (Kövesdi & Dunai, 2014) and (Xu et al., 2019) discovered that the fatigue crack usually initiates at the S-point. The S-point is located in the vicinity of the weld in the tension flange where the parallel and the inclined web fold connect. The fatigue crack initiates at the weld toe at the S-point and further propagates a short distance along the weld toe before it changes direction, moving perpendicular to the principal stress in the tensile flange (Anami et al., 2005), see Figure 2.6.

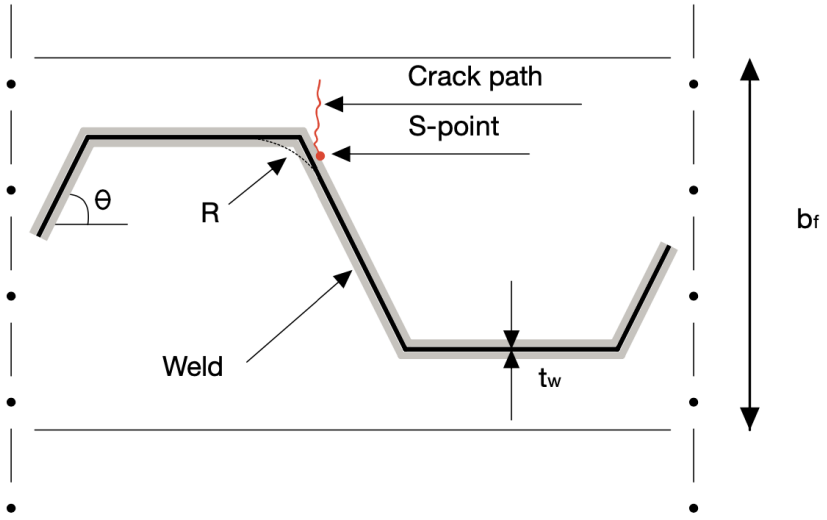

Figure 2.6: *S-point located in the fillet weld.*

2.3 Fatigue design methods

There are three different methods to use when designing the fatigue life; the nominal stress method and local approaches structural hot-spot stress (SHSS) and effective notch stress (ENS) method. Through all the methods, the goal is to find the stress concentration around the analysed detail and further obtain the fatigue life. The stress distribution in the vicinity of a welded connection depends on the direction of the applied load and the design of the detail. The main difference between the three methods is how the stress concentration is calculated. The effective notch stress method takes into account stress raisers due to micro geometry i.e., the notch effect. This means that ENS corresponds to reality the most, while in the nominal stress method, the stress used is simplified and an average stress is used. The SHSS method takes into account the stress raisers due to macro geometry, the shape of the detail. More information about the fatigue methods can be read in the following sections.

2.3.1 Nominal stress method

Al-Emrani (2023) explains that the definition of nominal stresses is the sum of bending and membrane stresses calculated in a structural detail. The nominal stress is the uniform stress distribution and having an abrupt change in the stress distribution results in a non-linear stress concentration. However, in the nominal stress method, these stress concentrations are not considered. Figure 2.7 presents the nominal stresses for a plate subjected to uniaxial tension. A discontinuity in the geometry such as notches, holes and welds etc., causes a disruption in the stress field and results in stress raisers in the vicinity of the geometrical discontinuity.

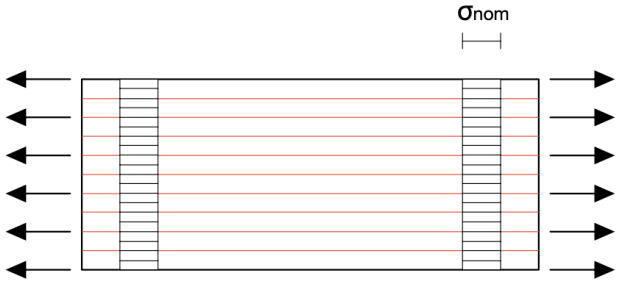

Figure 2.7: *Plate subjected to uniaxial tension presenting the nominal stress distribution.*

Assuming a detail subjected to axial tension and bending the nominal stress would be calculated using sectional constants, see Equation 2.5 and notations below.

$$\sigma_{nom} = \frac{N}{A} + \frac{M}{W} \tag{2.5}$$

N, axial force $[N]$
A, area $[m^2]$
M, bending moment $[Nm]$
W, bending resistance $[m^3]$

The calculation of the nominal stresses excludes the detail geometry, the weld and local stress raisers (Al-Emrani, 2023). In order to consider these effects, a relevant detail category is selected in Eurocode 3. The fatigue life is then determined based on the DC in the S-N curve (EN1993-1-9, 2005).

2.3.2 Structural Hot-spot stress method

The structural hot-spot stress method (SHSS) is another method used to evaluate the fatigue strength of a welded detail. Lindqvist and Nilsson (2016) mention that SHSS is preferred to be used when the geometry is very complex and the nominal stress is hard to estimate.

As mentioned in previous chapters, the stress distribution in the vicinity of a weld is non-linear, having a peak by the weld toe, see Figure 2.8. The stress distribution is composed of nominal membrane stresses (σ_{nom}), bending stresses (σ_{bend}) caused by the geometry, and non-linear notch stress (σ_{notch}) from local weld geometry. When calculating the SHSS, the non-linear notch stress is excluded by linearly or quadratically extrapolate the stresses at a predetermined distance, see Figure 2.10 (Al-Emrani & Aygül, 2014). The reason for excluding the non-linear stresses when calculating the SHSS is because it is hard to detect the exact welding geometry during the design phase (Akhlaghi, 2009).

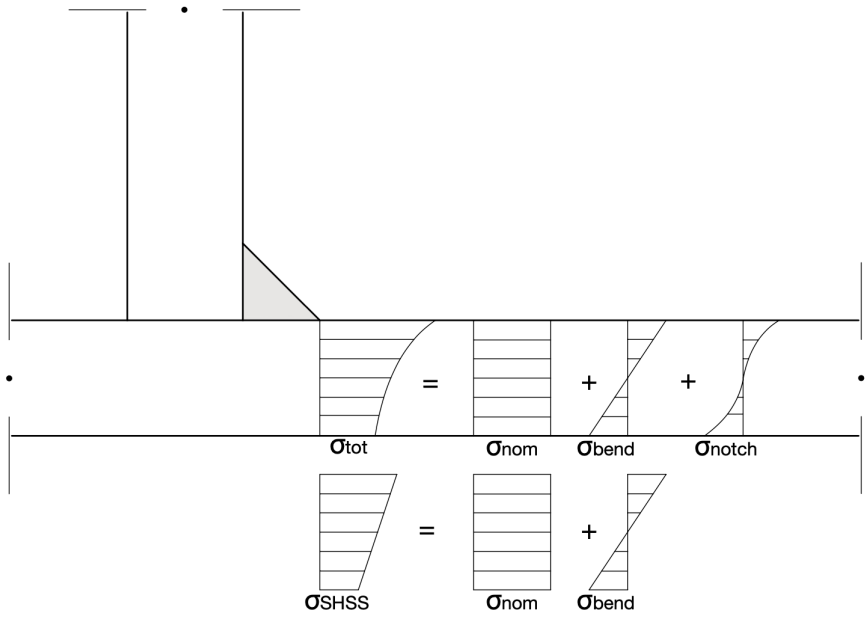

Figure 2.8: *Stress distribution by the weld toe and how hot-spot stresses is received.*

To reach the SHSS, Al-Emrani and Aygül (2014) emphasize that there are two different types of hot-spot appearances that need to be taken into account when analysing a weld detail: *Type a* and *Type b*, see Figure 2.9. The stress distribution in Type a varies through the thickness of the cracked plate, while the stress distribution in Type b are more uniform. This means that for Type a, the plate thickness should be considered when calculating the SHSS through linearization of the stresses. However, the plate thickness does not need to be considered for Type b.

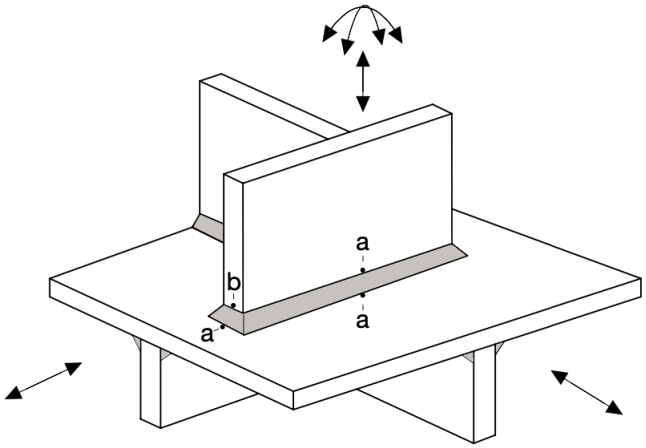

Figure 2.9: *Hot-spot appearances Type a and Type b.*

The two methods, *linear surface stress extrapolation* and *quadratic stress extrapolation* have been used to evaluate the SHSS. Through the linear surface stress extrapolation, the hot-spot stress is calculated by taking the stresses at two reference points and extrapolating a value for the weld toe (Al-Emrani & Aygül, 2014). However, using linear surface stress extrapolation might sometimes be conservative, and the technique of quadratic stress extrapolation is more accurate, instead of taking two reference points three are used to validate the hot-spot stress. Both methods can be used for detail Type a and Type b, however, the location of the reference points varies depending on the flange thickness t and whether the finite element model has fine or coarse mesh. See Figure 2.10 and Table 2.2 for illustrations and values of the two methods. The distances shown in Table 2.2 are between the hot-spot stress at the weld toe and the extrapolation points. Lastly, it should be mentioned that there are plenty of other methods that can be used to derive the SHSS, these can be read about in Al-Emrani and Aygül (2014) report.

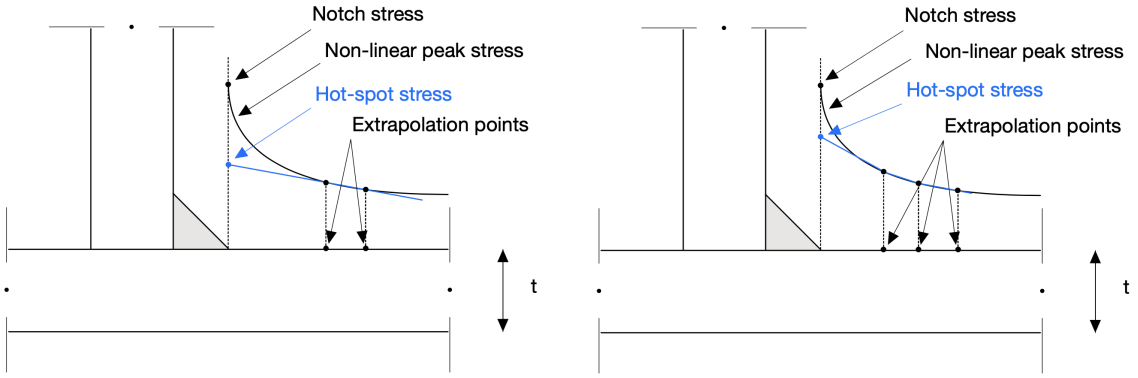

(a) *Sketch of Linear extrapolation.* **(b)** *Sketch of Quadratic extrapolation.*

Figure 2.10: *Linear- and quadratic extrapolation of structural hot-spot stress.*

Table 2.2: *Distance from the hot-spot point to the reference points using Linear- and quadratic extrapolation.*

	Linear extrapolation				**Quadratic extrapolation**					
	Fine mesh		*Coarse mesh*		*Fine mesh*			*Coarse mesh*		
	1st point	2nd point	1st point	2nd point	1st point	2nd point	3rd point	1st point	2nd point	3rd point
Type a	0.4t	1.0t	0.5t	1.5t	0.4t	0.9t	1.4t	0.5t	1.5t	2.5t
Type b	-	-	5 mm	15 mm	4 mm	8 mm	12 mm	-	-	-

The equations used for calculating the structural hot-spot stress for a detail of Type a, can be seen below. Both equations are for a FE-model having fine mesh, Equation (2.6) is used for linear extrapolation and Equation (2.7) is used for quadratic extrapolation (Al-Emrani & Aygül, 2014).

$$\sigma_{SHSS} = 1.67 \cdot \sigma_{0.4t} - 0.67 \cdot \sigma_{1.0t} \tag{2.6}$$

$$\sigma_{SHSS} = 2.52 \cdot \sigma_{0.4t} - 2.24 \cdot \sigma_{0.9t} + 0.72 \cdot \sigma_{1.4t} \tag{2.7}$$

Lindqvist and Nilsson (2016) mention that SHSS can be estimated analytically, numerically and experimentally. However, the numerical solution is mostly used because of the accuracy of the Finite Element method (FEM).

The International Institute of Welding (IIW) has derived hot-spot stress recommendations when a plate is exposed to bi-axial stress in the fatigue critical region (A. F. Hobbacher, 2016). The maximum principal stress (σ_{11}) is the stress component to analyse whether the crack is located within $\pm 60°$ of the nominal stress, see Figure 2.11a. If not fulfilled, the stress perpendicular to the weld stress component should be considered ($\sigma_{\perp}$), see Figure 2.11b.

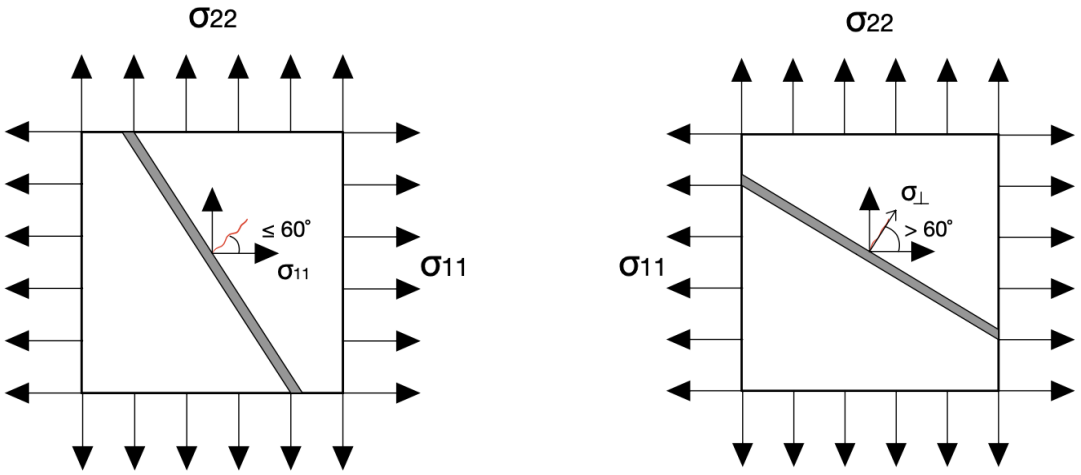

(a) $\sigma_{SHSS} = \sigma_{11}$, *for* $\theta \leq 60°$. **(b)** $\sigma_{SHSS} = \sigma_{\perp}$, *for* $\theta \geq 60°$.

Figure 2.11: *Hot-spot stress at weld toe for bi-axial stress state.*

The benefits that come with using SHSS are that the amount of S-N curves is reduced since the geometry effect is included in the stress analysis, see Figure 2.12. However, the stresses coming from the weld geometry and local defects are not included. Consequently, this makes the result of SHSS slightly different from reality (Lindqvist & Nilsson, 2016). Further, SHSS is very good at investigating toe cracking but bad when other cracking modes occur (Al-Emrani & Aygül, 2014).

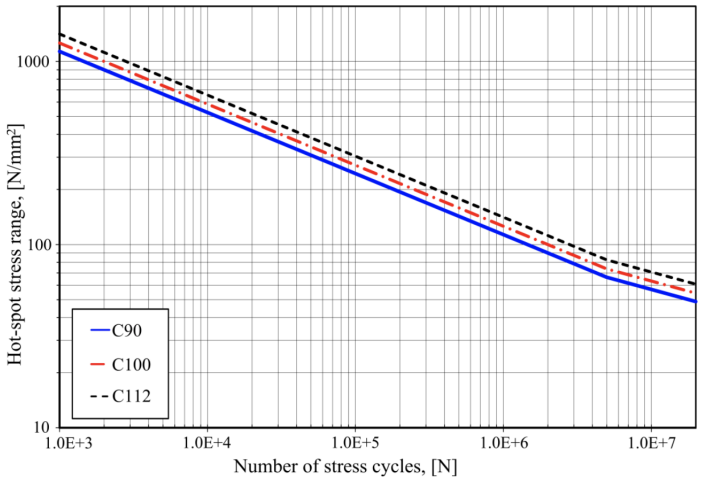

Figure 2.12: *S-N curves for the structural hot-spot stress method, (Al-Emrani & Aygül, 2014).*

2.3.3 Effective notch stress method

Local stress raisers occur due to geometrical discontinuities such as sharp changes in geometry, notches, holes and other geometrical alterations, which have a considerable effect on the fatigue life (Al-Emrani & Aygül, 2014). The so-called notch stress is the stress emerging from the local stress raisers. Therefore, the notch stress consists of the total stress originating from both the geometry of the detail and the local stress raiser itself. The magnitude of the notch stress at the welded joint is dependent on the notch radius which is essentially the sharpness of the notch.

The effective notch stress is defined as the averaged stress over a distance or a volume (Al-Emrani & Aygül, 2014). This definition is based on the fact that notch radius close to zero results in an infinite stress which cannot be used. Assuming a reference notch radius results in one single S-N curve which can be used to determine the fatigue strength of the welded detail. A reference radius of 1 mm has shown consistent results (A. Hobbacher, 2008). The actual weld contour is replaced by this effective notch root radius to consider the variation of weld shape as well as the material behaviour of the notch root, see Figure 2.13. This method is valid for plate thickness greater than 5 mm. For plates with a thickness less than 5 mm, an effective notch radius of 0.05 mm is recommended (Karakas et al., 2020).

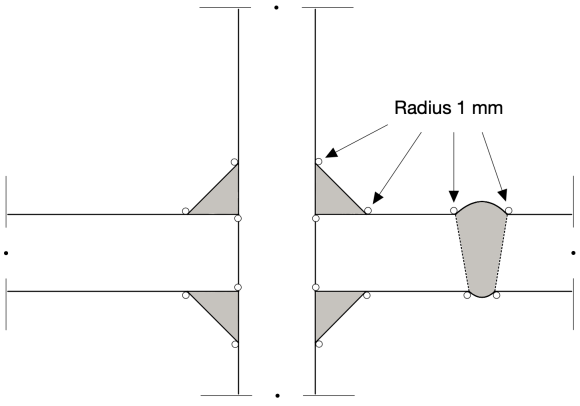

Figure 2.13: *The effective notch root radius.*

This method covers the effects of the global stress concentration and the effect from local geometry which allows for one single S-N curve for any welded detail (Al-Emrani & Aygül, 2014). According to the International Institute of Welding (IIW) recommendations, two different S-N curves, one for principle stresses and one for von Mises stresses, should be used to determine fatigue strength with effective notch stress method, see Figure 2.14. In Table 2.3 the proposed detail category for the different effective notch radiuses is presented.

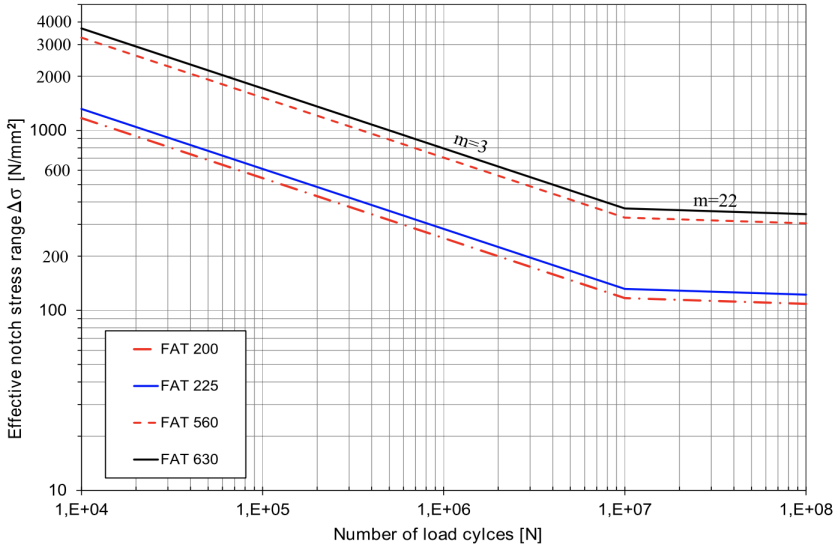

Figure 2.14: *S-N curves for the effective notch stress method, (Al-Emrani & Aygül, 2014).*

Table 2.3: *IIW recommendations for the S-N curves for the effective notch stress method (Al-Emrani & Aygül, 2014).*

Effective notch radius	**Principal stress**	**von Mises stress**
$r = 1.00mm$	FAT225	FAT200
$r = 0.05mm$	FAT630	FAT560

The ENS can be performed both analytically and numerically, however, the latter is more common (Al-Emrani & Aygül, 2014). Also, the ENS can be used to determine both toe and root cracking for fillet welds due to the effective notch root radius. Finite Element analysis (FEA) is the most common numerical analysis to determine the effective notch stress at weld toes and roots. Although the effective notch method is an accurate method to evaluate the fatigue strength of welds, it is not suitable if there is a remarkable stress raiser parallel to the weld. In such cases, the nominal stress method is preferred when performing the fatigue evaluation on corrugated web girders.

3 Previous research on fatigue of corrugated web girders

Understanding the fatigue behaviour of steel beams is essential in order to limit the risk of failure. Therefore, previous laboratory fatigue experiments on corrugated web girders have been done to analyse their behaviour depending on different geometry and loading conditions. Fatigue experiments are expensive and requires a lot of time (Save & Åkermo, 2020).

In addition to the laboratory experiments, numerical simulations have been done in the FEM software Abaqus to analyse specific parameters that affect the fatigue life. After validating that the experimental and numerical result comply, the model has further been used to check how the different parameters affect the fatigue life. This has been done through the method of one-factor-at-a-time analysis (OFAT). This means that one parameter has been analysed and the other factors have been kept the same (Xu et al., 2019).

3.1 Experimental studies

This section contains a summary of previous fatigue experiments that have been performed on trapezoidal corrugated web girders. The geometry, loading condition, and welding procedure are different in different investigations. Therefore, the in-data for each experiment varies, which needs to be kept in mind for the comparison of results. A brief conclusion of all the experiments is presented and the data is summarized in Table 3.1.

The loading procedures are similar for all the test girders. Firstly, the beams have been loaded statically and later with cyclic loading in order to simulate the reality. The cycling loading will continue until either failure appears or the test "runs out", in other terms, end without fatigue cracking (Rodriguez, 2000).

Sherif A. Ibrahim (2001)
Six identical trapezoidal corrugated web girders welded with semi-automatic welding were tested for fatigue. The girder was simply supported and subjected to four-point loading each with different stress ranges (Ibrahim, 2001). See Figure 3.1 and 3.2 for visualization of the geometry of the girder.

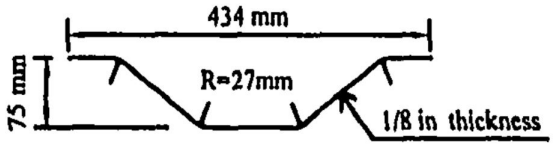

Figure 3.1: *Geometry of the corrugation profile, (Ibrahim, 2001).*

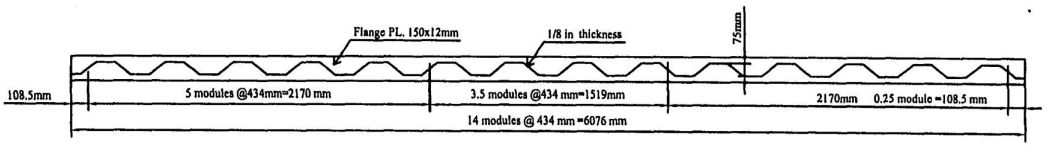

Figure 3.2: *Geometry of the girder under four-point loading, (Ibrahim, 2001).*

The outcome of the six experiments was that all the girders cracked in the constant moment zone due to fatigue. Five of the girders cracked at the S-point as expected while one cracked in the middle of the inclined fold due to a start-stop weld defect. The nominal stresses varied between $60.73 - 161.84MPa$ and the fatigue lives turned out between $1.23 - 17.6$ millions of cycles.

Sause et al. (2003)
Sause et al. (2003) performed fatigue strength tests on eight girders with trapezoidal corrugated webs, see Figure 3.3. Six of these specimens were welded using semiautomatic Gas Metal Arc Welding (GMAW), and two specimens were re-fabricated from the first and fourth girder and re-welded using robotic GMAW. The web-to-flange weld size was specified to $8mm$ and had a yield strength of $345MPa$. Welding stop-start points were avoided within the web bend region due to the risk of local weld defects, and most of the welding stop-starts were done at the horizontal fold and occasionally on the inclined fold.

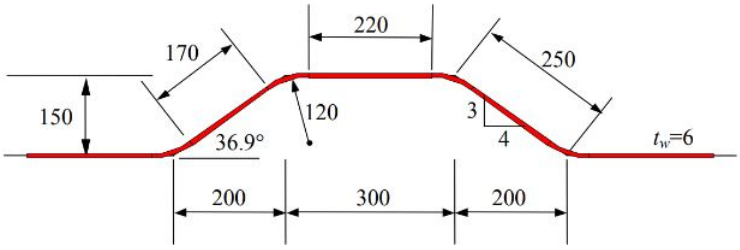

Figure 3.3: *Geometry of the corrugation profile, (Sause et al., 2003).*

The fatigue strength tests consisted of four-point bending under a dynamic load, see Figure 3.4. The main variables in the test was the stress range and welding procedure (Sause et al., 2003). The purpose was to determine the welding process effect on fatigue strength. The intention of the experimental tests of identical girders with the same stress range was to confirm the results. The nominal stress variations ranged between $103 - 138MPa$. Based on the results from the fatigue strength test, it was noted that the fatigue crack initiation was mostly associated with the weld toe geometry from the semiautomatic GMAW. The summary from these tests was that the robotic GMAW resulted in an increase of 42 % in fatigue life. This result depends on the uniformity in the weld toe geometry from the robotic welding.

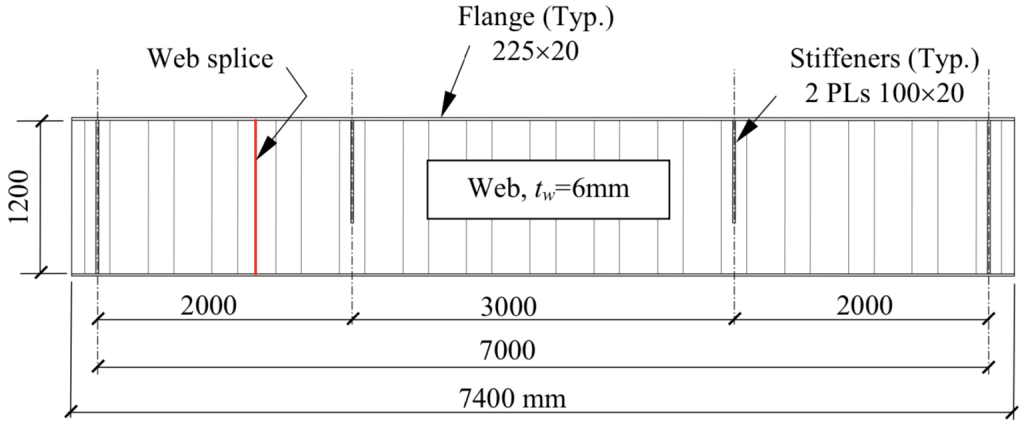

Figure 3.4: *Geometry of the girder under four-point loading, (Sause et al., 2003).*

Kotaki et al. (2003)
The experimental study by Kotaki et al. (2003) was done on two different corrugated web specimens and two of each specimen was produced. The first specimen was composed of both flanges in steel quality SM490YB and the web of steel quality SM400 (Kotaki et al., 2003). The second specimen had the same steel quality in the top flange and the web as the first specimen, however, the bottom flange was constituted of steel quality SM570. The girders were separately analysed and exposed to four-point bending. The bottom flange in the girders reached the same nominal stress being $150MPa$. The final failure appeared in the constant moment zone with the fatigue life of 1.38 and 1.60 millions of cycles. In Figure 3.5 the corrugation geometry of the specimens are presented.

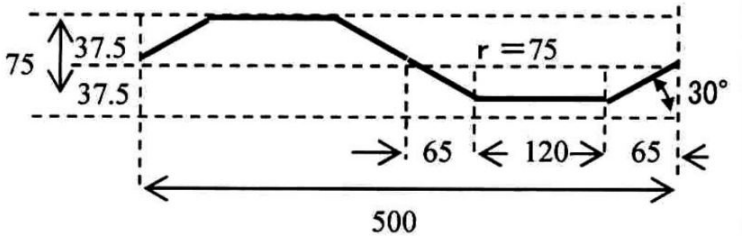

Figure 3.5: *Geometry of the corrugation profile, (Kotaki et al., 2003).*

Wang et al. (2013)
Two girder specimens have been tested to analyse what effect the corrugation angle has on fatigue strength (Wang et al., 2013a). The two girders were made of Q345 steel and were geometrically identical apart from having a corrugation angle of either 30.6° or 45°. The fillet welds were semiautomatic Gas Metal Arc Welded (GMAW) to avoid failure in start-stop locations. The two girders were exposed to three-point bending, see Figure 3.6. The measured nominal stresses in the girders received were 144.54 MPa for 30.6° and 117.49 MPa for 45° angle of corrugation. Based on this, the fatigue life was calculated to be 1.05 and 3.2 million number of cycles in the first and second girders, respectively. The test result showed that the girder with 30.6° corrugation angle failed in a crack that started in a notch in the flange. However, in the girder having 45° corrugation angle a fatigue crack appeared where the inclined fold meet the longitudinal weld as expected (Wang et al., 2013a).

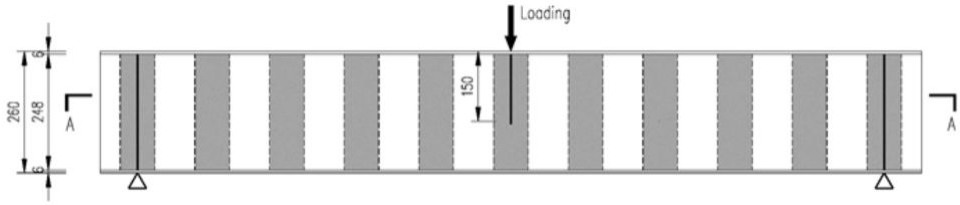

Figure 3.6: *Geometry of the girder under three-point loading, (Wang et al., 2013a).*

Apart from the two girders, Wang et al. (2013a) also tested 28 smaller specimens having the length of a half corrugation containing the inclined fold as the location of failure, see Figure 3.7. The corrugated-web T-section members (CWT), and they were subjected to tension.

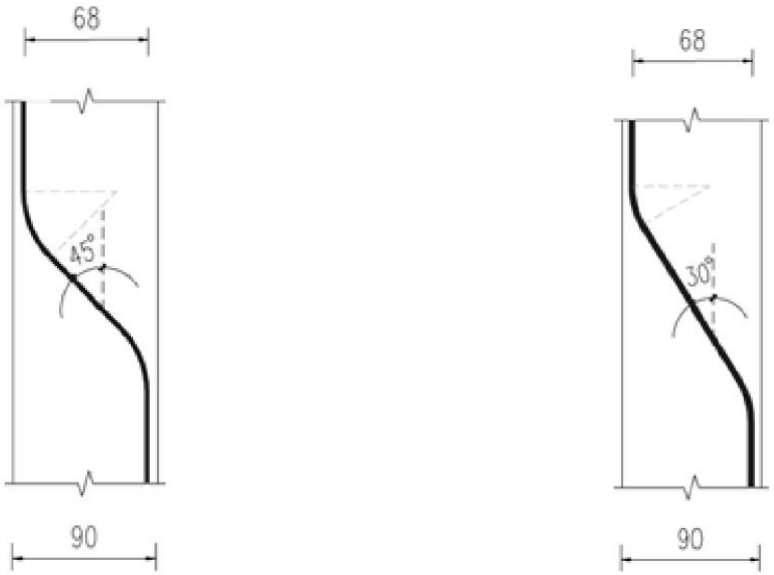

(a) *Geometry of the CWT, R=45.* **(b)** *Geometry of the CWT, R=30.*

Figure 3.7: *Geometry of the corrugation profile, (Wang et al., 2013a).*

14 of the specimen were tested having a corrugation angle of 30° and 14 had a corrugation angle of 45°. The conclusion received was that all the specimens having the corrugation angle of 45° failed in the expected S-point. Further, one of the specimens having 30° angle of corrugation failed in a notch in the flange, and the rest failed in the S-point. The conclusion when analysing the crack pattern was that the S-point moves from the end of the inclined fold when having a larger corrugation angle.

Lastly, the nominal stresses varied between $138.36 - 199.53 MPa$ for the specimen having 30° corrugation angle and having a fatigue life between 0.726 and 2.529 million number of cycles. Further, the nominal stresses for 45° corrugation angle varied between $124.17 - 198.61 MPa$ having a fatigue life between 0.570 and 1.919 million number of cycles (Wang et al., 2013a).

B. Kövesdi & L. Dunai (2014)
Six test specimens having steel class 355 were investigated under static and repeated load with the aim of testing their fatigue behaviour (Kövesdi & Dunai, 2014). The experiment consisted of identical corrugated web girders having varied stress, loading condition and weld size. Two of the girders were tested under four-point bending while the rest were tested for three-point bending. Four of the specimens were constructed with a weld size of $6mm$ while the other two had a weld size of $3mm$. All the test girders were simply supported at both ends. More detail of the in-data can be found in the following Figures 3.8, 3.9 and 3.10.

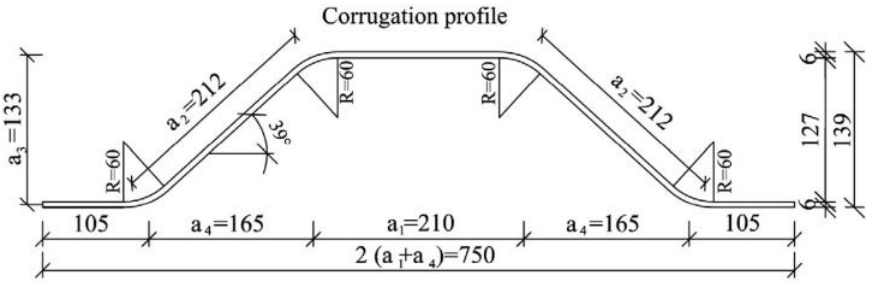

Figure 3.8: *Geometry of the corrugation profile, (Kövesdi & Dunai, 2014).*

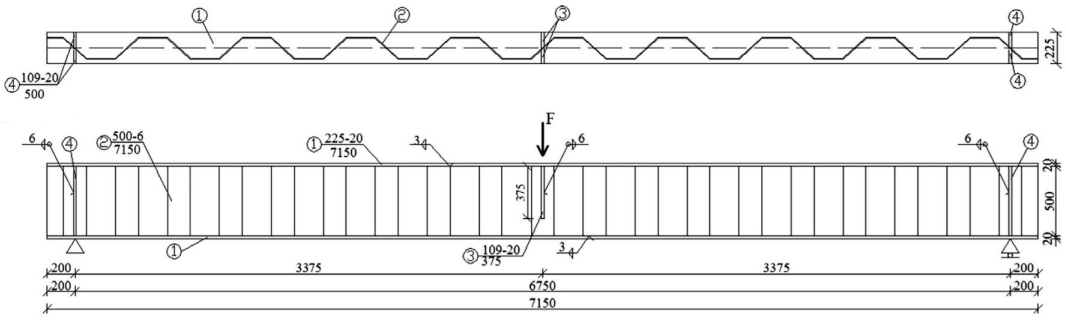

Figure 3.9: *Geometry of the girder under three-point loading, (Kövesdi & Dunai, 2014).*

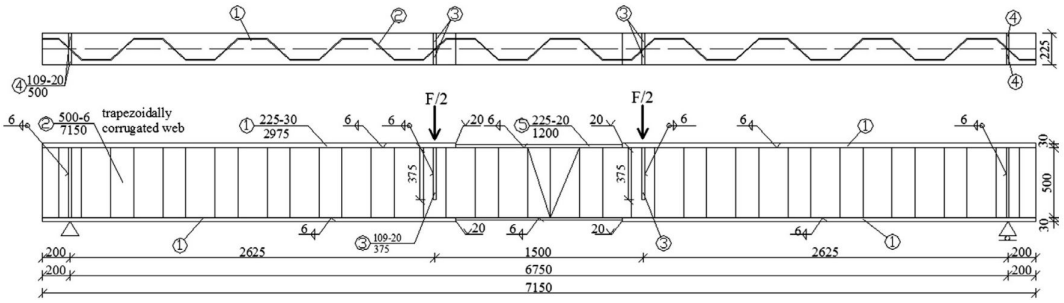

Figure 3.10: *Geometry of the girder under four-point loading, (Kövesdi & Dunai, 2014).*

The outcome from the laboratory experiments showed that the two beams subjected to four-point bending and one subjected to three-point bending had no risk of fatigue failure occurring since they reached 4 million cycles. Kövesdi & Dunai (2014) mentioned that the rest of the girders reached fatigue failure where the crack initiated in the S-point in the tension flange. Further, the authors saw that by having a smaller weld size, the fatigue life became longer. The nominal stress range in the girders varied between $100.6 - 148.81 MPa$ and the number of cycles between $1.31 \cdot 10^6 - 3.27 \cdot 10^6$.

J. Xu et al. (2019)
Xu et al. (2019) tested one prefabricated specimen having oblique flanges with an angle of 19.3°, see Figures 3.11a and 3.11b. The oblique flanges made it possible to investigate the fatigue performance of corrugated webs in box girders. The girder had a steel class of 355. Further, the girder was simply supported and tested for four-point bending, see Figure 3.12. The nominal stress became $66MPa$ and the fatigue life 5.74 millions of cycles. Lastly, the result from the experiment showed that the girder failed outside the constant moment zone and of all the cracks that appeared in the girder most of them were initiated in the S-point (Xu et al., 2019).

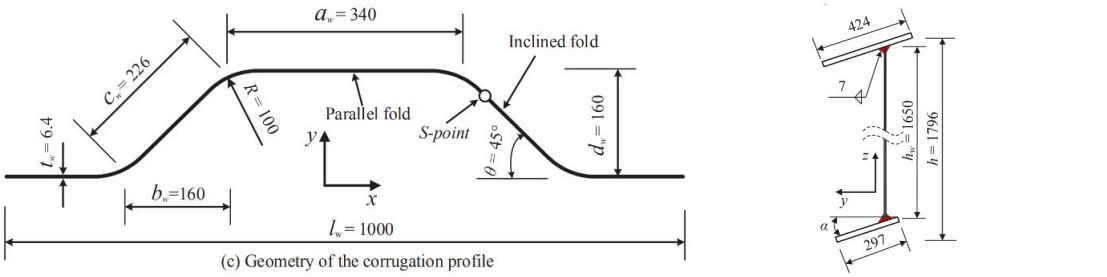

(a) *Geometry of the corrugation profile.* **(b)** *Section showing the oblique flanges.*

Figure 3.11: *Geometry of the girder, (Xu et al., 2019).*

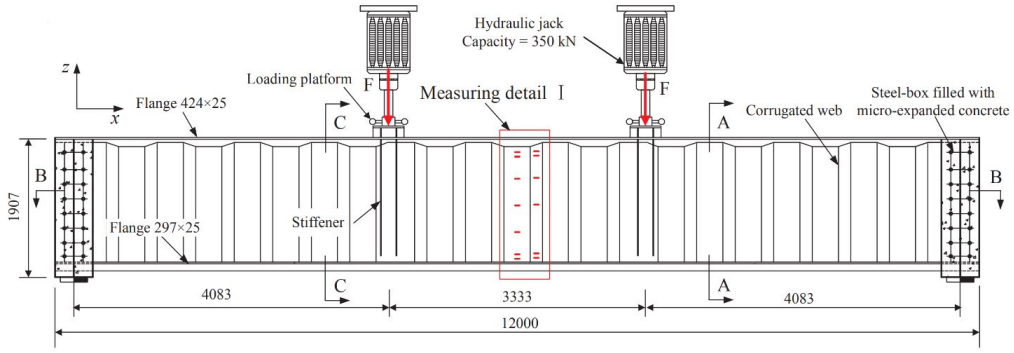

Figure 3.12: *Geometry of the girder under four-point loading, (Xu et al., 2019).*

Tong et al. (2024)
In order to improve the efficiency of analysing the fatigue behaviour of corrugated web girders, Tong et al. (2024) realized that a corrugated web girder (CWG) behaves the same as simplified corrugated-web T-section members (CWT). Tong et al. conducted one experiment on a CWG specimen subjected to four-point bending (Fig 3.13) and 20 experiments on CWT specimen (Fig 3.14). The flanges of the CWT specimen were subjected to alternating axial loading. Otherwise, the girders had the same structural details meaning steel quality, corrugation of the web and welding procedure, see Figure 3.15.

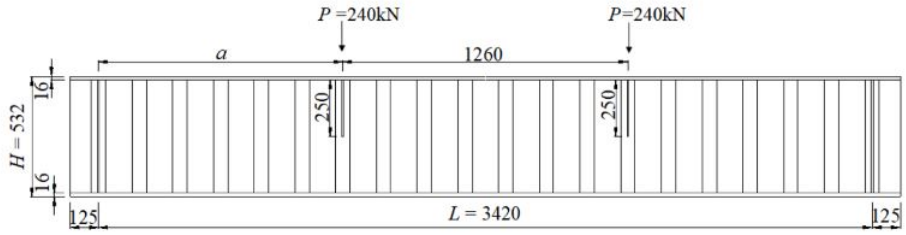

Figure 3.13: *Geometry of the CWG under four-point loading, (Tong et al., 2024).*

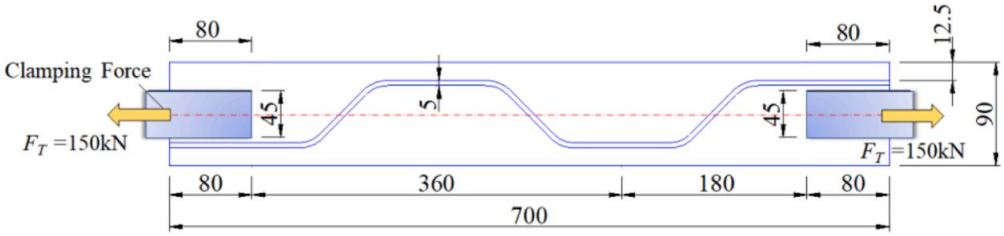

Figure 3.14: *Geometry of the CWT loaded with tension, (Tong et al., 2024).*

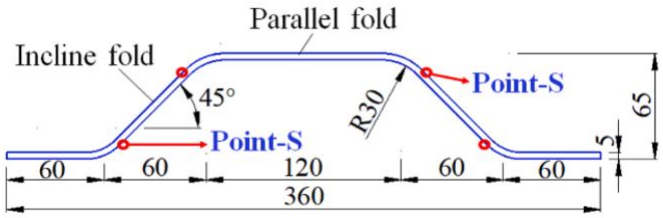

Figure 3.15: *Geometry of the corrugation profile, R30, (Tong et al., 2024).*

The final nominal stress of the CWG was $116MPa$ having the fatigue life of 1.8 millions of cycles. Out of the 20 CWT speecimens that were tested, 10 had a radius of $30mm$ and the rest had a radius of $60mm$. Lastly, the nominal stress of the CWT specimens varied between $140 - 200MPa$ having the number of failure varying between $0.32 - 2.28$ million of cycles. The majority of the final fatigue failure appeared in the S-point. For two of the specimens, the experiment reached "run-out" after 3 million of cycles and no cracks were initiated.

The conclusion that Tong et al. (2024) obtained was that the results from CWG and CWT complied, meaning that the S-N curves from CWT can be used to validate the fatigue life of a CWG as well.

Table 3.1: Geometrical and testing parameters on previous experiments.

Reference	Type of specimen	Specimen	Loading type	L [mm]	L0 [mm]	bf [mm]	tf [mm]	hw [mm]	tw [mm]	a3 [mm]	a2 [mm]	a1 [mm]	θ [°]	R [mm]	wave length [mm]	aw [mm]	Δσnom [MPa]	Nf
Ibrahim (2001)	CWG	CWG2-1	4-point	6076	5859	150	12.7	500	3	75	125	117	36.87	27	434	5	97.16	2160000
	CWG	CWG2-2	4-point	6076	5859	150	12.7	500	3	75	125	117	36.87	27	434	5	60.73	17613800
	CWG	CWG2-3	4-point	6076	5859	150	12.7	500	3	75	125	117	36.87	27	434	5	142.41	1595000
	CWG	CWG2-4	4-point	6076	5859	150	12.7	500	3	75	125	117	36.87	27	434	5	137.24	1806100
	CWG	CWG2-5	4-point	6076	5859	150	12.7	500	3	75	125	117	36.87	27	434	5	161.84	1235100
	CWG	CWG2-6	4-point	6076	5859	150	12.7	500	3	75	125	117	36.87	27	434	5	97.16	9339000
Sause et al. (2003)	CWG	G2A	4-point	7400	7000	227	20	1200	6	150	250	300	36.9	120	1000	8	138	1418000
	CWG	G1A	4-point	7400	7000	227	20	1200	6	150	250	300	36.9	120	1000	8	138	1448000
	CWG	G4A	4-point	7400	7000	227	20	1200	6	150	250	300	36.9	120	1000	8	138	1304000
	CWG	G6A	4-point	7400	7000	227	20	1200	6	150	250	300	36.9	120	1000	8	103	2563000
	CWG	G4B	4-point	7400	7000	227	20	1200	6	150	250	300	36.9	120	1000	8	138	1980000
	CWG	G1B	4-point	7400	7000	227	20	1200	6	150	250	300	36.9	120	1000	8	110	3500000
	CWG	G5A	4-point	7400	7000	227	20	1200	6	150	250	300	36.9	120	1000	8	103	7317000
	CWG	G3A	4-point	7400	7000	227	20	1200	6	150	250	300	36.9	120	1000	8	103	7645000
Kotaki (2003)	CWG	1	4-point	6500	6000	300	19/12	600	4.5	75	130	120	30	75	500	-	150	1380000
	CWG	2	4-point	6500	6000	300	19/12	600	4.5	75	130	120	30	75	500	-	150	1650000
Wang et al. (2013)	CWG	B1-030-n	3-point	1760	1600	88	6	248	4	64	82	82	30.6	-	320	3	144.54	1050000
	CWG	B4-045-n	3-point	1760	1600	88	6	248	4	64	82	82	45	-	320	3	117.49	3200000
Wang (2013)	CWT	030-1	Uniaxial	160	-	90	6	12	4	64	82	82	30	60	160	3	138.36	2529298
	CWT	030-2	Uniaxial	160	-	90	6	12	4	64	82	82	30	60	160	3	139.32	2269865
	CWT	030-3	Uniaxial	160	-	90	6	12	4	64	82	82	30	60	160	3	158.12	1659587
	CWT	030-4	Uniaxial	160	-	90	6	12	4	64	82	82	30	60	160	3	158.12	1524053
	CWT	030-5	Uniaxial	160	-	90	6	12	4	64	82	82	30	60	160	3	163.31	1309182
	CWT	030-6	Uniaxial	160	-	90	6	12	4	64	82	82	30	60	160	3	162.93	1233105
	CWT	030-7	Uniaxial	160	-	90	6	12	4	64	82	82	30	60	160	3	169.04	1071519
	CWT	030-8	Uniaxial	160	-	90	6	12	4	64	82	82	30	60	160	3	167.88	997700
	CWT	030-9	Uniaxial	160	-	90	6	12	4	64	82	82	30	60	160	3	178.24	801678
	CWT	030-10	Uniaxial	160	-	90	6	12	4	64	82	82	30	60	160	3	189.23	928966
	CWT	030-11	Uniaxial	160	-	90	6	12	4	64	82	82	30	60	160	3	188.36	812831
	CWT	030-12	Uniaxial	160	-	90	6	12	4	64	82	82	30	60	160	3	198.15	866962
	CWT	030-13	Uniaxial	160	-	90	6	12	4	64	82	82	30	60	160	3	198.15	772681
	CWT	030-14	Uniaxial	160	-	90	6	12	4	64	82	82	30	60	160	3	199.53	726106

Wang et al. (2013)	CWT	θ45-1	Uniaxial	160	-	90	6	12	4	64	82	82	45	60	160	3	124.17	19188669
	CWT	θ45-2	Uniaxial	160	-	90	6	12	4	64	82	82	45	60	160	3	124.17	16749143
	CWT	θ45-3	Uniaxial	160	-	90	6	12	4	64	82	82	45	60	160	3	125.03	13152225
	CWT	θ45-4	Uniaxial	160	-	90	6	12	4	64	82	82	45	60	160	3	138.36	12105598
	CWT	θ45-5	Uniaxial	160	-	90	6	12	4	64	82	82	45	60	160	3	139.00	10399920
	CWT	θ45-6	Uniaxial	160	-	90	6	12	4	64	82	82	45	60	160	3	138.36	9840111
	CWT	θ45-7	Uniaxial	160	-	90	6	12	4	64	82	82	45	60	160	3	148.25	9015711
	CWT	θ45-8	Uniaxial	160	-	90	6	12	4	64	82	82	45	60	160	3	148.25	8749841
	CWT	θ45-9	Uniaxial	160	-	90	6	12	4	64	82	82	45	60	160	3	158.12	7925011
	CWT	θ45-10	Uniaxial	160	-	90	6	12	4	64	82	82	45	60	160	3	164.06	6745281
	CWT	θ45-11	Uniaxial	160	-	90	6	12	4	64	82	82	45	60	160	3	178.24	5610481
	CWT	θ45-12	Uniaxial	160	-	90	6	12	4	64	82	82	45	60	160	3	178.24	4920401
	CWT	θ45-13	Uniaxial	160	-	90	6	12	4	64	82	82	45	60	160	3	198.61	4178301
	CWT	θ45-14	Uniaxial	160	-	90	6	12	4	64	82	82	45	60	160	3	198.61	5701641
B. Kövesdi & L.Dunai (2014)	CWG	1	4-point	7150	6750	225	20	500	6	133	212	210	39	60	750	6	100.6	44860001
	CWG	2	4-point	7150	6750	225	20	500	6	133	212	210	39	60	750	6	110.63	41620001
	CWG	3	3-point	7150	6750	225	20	500	6	133	212	210	39	60	750	6	146.7	13100001
	CWG	4	3-point	7150	6750	225	20	500	6	133	212	210	39	60	750	6	140.27	13260001
	CWG	5	3-point	7150	6750	225	20	500	6	133	212	210	39	60	750	3	148.81	13720001
	CWG	6	3-point	7150	6750	225	20	500	6	133	212	210	39	60	750	3	127.54	15000001
Xu (2019)	CWG	1	4-point	12000	11500	424/297	25	1650	6.4	160	226	340	45	100	1000	7	66	6208700
Tong et al. (2024)	CWG	CWG-R30	4-point	3670	3420	150	16	500	5	60	-	120	45	30	360	5	115.50	1386000
Tong et al. (2024)	CWT	R30-1	Uniaxial	700	540	90	8	40	5	60	-	120	45	30	360	5	200	320000
	CWT	R30-2	Uniaxial	700	540	90	8	40	5	60	-	120	45	30	360	5	190	370000
	CWT	R30-3	Uniaxial	700	540	90	8	40	5	60	-	120	45	30	360	5	180	789000
	CWT	R30-4	Uniaxial	700	540	90	8	40	5	60	-	120	45	30	360	5	170	763000
	CWT	R30-5	Uniaxial	700	540	90	8	40	5	60	-	120	45	30	360	5	160	972000
	CWT	R30-6	Uniaxial	700	540	90	8	40	5	60	-	120	45	30	360	5	155	1138000
	CWT	R30-7	Uniaxial	700	540	90	8	40	5	60	-	120	45	30	360	5	153	1140000
	CWT	R30-8	Uniaxial	700	540	90	8	40	5	60	-	120	45	30	360	5	151	3000000
	CWT	R30-9	Uniaxial	700	540	90	8	40	5	60	-	120	45	30	360	5	150	2280000
	CWT	R30-10	Uniaxial	700	540	90	8	40	5	60	-	120	45	30	360	5	140	3000000
Tong et al. (2024)	CWT	R60-1	Uniaxial	700	540	90	8	40	5	60	-	120	45	60	360	5	200	375000
	CWT	R60-2	Uniaxial	700	540	90	8	40	5	60	-	120	45	60	360	5	192	415000
	CWT	R60-3	Uniaxial	700	540	90	8	40	5	60	-	120	45	60	360	5	185	672000
	CWT	R60-4	Uniaxial	700	540	90	8	40	5	60	-	120	45	60	360	5	184	433000
	CWT	R60-5	Uniaxial	700	540	90	8	40	5	60	-	120	45	60	360	5	175	605000
	CWT	R60-6	Uniaxial	700	540	90	8	40	5	60	-	120	45	60	360	5	173	1059000
	CWT	R60-7	Uniaxial	700	540	90	8	40	5	60	-	120	45	60	360	5	165	1059000
	CWT	R60-8	Uniaxial	700	540	90	8	40	5	60	-	120	45	60	360	5	162	419000
	CWT	R60-9	Uniaxial	700	540	90	8	40	5	60	-	120	45	60	360	5	161	1028000
	CWT	R60-10	Uniaxial	700	540	90	8	40	5	60	-	120	45	60	360	5	156	1035000

3.2 Numerical studies

The following section contains a summary of numerical analyses performed on trapezoidal corrugated web girders. Further, through the method OFAT different conclusions on which corrugation parameters that are important regarding the fatigue life has been obtained.

Sause et al. (2005)
Sause et al. performed a linear elastic FEM analysis to evaluate the fatigue behaviour of a corrugated web beam previously tested under fatigue loading in 2003. The stress conditions at the weld toe along the incline fold were evaluated (Sause et al., 2005). Firstly, the FEM analysis was performed on the entire CWG specimen using 8-node solid elements. Based on the displacements from the first analysis, the boundary conditions was set on the sub-model in the second analysis. The second FEM analysis was also performed with 8-node solid elements and a toe radius of the weld was assumed to be $1mm$. The results from the FEM analysis confirmed the experimental results that the crack near the S-point developed ahead of the cracks initiating closer to the middle of the inclined fold.

Furthermore, a parametric FEM analysis was performed in order to demonstrate the influence of corrugation parameters such as the corrugation angle, the bending radius, the corrugation depth, length of the parallel fold, as well as the flange thickness and the flange width (Sause et al., 2005). The parametric study consisted of 25 different configurations of corrugation and resulted in the conclusion that the corrugation angle and bending radius had the most significant influence on stress conditions at the weld toe. The highest stress appears at the S-point and it was concluded that the corrugation angle was the dominant parameter regarding the stress concentration. By decreasing the corrugation angle the stresses at the weld toe decreased.

The hot-spot stress method was performed with linear extrapolation and the result showed that hot-spot stresses increased near the S-point (Sause et al., 2005). The result from the numerical analysis showed that the size of the hot-spot stresses was 1.23 times the nominal stresses.

Ibrahim et al. (2006)
Using FEM in Abaqus, Ibrahim et al. (2006) studied how the stress concentration at the S-point is affected by changing the bending radius. They investigated this by modelling a single corrugation containing quadrilateral and triangular elements.

As mentioned in Chapter 2.2.1, a sinusoidal corrugation contains smooth transitions of the waves which avoid the appearance of stress concentrations. Through the FEM analysis that Ibrahim et al. (2006) performed, the conclusion was that by increasing the bending radius the stress concentration factor (SCF) at the S-point will be reduced. In other words by increasing the bending radius the corrugation becomes more like a sinusoidal corrugation, the fatigue life will increase (Ibrahim et al., 2006a).

Kövesdi et al. (2012)
Kövesdi et al. developed a numerical model based on the experimental study performed at Budapest University of Technology 2008 (Kövesdi et al., 2012). The numerical analysis aimed to determine the stress distribution from different loading conditions beyond the range of previous results obtained from the experiments. The corrugated web girder was modelled using 8-node thin shell elements with an element size between 15 and $25mm$. To verify the numerical model, stresses and deflection were compared to the results of the six test. The numerical model demonstrated the same elastic structural behavior as observed in the experiments and the numerical method of study verified.

Bending from uniformly distributed load was investigated. Testing under such loading conditions was conducted in order to compare the numerical results to the proposed equations for the additional transverse bending moment of the flange. The numerical analysis was performed on various cases with

different numbers of corrugation waves between support and loading points. The results from the numerical analysis showed that the most unfavourable case is the girder with support and loading points at the middle of the inclined fold and full corrugation waves between support and loading points. In addition to the numerical results from three-point bending, an enhanced equation (Equation 2.4) was derived for the maximum transverse bending moment for the most unfavourable case. The results from the numerical analysis with uniformly distributed load conformed with the equation given by Abbas et al. (2007b), Equation 2.1.

Wang et al. (2013b)
With the same geometrical data as the girder that was tested in a previous experimental study, Wang et al. (2013b) utilized FEM to investigate the intersection of the crack using ENS. The two girders having a corrugation angle of 30° and 45° were modelled. The conclusion showed that the fatigue crack initiated at the S-point which agreed with the result of the experiment. It was also shown that the stress concentration becomes larger for a larger corrugation angle. Further, it was concluded that ENS is a good method to obtain the stresses related to a fatigue crack located at the toe or root (Wang et al., 2013b).

Wang et al. (2015)
Wang et al. (2015) conducted complementary Finite Element analysis (FEA) on the girder that were previously tested in 2013. SOLID185, elements having eight nodes with three degrees of freedom in each node was used. To obtain more accurate stress distribution, a finer mesh were picked for the areas where the stress concentration may be significantly larger. To validate the model, the strains received from the laboratory experiment was compared with the numerical model.

Based on this, the model was used to investigate the effects of corrugation angle θ, and the flange thickness t_f using the effective notch stress method. Increasing the flange thickness from $5-10mm$ for a corrugation angle of 45°, resulted in reduced stresses and the fatigue life increased by 133%. However, since increasing the flange thickness consequently increases the structural weight so instead an analysis was done on the corrugation angle. By reducing the corrugation angle, the fatigue life is increased by 34.6%. Therefore, reducing the corrugation angle was recommended by the authors (Wang et al., 2015).

Xu et al. (2019)
Xu et al. (2019) implemented a girder in FEM to continue the investigation. The parameters that were further investigated OFAT, contained the corrugation angle θ, bending radius R, weld size a_w and inclination angle between the flange and horizontal axis α (Xu et al., 2019).

The structural hot-spot stresses have been used to compare the influence of the parameters. This has been done in the S-point taking the stresses $2mm$ from the weld toe. From the global model including the entire girder, sub-models focusing on the critical area have been produced.

The parameters varied between a range of numbers which all are standard dimensions recommended to use when creating a trapezoidal corrugated web girder. The corrugation angles were modelled varying between 30° and 60°. It showed that the fatigue notch factor, the ratio between effective notch stress and nominal stress, increased from 20.6% to 29.8% for a higher corrugation angle. The author stated that picking a smaller θ should be done to elongate the fatigue life. R varied between $50-200mm$, which resulted in that the fatigue notch factor increased from 27.3% to 30.9% at the S-point. Further, the inclination angle between the flange and horizontal axis varied between $10-30°$. This gave a reduction of the fatigue notch factor by 1.7% and 1.1%. The last analysis was on the weld size, which varied between 6-10 mm which gave the fatigue notch factor varying between 3.8% and 2.1%.

The conclusion of the numerical analysis was that the corrugation angle and bending radius have the largest influence on the stress concentration at the S-point. Further, the weld size has a certain impact while the inclination angle barely has any significant influence on the stresses (Xu et al., 2019).

Save and Åkermo (2020)
Four girders having varying web height, h_w, and parallel fold length, a_1, have been analysed in FEM. Save and Åkermo (2020) wanted to analyse the S-point and the shear flow and transverse bending moment in the flange using different SHSS methods. The geometry of the analysed girders has been picked from common bridge girder dimensions (Save & Åkermo, 2020).
Two of the girders were modelled to have a web height of $1500mm$ and the other two $3000mm$. The parallel fold length for two of the girders were $200mm$ and $400mm$ for the rest. All the girders were subjected to four-point bending.

The conclusion was that in SHSS method, *1 mm stress* is preferred to use when analysing parametric studies in FEM. Further, Save and Åkermo (2020) mentioned that the calculations of SHSS should include the effects of both vertical and lateral bending moments on the flange. Lastly, during the entire numerical analyses Save and Åkermo (2020) emphasized that by creating sub-models, which are smaller parts of the entire girder, it is possible to have smaller mesh and receive more accurate result.

3.3 Summary of the literature study

The following sections contain a summary of the important information obtained during the literature study.

3.3.1 Summary of the experimental data

From the experimental data compiled in Table 3.1, a nominal stress range vs. fatigue life plot has been created, see Figure 3.16. The figure contains the results from the experiments that failed in fatigue failure. Other failure reasons are mentioned in Table 3.1 and has been excluded from the graph. Through the graph, it can be seen that all the experimental results follow the same slope, and DC100 appear to be applicable for corrugated web girders.

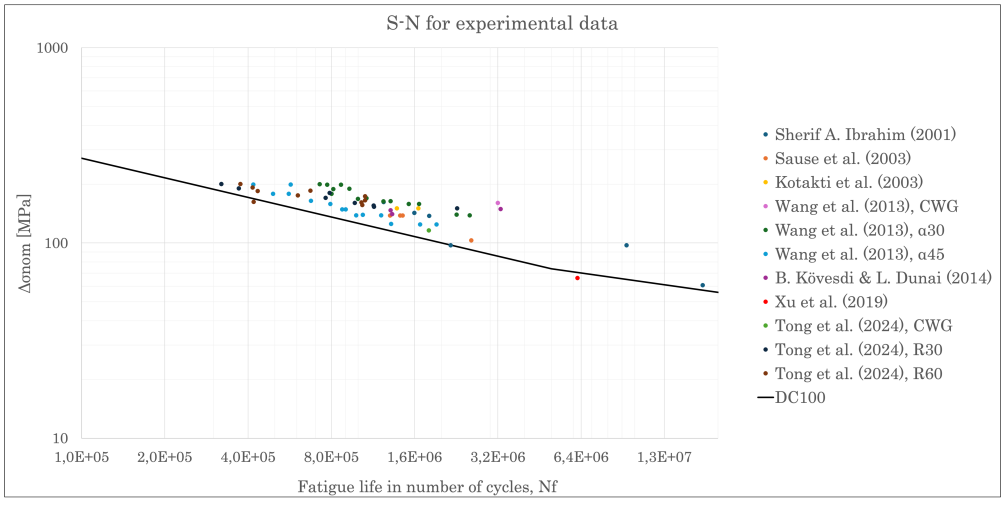

Figure 3.16: *S-N curves for the experimental data, with outliers.*

3.4 Influential parameter on fatigue behaviour of corrugated web beams

In Figure 3.16, it can be seen that three data points differ slightly from the rest by having lower stress and higher fatigue life. It includes two girders from Ibrahim (2001) and one from Xu et al. (2019). The two girders from Ibrahim (2001) exceeded the constant amplitude fatigue limit (CAFL) of 5 millions of cycles. The girder that Xu et al. (2019) analysed had a geometry that differs from the rest by having oblique flanges, therefore Xu's girder will be excluded in further investigations.

Fatigue testing is expensive and requires plenty of time to analyse. However, the problem with the tests have been that some failed due to other reasons than fatigue. The problem was that the cut-of-limit had been reached or the crack initiated in a local weld defect as start-stop locations. Save and Åkermo (2020) mentioned the importance of picking good quality of the welding to avoid the risk of local weld failure. Furthermore, Sause et al. (2003) specifically conducted an experiment analysing the welding quality where the semiautomatic weld was compared to a robotic weld. The conclusion was that the robotic welding was more uniform containing less welding ripples which increased the fatigue life.

Wang et al. (2013a) and Tong et al. (2024) concluded that it is possible to test a corrugated web T-shaped member subjected to tension. The result from their analysis showed that the CWT specimen corresponded with the result from testing an entire CWG. This further makes CWT a cheaper way of performing fatigue analysis due to the reduction of material. This can further be proven in the S-N curve (Figure 3.16) where the CWT and CWG specimens receive a fatigue result that corresponds to each other.

By compiling and comparing experimental studies, deeper knowledge has been gained about how the girders behave during a fatigue experiment. As mentioned in the literature analysis, the fatigue crack is expected to initiate in the S-point. This has been confirmed in several of the experiments; (Wang et al., 2013a) and (Ibrahim, 2001) even though the geometry of their girders differ. From the smaller CWT specimen, that Wang et al. (2013a) and Tong et al. (2024) analysed, it has been concluded that the bending radius and corrugation angle has an impact on where the S-point appears. Having a larger corrugation angle, the S-point moves from the end of the inclined fold (Wang et al., 2013a). Further, by having a smaller bending radius, the S-point will be located closer to the end of the inclined fold unlike when having a larger radius (Tong et al., 2024), see Figure 3.17a and 3.17b. Save and Åkermo (2020) mention that the corrugation parameters additionally have an impact on the stress concentration, a smaller corrugation angle and larger bending radius result in lower stress concentration.

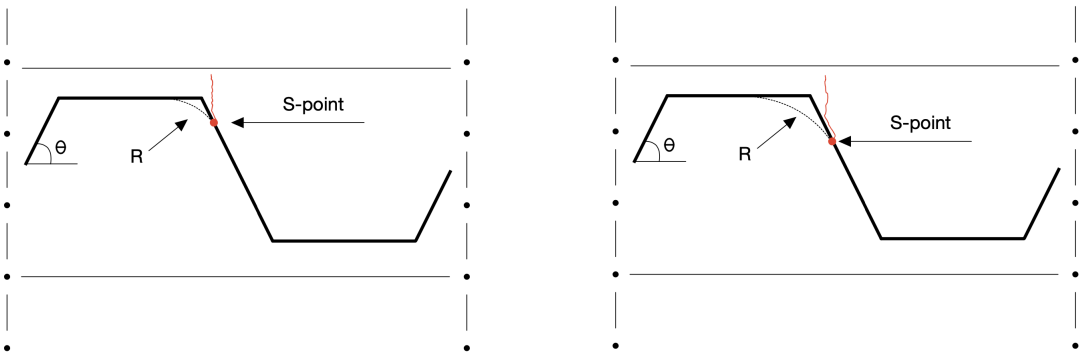

(a) *S-point for smaller bending radius.* **(b)** *S-point for larger bending radius.*

Figure 3.17: *Location of S-point for different bending radius.*

3.4.1 Summary of the numerical studies

Xu et. al (2019), Sause et al. (2005) and Wang et. al (2015) confirmed in their numerical analysis that the corrugation angle θ and the bending radius R have the largest effect on the fatigue life. Also, other parameters including weld size, a_w, inclination angle between the flange and horizontal axis, α, and flange thickness t_f, were stated to have some impact on improving the fatigue strength. However, recommendations from the authors has mentioned that in order to receive a longer fatigue life, the design parameters θ and R is preferred to be altered since they showed to have the greatest impact.

Different stress methods were selected in the previous numerical analyses. Sause et al. (2005) mentioned that using the SHSS method, larger stresses were obtained compared to the nominal stress method. This further confirmed the literature analyses saying that the SHSS apart from nominal stresses also includes the bending stresses. Save and Åkermo (2020) continued the investigation of different SHSS methods, and concluded that the method *1mm stress* is preferred to use. Wang et al. (2013) used the ENS method in their numerical investigation and concluded that it is a good method to use when analysing the fatigue crack in the root or vicinity of the toe.

Lastly, Save and Åkermo (2020) also mentioned the importance of making sub-models to facilitate the work and still have fine mesh at the investigated area.

4 FE description and validation

The following chapter contains the method of how the fatigue strength of trapezoidal corrugated girders has been investigated numerically in the current study using the nominal stress-, structural hot-spot and effective notch stress method. This has been completed through the Finite Element software Abaqus. The modelling procedure has been described and the models have been verified through a validation study and convergence study which can be seen in the following sections.

4.1 Model description

Based on the previous experiments has described in Chapter 3, all tests have been modelled in Abaqus for analyzing the fatigue life using three different methods of the nominal stress, SHSS and ENS. Specifically, the specimens that have been part of the curreent numerical analysis are selected from the experiments that Ibrahim (2001), Sause et al. (2003), Wang et al. (2013a), Kövesdi & Dunai (2014) and Tong et al. (2024) have performed. All the models have been created separately containing their individual in-data. This means that the material properties, geometry, boundary condition and type of loading differ for different models based on the experimental tests.

A global model of the entire specimen has been created in Abaqus to verify the structural behaviour of the specimen in the FEA (Finite Element analysis). In order to receive more accurate stresses at the investigated area, the specimen has been subdivided into two smaller sub-models. Al-Emrani and Aygül (2014) mentions that using sub-models is a good solution to analyse smaller part of a structure since large FE models with solid elements can require large computational time and heavy data to handle. The first sub-model has been used for the SHSS method and the second sub-model has been used for the ENS method. More information on how to create the specific models can be seen in the following section, further, the entire approach can be seen in the flow-chart presented in Figure 4.1.

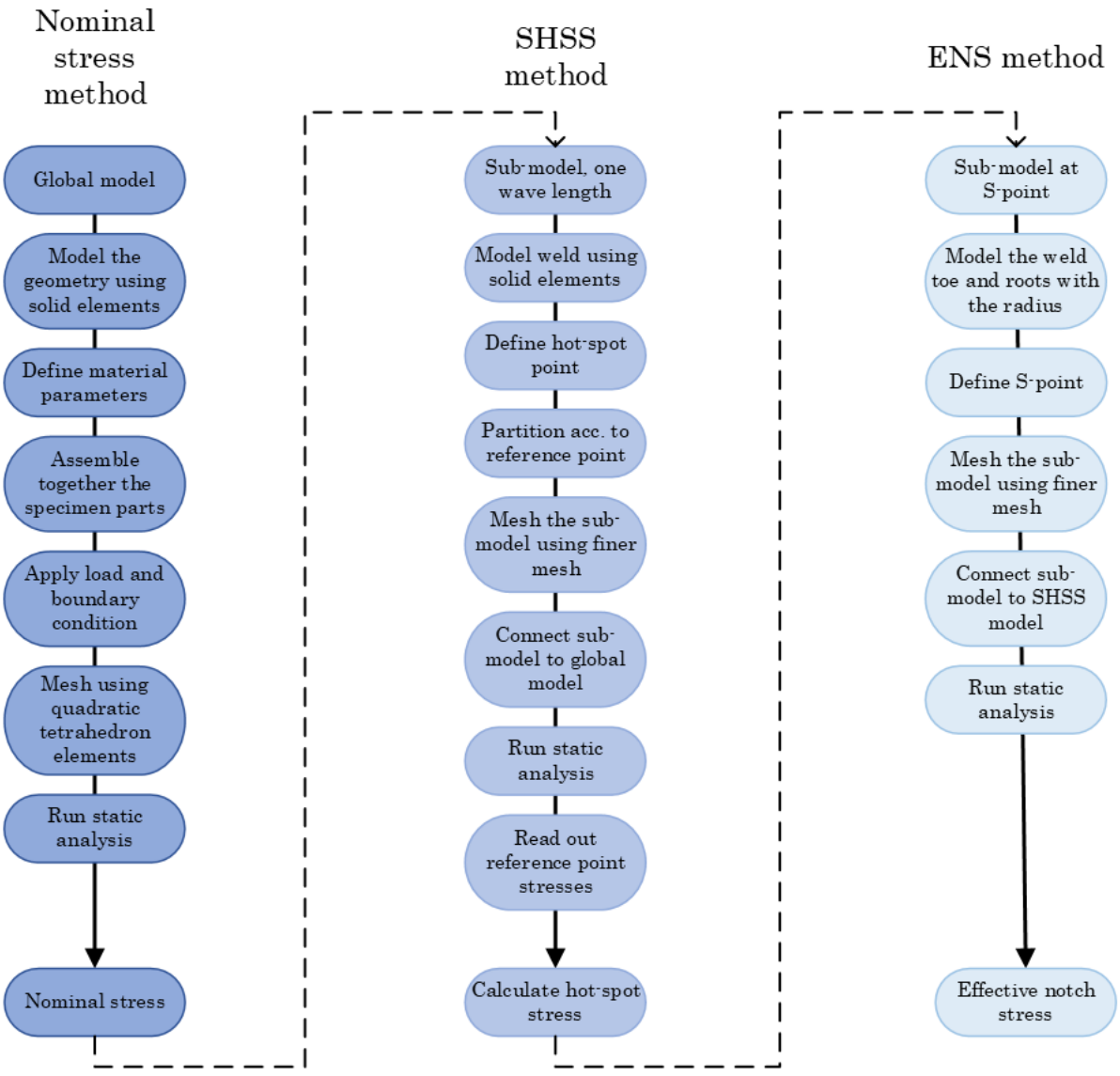

Figure 4.1: *Flow chart of creating the nominal-, SHSS- and ENS model in Abaqus.*

As mentioned in the state-of-the-art, Chapter 2.2.3, many experimental results show that the fatigue failure mainly occurs in the S-point for corrugated webs. With this knowledge, the following chapter has been written as the fatigue failure occurs in the S-point. The exact crack location in all the FE-models can be found in Appendix B.

The following FEM input data are selected in the current thesis study. More general information on how to create the model in FEM regarding local approaches can be found in Al-Emrani and Aygül's report (Al-Emrani & Aygül, 2014).

4.1.1 Global model

Three different specimens including, CWT specimens exposed to tension, CWG subjected to three-point bending and CWG subjected to four-point bending, have been selected in this current study, see Table 4.1. For this reason, the global modelling of each type has been explained separately in the following sections.

More detailed information regarding the geometry of each specimen can be found in the figures in Chapter 3.1.

Table 4.1: *Test specimen used by the different authors.*

Global model:	Authors:		
CWG, three-point bending	Kövesdi & Dunai (2014)		
CWG, four-point bending	Sherif A.Ibrahim (2001)	Sause et al. (2003)	Tong et al. (2024)
CWT	Wang et al. (2013a)	Tong et al. (2024)	

CWG with three-point bending
The fatigue experiment that Kövesdi & Dunai performed in 2014 was exposed to three-point bending. Similarly, the numerical model in Abaqus has been simulated under similar loading condition.

The CWG have been modelled using solid elements having the same geometry and loading condition as the experimental girder. The load has been applied on the flange in the middle of the girder having a stiffener underneath, see Figure 4.2. The test specimen was simply supported and the boundary conditions on the edges can be seen in Table 4.2. Further stiffeners have been added at the supports.

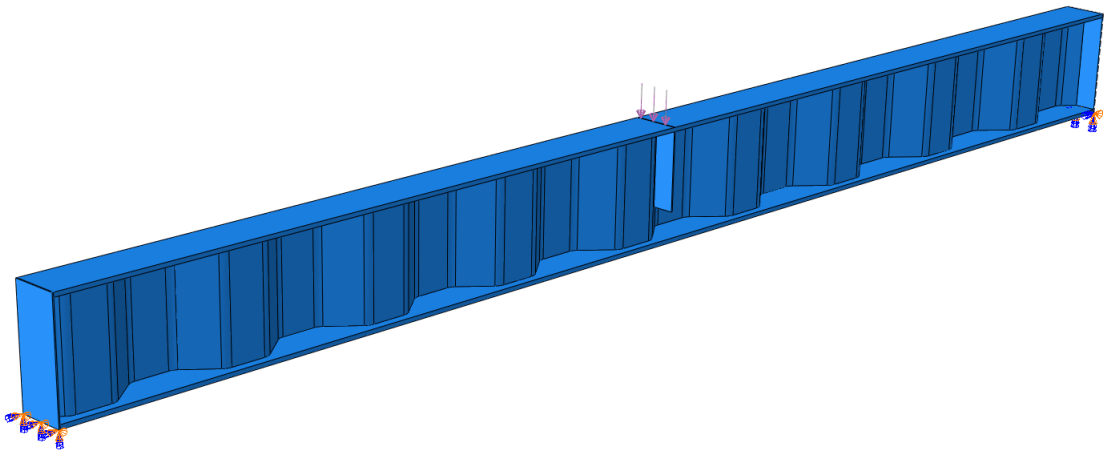

Figure 4.2: *CWG loaded with three-point bending and its boundary conditions.*

Table 4.2: *Boundary conditions for CWG, three-point bending.*

		Boundary condition					
Authors:		Ux	Uy	Uz	Rx	Ry	Rz
Kövesdi & Dunai (2014)	Left edge	0	0	0	0	1	0
	Right edge	1	0	0	0	1	0

Note: BC 1 indicates free, BC 0 indicates fixed.

A sufficient mesh has been picked to capture the realistic behaviour of the girder exposed to the load and the boundary conditions. Therefore, the flange that contains the investigated area will have a smaller mesh than the web. Further, the element type for the entire specimen has been created using solid quadratic tetrahedral elements.

Lastly, the fatigue stresses have been obtained by making a path along the width of the flange in the area of interest. Some of the specimens from the same author showed the fatigue crack in different locations of the specimen. Therefore, paths have been created for each location. All the stresses along each path have been collected and an average stress has been calculated. The stresses that have been investigated are the longitudinal stresses, S_{11}.

CWG with four-point bending

As seen in Table 4.1, some of the authors test girders were subjected to four-point bending. Apart from the material properties and geometry (see Chapter 3.1), the FE-modelling for the global model of the test specimens has been the same.

The girders have been modelled using solid elements. Further, the load has been applied on the top flange of the girder having stiffeners placed underneath the load. All the girders were tested being simply supported, see Figure 4.3. These boundary conditions have been applied in Abaqus and can be seen in Table 4.3.

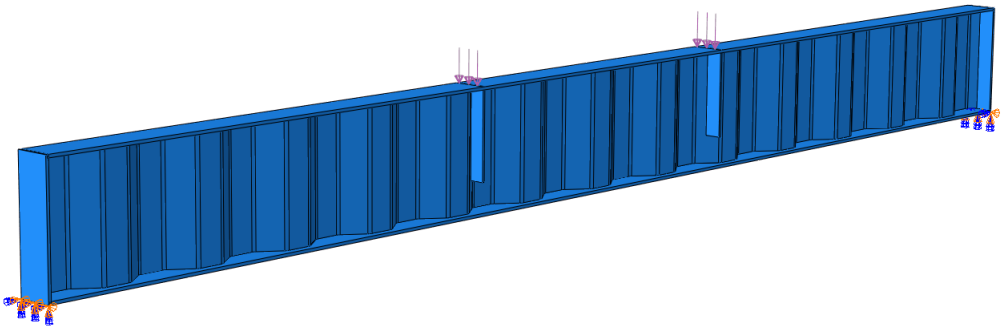

Figure 4.3: *CWG exposed to four-point bending and its boundary condition.*

Sause et al. (2003) had besides the boundary conditions as presented in Table 4.3 lateral restraints at the loading points, see Figure 4.4.

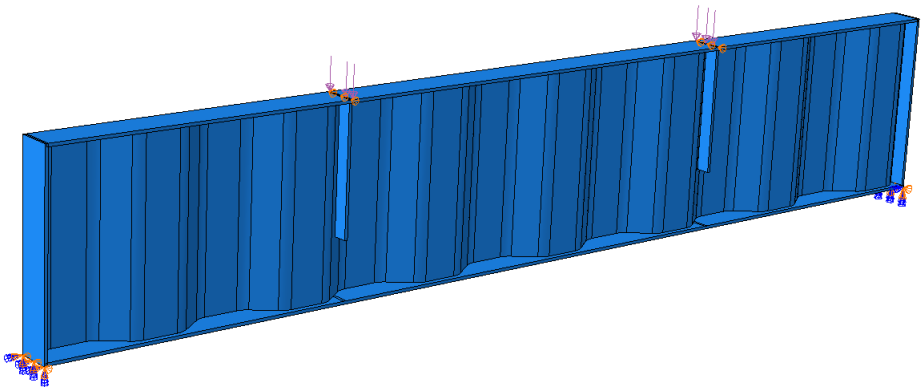

Figure 4.4: *Sause et al. (2003) specimen exposed to four-point bending and its boundary condition with lateral supports at the loading points .*

Table 4.3: *Boundary condition for CWG, four-point bending.*

		Boundary condition					
Authors:		Ux	Uy	Uz	Rx	Ry	Rz
Sherif A. Ibrahim (2001)	Right edge	1	0	0	0	1	0
	Left edge	0	0	0	0	1	0
Sause et al. (2003)	Right edge	1	0	0	0	1	0
	Left edge	0	0	0	0	1	0
Tong et al. (2024)	Right edge	1	0	0	0	1	0
	Left edge	0	0	0	0	1	0

Note: BC 1 indicates free, BC 0 indicates locked.

The mesh and stress evaluation have been performed in the same way as explained in the previous model, CWG tested in three-point bending.

CWT

The authors Wang et al. (2013a) and Tong et al. (2024) made their fatigue experiment on a smaller specimen exposed to axial loading.

The tension force has been applied to one of the flange edges, see Figure 4.5. Both the authors had their specimens clamped on one edge and allowed movement on the other edge in the x-direction. Therefore, the boundary conditions picked for the numerical analysis have been fully fixed on one edge and free to movement in the other, see Table 4.4 for clarification.

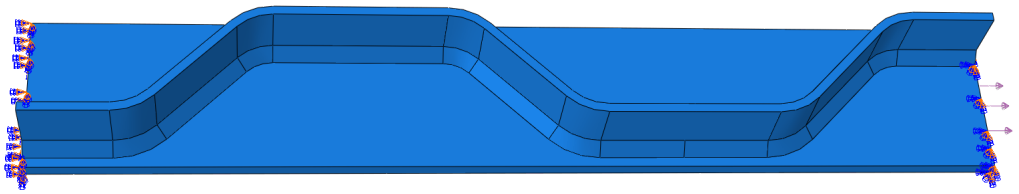

Figure 4.5: *CWT loading and boundary conditions.*

Table 4.4: *Boundary condition for CWT.*

		Boundary condition					
Authors:		Ux	Uy	Uz	Rx	Ry	Rz
Wang et al. (2013a)	Left edge	0	0	0	0	0	0
	Right edge	1	0	0	0	0	0
Tong et al. (2024)	Left edge	0	0	0	0	0	0
	Right edge	1	0	0	0	0	0

Note: BC 1 indicates free, BC 0 indicates locked.

The stress evaluation has been performed in the same way as explained in the previous models.

4.1.2 Sub-model (SHSS-model)

The following section is regarding how the sub-model has been created in Abaqus which is similar for all the global models, both CWG and CWT.

The SHSS method requires a finer mesh compared to the global model in order to receive more accurate stresses in the vicinity of the weld toe. The solution has therefore been to analyse a smaller section of the specimen using sub-modeling. The sub-model of SHSS consists of approximately one wavelength and contains more weld details compared to the global model. Lastly, the sub-model has been used to replace the global model at the specific location, see Figure 4.6.

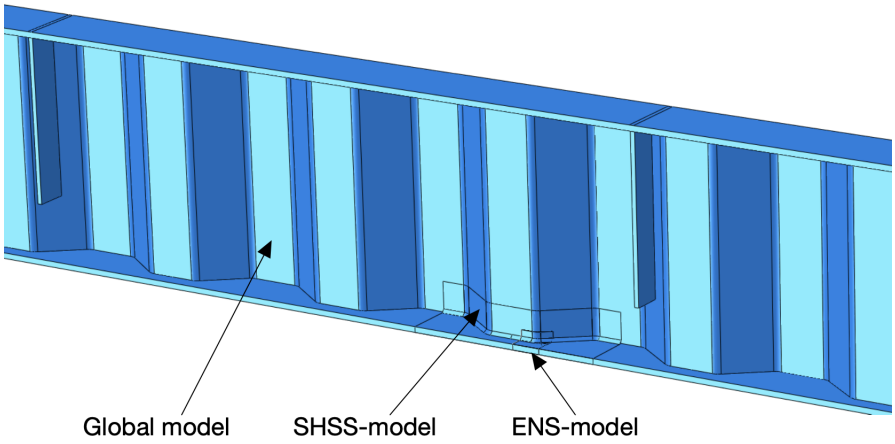

Figure 4.6: *Global model of CWG composed with the sub-models for SHSS and ENS.*

Since the boundary condition and load already has been applied to the global model these are no longer needed in the sub-model. However, new boundary conditions have to be applied on the surfaces as a reference connection to the global model. Figure 4.7 shows the hot-spot model containing all the new details and finer mesh applied to it.

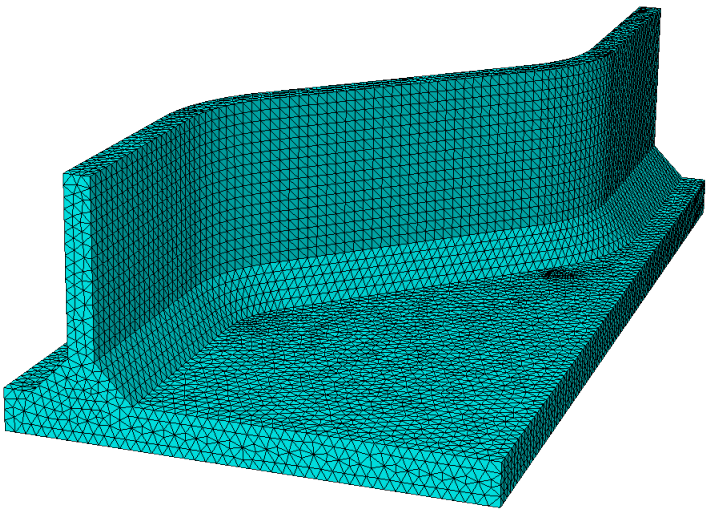

Figure 4.7: *Sub-model for SHSS analysis.*

To obtain SHSS, the weld has been modelled into the sub-model using solid elements. In order to find the hot-spot stress in the vicinity of the weld toe, the stresses from the extrapolation points have been collected by partitioning the flange for the specific distance along the weld, the distances can be found in Table 2.2. The size of the elements should be decided concerning the reference stress extrapolation points where they should align an edge node or mid-side of the element. Lastly, when the extrapolation stresses have been found, the SHSS can be calculated via analytical calculations, see Equation 2.6 and 2.7.

4.1.3 Sub-sub-model (Effective notch model)

The following section explains how the sub-sub-model has been created in Abaqus which is similar for all the models, both CWG and CWT.

As mentioned in the state-of-the-art, Section 2.3.3, the ENS method contains the most details regarding the geometrical discontinuities that exist around the welded detail. Therefore, when modelling the specimen in Abaqus for ENS, all geometrical imperfections have been modelled in order to investigate the effect from the local stress raisers. To facilitate the running time of the FEA, once again, a sub-model has been created around the S-point to find the ENS. The FE-modelling for ENS has been to use highly dense mesh in areas around the weld and coarser mesh for the rest of the specimen (Lindqvist & Nilsson, 2016).

For the ENS sub-model, sharp notches have been rounded off with a radius to avoid stress singularities (Al-Emrani & Aygül, 2014). Since all the flanges have a thickness larger than 5 mm, the weld toe has been rounded of with a radius of 1 mm. The mesh size has been even finer than the sub-model for SHSS analysis. Similarly to the SHSS model, the boundary conditions have been recreated where the new "cutting surfaces" in the ENS model are connected to the SHSS model. Lastly, the largest stress in the S-point has been collected.

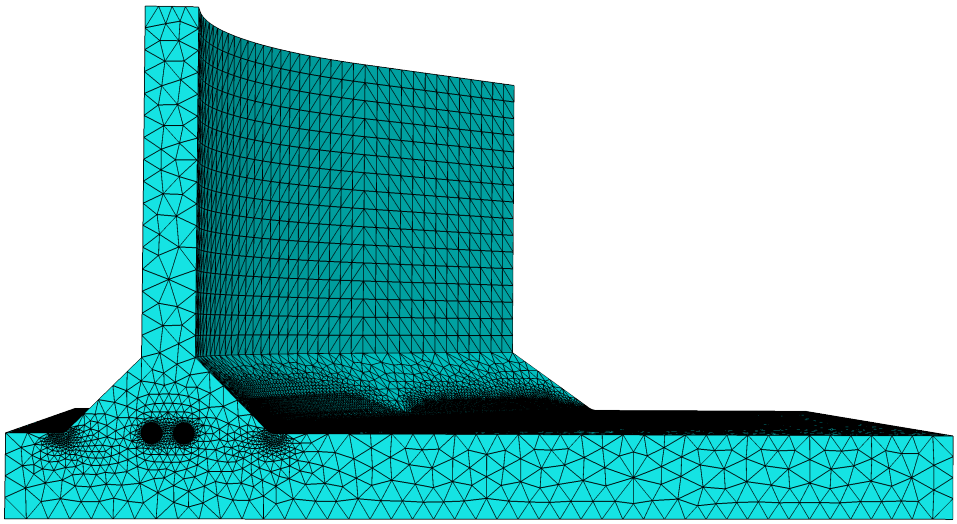

Figure 4.8: *Mesh sub-model for ENS analysis.*

4.2 Convergence study

A mesh convergence study has been done to verify that the mesh size of the elements required in the model are sufficient. Separate convergence studies have been completed on the global-, SHSS- and ENS model to receive accurate result. The convergence study has been approved when the mesh size in the models does not give large differences on the results. When the difference becomes less than 4% for global, 1% for SHSS and 1% for ENS, the mesh size is considered acceptable.

For all three models, there have been regions where the mesh has to be finer than other areas of the specimen. The mesh transition that appears from fine to coarse meshed areas have to be implemented gradually and smoothly. This is especially important in the vicinity of the welded area where the stress analyses have been carried out (Al-Emrani & Aygül, 2014). The element type that has been used for the analyses is 10-noded quadratic tetrahedral elements.

Global model
For the global model the convergence study of the CWG- and CWT specimen have been performed separately. For the CWG specimen the convergence study has been conducted by comparing the deflection and stress for two different mesh sizes. This has been done by creating an individual mesh convergence study for each of the global specimen. Even though the validation of deflection and stress have been sufficient, the area of interest for the fatigue analysis is the welded detail in the web to flange connection. Therefore, the mesh size of the flange is of greater importance to capture the stress distribution in the vicinity of the weld , see Table 4.5.

For the CWT specimen, the convergence study has been performed on Tong et al.'s (2024) CWT specimen with a bending radius of 30 mm. The conclusion has been implemented on all the CWT specimen, see Table 4.6.

Table 4.5: *Convergence study on CWG specimen, Global model .*

Global model	Mesh size web $[mm]$	Mesh size flange $[mm]$	U3 $[mm]$	Difference [%]	S11 $[MPa]$	Difference [%]
Sherif A. Ibrahim (2001)	100	81	30.094	2.24%	360.592	2.99%
		9	30.785		371.701	
Sause et al. (2003	100	120	2.169	1.36%	42.118	3.26%
		60	2.199		40.789	
Kövesdi & Dunai (2014)	100	60	13.629	0.78%	152.061	1.34%
		30	13.736		150.053	
Tong et al. (2024), CWG	100	60	6.661	2.63%	187.442	1.30%
		15	6.841		189.918	

Table 4.6: *Convergence study on CWT specimen, Global model .*

Mesh size $[mm]$	Nr. of elements on flange	Nr. of elements on global-model	Stress $[MPa]$	Difference [%]
10	1	5925	140.3338	
5	2	40496	139.477	0.61%
3	3	149983	137.4547	1.45%
2	4	477043	137.4119	0.03%

Sub-model (SHSS-model)
The sub-model used to find the SHSS, is constituted of a smaller part of the global model. This allows the ability to perform a finer mesh around the investigated area with less computation time. The convergence study has been performed on Tong et al.'s (2024) CWT specimen with a bending radius of 30 mm. Since the geometry of the sub-model is similar for all the authors, the approach developed during the convergence study are general and has been applied to all models.
The convergence study on the sub-model can be seen in Table 4.7 and clarified in Figure 4.9.

The guidelines concluded can be seen below and clarified in Figure 4.9

- At least 3 elements have to fit in the area between weld toe and 0.4t.
- At least 4 elements have to fit in the area between 0.4t and 0.9t.
- At least 2 elements have to fit in the area between 0.9t and 1.4t.
- At least 4 elements through the thickness of the flange.

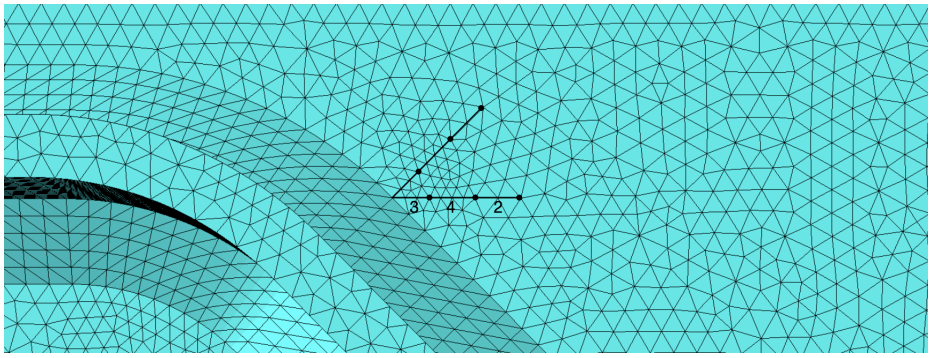

Figure 4.9: *Quadratic partition for SHSS.*

Table 4.7: *Convergence study on SHSS model, quadratic extrapolation.*

Mesh size [mm]	Distance	Nr. of elements in partition	Nr. of elements on sub-model	Nr. of elements in flange	SHSS [MPa]	Difference [%]
2	0.4t	2	148527	4	240.471	
	0.9t	3				
	1.4t	2				
2	0.4t	3	148527	4	242.482	0.83%
	0.9t	4				
	1.4t	2				
2	0.4t	4	148527	4	244.766	0.93%
	0.9t	4				
	1.4t	2				

Sub-sub-model (ENS-model)

The smallest sub-model, based on the SHSS sub-model is regarding the ENS analysis. It contains even more details and requires even finer mesh at the investigated area. The convergence study has once again been performed on Tong et al.'s (2024) CWT specimen with a bending radius of 30 mm. The geometry of the sub-model is similar for all tests, therefore the approach developed during the convergence study is general and has been applied to all models. Through the convergence study, see Table 4.8, the following guidelines have been summarised and further clarified in Figure 4.10:

- The element size inside the root and toe should be 0.25 mm.
- The outer radius surrounding the root should be 1 mm.
- There has to be at least 4 elements through the thickness of the flange.

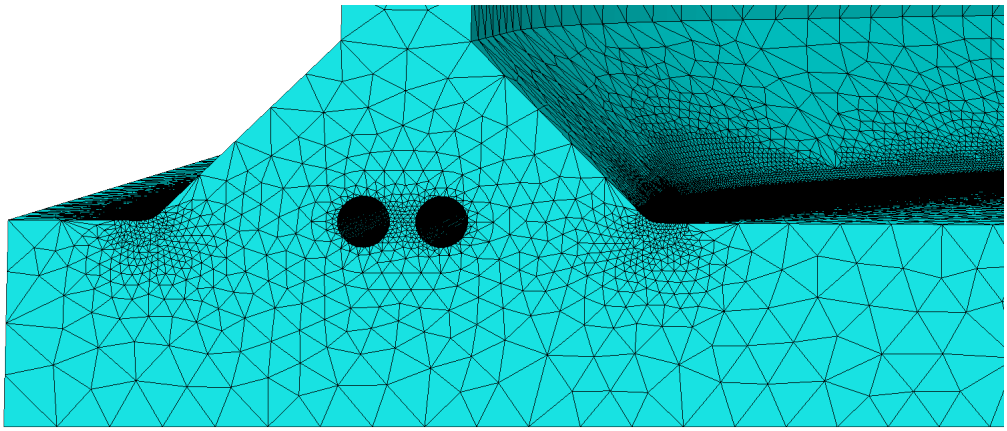

Figure 4.10: *Mesh size for ENS sub-model.*

Table 4.8: *Convergence study on ENS model.*

Mesh size [mm]	Mesh size toe [mm]	Mesh size inside root [mm]	Mesh size outside root [mm]	Nr. of elements on sub-model	Nr. of elements in flange	Max stress in S-Point [MPa]	Difference [%]
2	0.2	0.2	0.2	1061275	4	365.96	
2	0.25	0.25	0.25	713566	4	362.39	-0.99%
2	0.5	0.5	0.5	255518	4	360.26	-0.59%

4.3 Validation study

Different methods have been used to validate that the numerical models are consistent with the experimental specimen. This mainly depends on how much information and data that can be obtained from the various experiments. One verification model that has been used is that the comparison of stress and deflections found in the numerical models with analytical calculations. In Table 4.9, the numerical and analytical analysis has been compared. The analytical calculation can further be found in Appendix A.

Table 4.9: *Validation of numerical model using analytical analysis.*

Authors:	Study:	Deflection $[mm]$	Stress $[MPa]$
Sherif A. Ibrahim (2001)	Analytical analysis:	30.39	385.60
	Numerical analysis:	30.79	371.70
Difference [%]		1.3%	3.6%
Sause et al. (2003)	Analytical analysis:	1.95	35.51
	Numerical analysis:	2.20	40.79
Difference [%]		12.7%	14.9%
B. Kövesdi & L. Dunai (2014)	Analytical analysis:	13.79	159.41
	Numerical analysis:	13.74	150.05
Difference [%]		0.4%	5.9%
Tong et al. (2024)	Analytical analysis:	6.49	202.75
	Numerical analysis:	6.84	189.92
Difference [%]		5.4%	6.3%

From Table 4.9 it can be seen that Sause et al. (2003) had slightly larger difference between the analytical and numerical analysis than the rest of the authors. This could be due to the lateral supports modelled in the FE-model which affects the structural behaviour of the girder. In the analytical calculation these affects are not considered which affects the difference between the analytical and numerical results.

The CWT experiment from Tong et al. (2024), collected the stresses through strain gauges attached on the specimen, see Figure 4.11 for the position of the strain gauges. By comparing these stresses with the numerical model for the same location, the model has been verified, see Table 4.10.

Table 4.10: *Validation of numerical model using strain gauges.*

Authors:	Strain gauges	Experiment result: [MPa]	Numerical analysis: [MPa]	Difference [%]
Tong et al. (2024) CWT, R30	S1	192	194.96	-2%
		176	179.48	-2%
		157	155.74	1%
		136	132.92	2%
	S2	247	207.51	16%
		262	203.99	22%
		273	199.98	27%
		254	189.95	25%
	S3	290	212.3	27%
		283	205.73	27%
Tong et al. (2024) CWT, R60	S1	181	193.36	-7%
		175	178.28	-2%
		156	158.18	-1%
		139	134.57	3%
	S2	251	190.93	24%
		280	200.52	28%
		253	198.48	22%

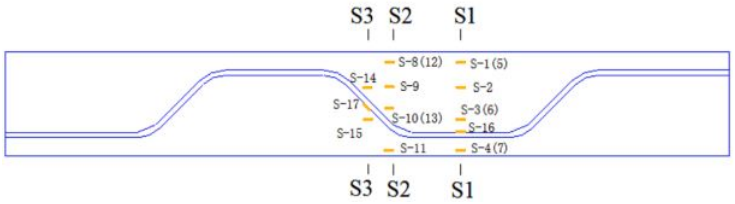

Figure 4.11: *Location of strain gauges on CWT specimen, (Tong et al., 2024).*

The validation results from Table 4.10 show that from the strain gauges used for static analysis, only the location S1 converged, the stress at which is same in both experimental and numerical studies. S2 and S3 did not converge, to ensure that the numerical model is correct, Tong et al. (2024) also produced structural hot-spot stresses based on the experiment. By comparing these stresses for all the specimens, the validation converged, 4.11.

Table 4.11: *Validation of SHSS numerical model using strain gauges.*

Specimen:	Experimental SHSS [MPa]	Numerical SHSS [MPa]	Difference [%]
R30-1	326	347.4	6.6%
R30-2	310	330	6.5%
R30-3	293	312.7	6.7%
R30-4	277	295.3	6.6%
R30-5	261	277.9	6.5%
R30-6	253	269.3	6.4%
R30-7	249	265.8	6.7%
R30-8	246	262.3	6.6%
R30-9	245	260.6	6.4%
R30-10	228	243.2	6.7%
R60-1	308	302.8	1.7%
R60-2	296	290.7	1.8%
R60-3	285	280.1	1.7%
R60-4	283	278.6	1.6%
R60-5	270	264.9	1.9%
R60-6	266	261.9	1.5%
R60-7	254	249.8	1.7%
R60-8	249	245.2	1.5%
R60-9	248	243.7	1.7%
R60-10	240	236.2	1.6%

Wang et al. (2013a) provided insufficient information verify the model. To solve the problem, the same modelling technique used on the CWT specimen from Tong et al. (2024) has been implemented on the specimen from Wang et al. (2013a).

4.4 SHSS Extrapolation study

As mentioned in Chapter 2.3.2, there are two extrapolation methods to use to find the structural hot-spot stress. An analysis has therefore been done on Tong et al.'s (2024) on CWT specimen having a bending radius of 30 mm. The numerical analysis for both the linear- and the quadratic extrapolation have been performed with fine mesh. According to Table 4.12, the structural hot-spot stress found from quadratic extrapolation is larger than the stress found from linear extrapolation.

Table 4.12: *SHSS extrapolation analyses.*

	Linear extrapolation	
	S_{11} [MPa]	$S_{principal}$ [MPa]
SHSS	225.96	228
	Quadratic extrapolation	
	S_{11} [MPa]	$S_{principal}$ [MPa]
SHSS	242.48	245.29

Therefore, for the following numerical analyses of the specimens, only quadratic extrapolation has been performed to receive the SHSS.

4.5 Evaluated stress components

As mentioned in the state-of-the-art, different stresses are needed in various stress methods. This has further been applied in the numerical models to finally conduct the stress components of interest.

Global model
For the global model, a path along the width of the flange has been created. If the location of the fatigue crack is known, the path has been created there. If not, two paths have been placed in the constant bending zone of the beam for both where the web is parallel and where the web is inclined. All the longitudinal stresses in the x-direction (S_{11}) located in the elements along the path have been collected to lastly found the average stress. For each sub-model, a stress concentration factor has been calculated based on the nominal stress (S_{11}) from the global model.

Sub-model
A crack appears perpendicular to the stresses. A few studies like Sause et al. (2003) showed that the fatigue crack initiates at the S-point grows a few millimetres along the weld before changing direction towards the edge of the flange. From this crack pattern, it can be seen that two different coordinate systems are of interest. From the global coordinate system, the stress component in x-direction (S_{11}) and the maximum principal stress ($S_{principal}$) has been extracted. Additionally, the von Mises stress ($S_{VonMises}$) has been collected for ENS. Considering the local coordinate system, the weld detail is subjected to normal stress perpendicular to the weld (S'_{11}) and the shear stress (S'_{12}) meaning it is multi-axially fatigue-loaded, see Figure 4.12.

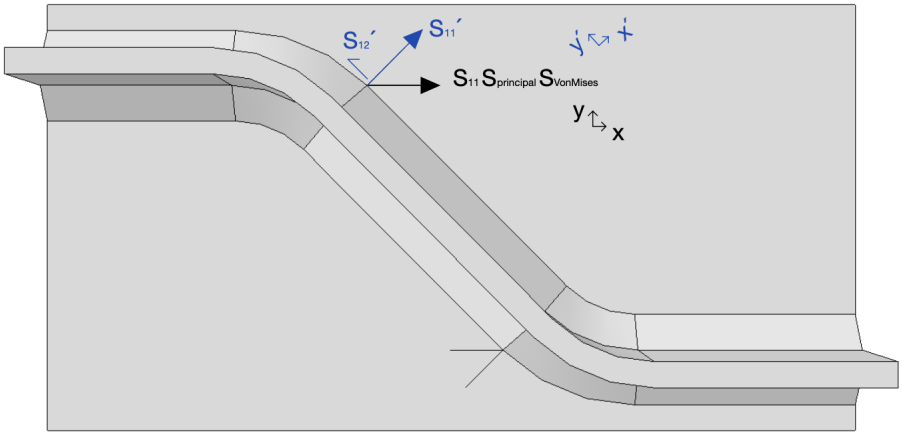

Figure 4.12: *The global- and local coordinate system used in the sub-models.*

The multi-axial stress state can be taken into account in three different ways, either by collecting the $S_{principal}$ and $S_{VonMises}$ from the global coordinate system, or through an interaction equation (see Equation 4.1) where the (S'_{11}) and (S'_{12}) from the local coordinate system are evaluated (Pedersen, 2015).

$$(\frac{\Delta\sigma_x}{\Delta\sigma_R})^3 + (\frac{\Delta\tau_{xy}}{\Delta\tau_R})^5 \leq D \tag{4.1}$$

$\Delta\sigma_x$, normal stress $[MPa]$
$\Delta\sigma_R$, normal stress fatigue strength $[MPa]$
$\Delta\tau_{xy}$, shear stress $[MPa]$
$\Delta\tau_R$, shear stress fatigue strength $[MPa]$
D, damage

In Equation 4.1, $\Delta\sigma_x$ corresponds to S_{11} and $\Delta\tau_{xy}$ is S_{12}.

Both in the sub-model for SHSS and ENS, the two different coordinate systems have been used to collect the stress components mentioned previously. For SHSS, the reference stresses for the quadratic extrapolation points have been collected and through Equation 2.7, the SHSS has been derived. However, for ENS the largest stresses have directly been obtained from the S-point.

4.6 Numerical analysis implemented on experimental S-N curves

Through the global-, SHSS- and ENS-model stresses have been found for the investigated area. A numerical modelling has been done for each experiment, meaning one model results in one value. However, some of the authors have performed several experiments on the same specimen geometry and received different results. In order to compare the numerical model with the experimental test, the stresses obtained from the nominal-, SHSS- and ENS model has been recalculated using a stress concentration factor (SCF), see Equation 4.2-4.4, and then multiplied with the nominal stress from the experimental results, see Equation 4.5 and 4.6. S-N curves have been plotted for each stress and fatigue life respectively. These new stresses with the corresponding number of cycles are further analysed in the results.

$$SCF_{nom} = \frac{\sigma_{global}}{\sigma_{nomFE}} \tag{4.2}$$

$$SCF_{SHSS} = \frac{\sigma_{SHSS}}{\sigma_{nomFE}} \tag{4.3}$$

$$SCF_{ENS} = \frac{\sigma_{ENS}}{\sigma_{nomFE}} \tag{4.4}$$

$$\Delta\sigma_{SHSS} = SCF_{SHSS} \cdot \Delta\sigma_{nom} \tag{4.5}$$

$$\Delta\sigma_{ENS} = SCF_{ENS} \cdot \Delta\sigma_{nom} \tag{4.6}$$

σ_{nomFE}, nominal stress received from the numerical global model $[MPa]$
σ_{SHSS}, stress from investigated area in SHSS-model $[MPa]$
σ_{ENS}, stress from investigated area in ENS-model $[MPa]$
$\Delta\sigma_{nom}$, stress range from experiment $[MPa]$

5 Results

The following chapter presents the results obtained from the numerical analysis described in Chapter 4. The following chapter consists of an evaluation of the fatigue life on the corrugated web girders based on the three methods; nominal stress, structural hot-spot stress and lastly effective notch stress. The effects of geometrical parameters including bending radius (R) and corrugation angle (θ) have also been evaluated based on the nominal method and local approach SHSS.

The stresses obtained from the numerical analysis explained in Chapter 4, and presented in following Chapter 5 can be found in Appendix C.

5.1 Evaluation of all specimens with corrugated web with Nominal-, Structural Hot-spot and Effective notch stress method

All the results obtained from the numerical analysis have been plotted in stress range vs. fatigue life plot. For each S-N curve, the associated DC recommended from Eurocode has been added and the standard deviation (STD) has been calculated to evaluate the scatter, see Table 5.1 for the compiled results.

The nominal stresses obtained from the fatigue experiments performed on the corrugated web specimen have once again been plotted in a stress range vs. fatigue life plot, see Figure 5.1. Unlike the graph derived in Chapter 3.3.1, where all beams have been included, only some of the specimens (mentioned in Chapter 4) have been further analysed. The specimens that failed due to other reasons than fatigue or achieved "run out" have been excluded from the graph, see Figure 5.1. The results shows that the result lies above DC100 and has a standard deviation of 0.147.

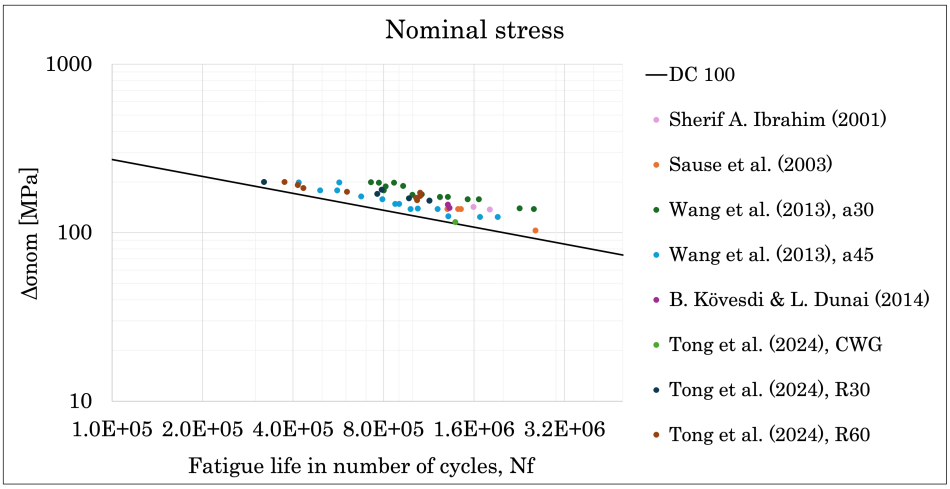

Figure 5.1: *S-N curve for experimental data with nominal stress (S_{nom}).*

The structural hot-spot stress has been obtained by creating a sub-model from the global model. The stress in the vicinity of the weld has further been derived through quadratic extrapolation.

The result received for the SHSS are based on two stresses from the global coordinate system, the principal stress ($S_{principal}$) and stress component in x-direction (S_{11}). By plotting the stresses in separate S-N curves, the result shows that the stresses are almost identical, slightly larger for $S_{prinicpal}$. Since $S_{prinicpal}$ includes the multi-axial response that appears in the S-point it will be investigated further,

see Figure 5.2. The standard deviation 0.121 decreased due to considering the weld geometry.

The recommended detail category mentioned in Eurocode (EN1993-1-9, 2005) DC100, can be seen as very low in the case for corrugated web, see Figure 5.2. Instead DC160 is to recommend being more accurate.

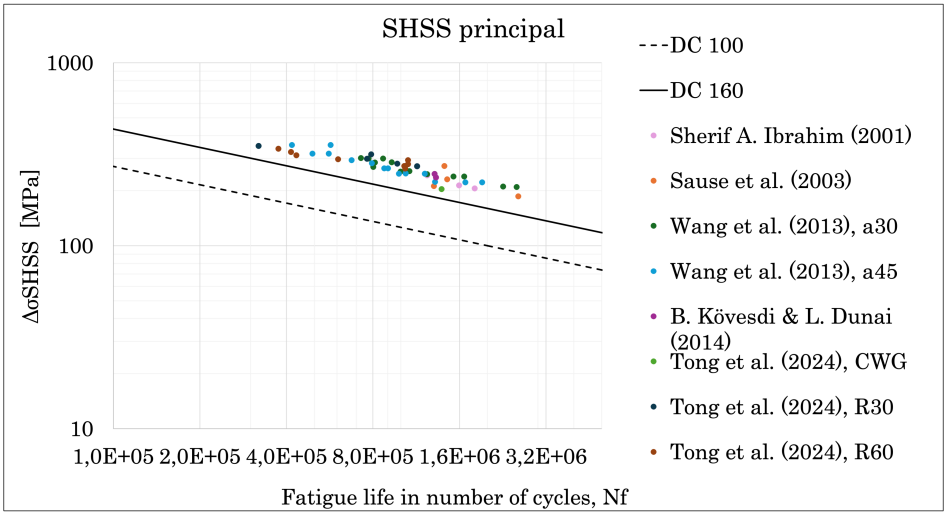

Figure 5.2: *S-N curve for experimental data with SHSS ($S_{principal}$) from FE-result.*

By creating an even smaller sub-model in the Abaqus, the effective notch stresses have been found. The sub-sub-model contains more details for the weld, like the weld notch.

The results received for ENS are the principal stress ($S_{principal}$) and von Mises stress ($S_{VonMises}$), see Figures 5.3 and 5.4. The stress component in x-direction (S_{11}) was also extracted, but smaller than the other stress components. As mentioned in Chapter 2 the stress components of interest in the effective notch stress method are ($S_{principal}$) and ($S_{VonMises}$), therefore these stresses have been further investigated.

For the S-N curve of ENS ($S_{principal}$), the detail category DC225 recommended from IIW appears to be applicable. Further it can be seen that the standard deviation increases to 0.166. In regards to the result for ENS ($S_{VonMises}$), the detail category DC200 recommended from IIW appears to be applicable, and the standard deviation was calculated to 0.159.

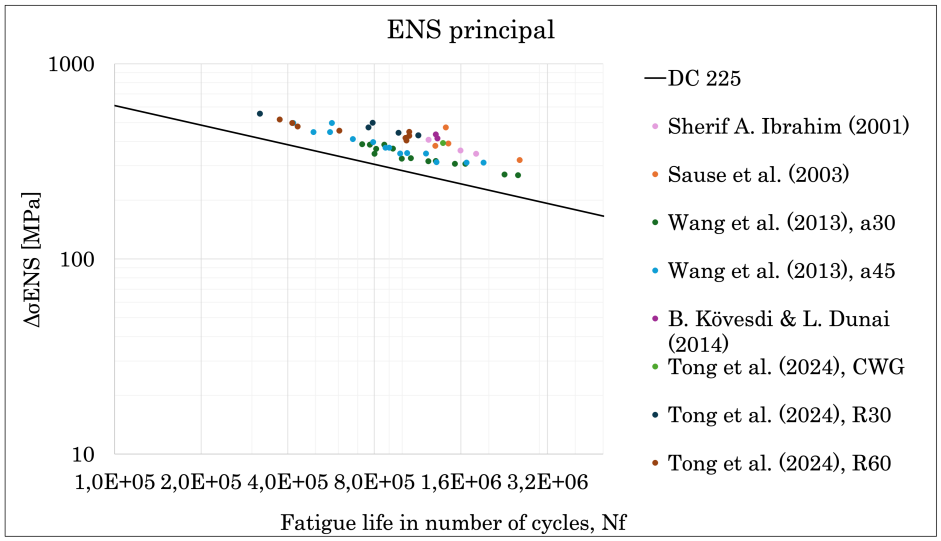

Figure 5.3: *S-N curve for experimental data with ENS ($S_{principal}$) from FE-result.*

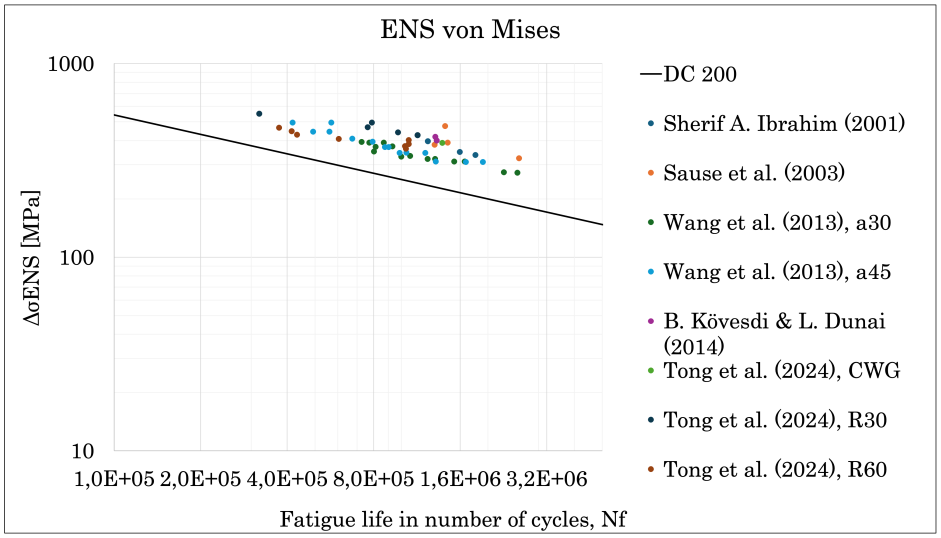

Figure 5.4: *S-N curve for experimental data with ENS ($S_{VonMises}$) from FE-result.*

The compiled result of the standard deviation and detail category used in Figure 5.1- 5.4 can be seen in Table 5.1. The DC are recommended from Eurocode for SHSS and IIW for ENS.

Table 5.1: *All the results summarized of standard deviation and DC for the specimens.*

	Nominal stress	SSHS $S_{prinicpal}$	ENS $S_{prinicpal}$	ENS $S_{VonMises}$
Standard deviation	0.147	0.121	0.166	0.159
DC	100	160	225	200

5.2 Evaluation of geometric parameters

As mentioned in the state-of-the-art, Chapter 2, the geometrical parameters have a large influence on the fatigue life. Based on the conclusion drawn from previous authors in Section 3.4, changing the bending radius and corrugation angle has the largest influence on the fatigue life. Therefore, the following result has been divided into subsections regarding the geometrical parameters: bending radius (R) and corrugation angle (θ).

In order to evaluate the scatter in the S-N curves, the standard deviation (STD) has been calculated. Also, the data points can be allocated to a straight regression line expressed as in Equation 5.1 on a $\log - \log$ S-N curve, with a slope of $m = 3$ (Drebenstedt & Euler, 2018). This linear regression line is the mean of the evaluated data points.

$$log\hat{N} = \log \hat{a} - m \cdot \log S \tag{5.1}$$

To achieve the lower bound of the plotted results the equation has been modified see Equation 5.2 (Sause et al., 2003).

$$log\hat{N} = (\log \hat{a} - 1.96 \cdot S) - m \cdot \log S \tag{5.2}$$

In Section 5.1 the evaluation of all specimens showed that the standard deviation decreased between the nominal stresses and SHSS. However, the standard deviation increased from SHSS to ENS and therefore ENS has been excluded from further evaluations. Therefore, following results are based on nominal stress and SHSS.

5.2.1 Bending radius, R

In order to see the effect of the bending radius, specimens having similar corrugation angle has been plotted together, see Table 5.2. Two different plots have been created. The first contains the CWT specimen from Tong et al. (2024), where the bending radius is either $R = 30mm$ or $R = 60mm$ with a fixed corrugation angle of $\theta = 45°$. The second category has a corrugation angle of $\theta = 36.9°$ including the specimens tested by Ibrahim (2001) and Sause et al. (2003), where the bending radius is $R = 27mm$ for Ibrahim and $R = 120mm$ for Sause et al.

For each category, the nominal stress and SHSS have been plotted to investigate the fatigue strength. For each S-N curve the standard deviation, mean regression line and lower bound has been presented.

Table 5.2: *Evaluation of bending radius for different stress models.*

Nominal stress		
	Tong et al. (2024)	Ibrahim (2001) and Sause et al. (2003)
	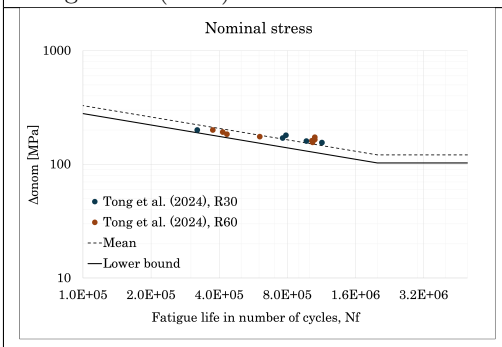	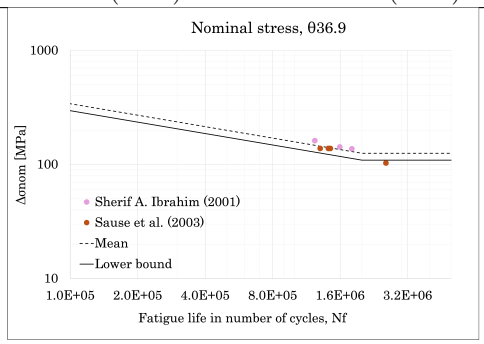
Standard deviation	0.108	0.093
Mean	$12.55 - 3 \cdot \log S$	$12.60 - 3 \cdot \log S$
Lower bound	$12.34 - 3 \cdot \log S$	$12.42 - 3 \cdot \log S$
DC	102	109
SHSS, $S_{principal}$		
	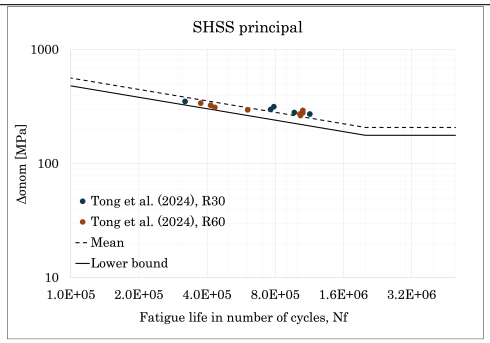	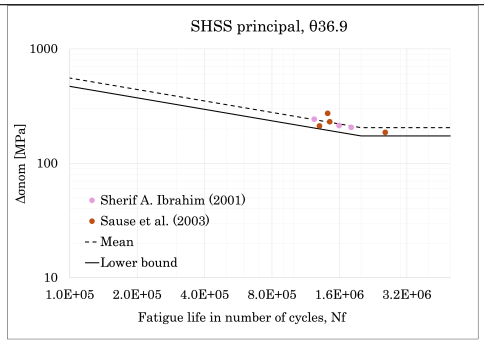
Standard deviation	0.105	0.111
Mean	$13.26 - 3 \cdot \log S$	$13.24 - 3 \cdot \log S$
Lower bound	$13.05 - 3 \cdot \log S$	$13.02 - 3 \cdot \log S$
DC	178	174

From the results of Tong et al.'s (2024) CWT specimens (see Table 5.2), the nominal stress gave a standard deviation of 0.108, and for SHSS the standard deviation decreased to 0.105. The standard deviation is very close between the stress methods, therefore the geometrical effect from the bending radius is consider to be small in this case. Therefore the scatter from fatigue testing has a larger impact than geometrical effect from the bending radius. The mean and lower bound curves increased between the nominal stress and SHSS which indicates a higher fatigue strength for SHSS. The detail category for nominal stress is DC102 and DC178 for SHSS.

In order to further evaluate the scatter coming from the bending radius, the CWG's tested by Ibrahim (2001) and Sause et al. (2003) was evaluated. As for Tong et al. (2024), the scatter from fatigue testing is larger than the geometrical effects from the bending radius. The detail categories are DC109 and DC174 for nominal stress and SHSS, respectively.

5.2.2 Corrugation angle, θ

The corrugation angle has been investigated by plotting specimens having the same bending radius with varying corrugation angles in the same graph, see Table 5.3. The plot has been divided into two categories. The first contains the CWT specimen from Wang et al. (2013a) where the corrugation angle is either $\theta = 30°$ or $\theta = 45°$ and the bending radius is fixed to $R = 60mm$. The second category also has the bending radius of $R = 60mm$ and containing the specimens tested by Wang et al. (2013a), Kövesdi & Dunai (2014) and Tong et al. (2024).

With similar bending radius in the S-N plots, the scatter that appears is based on the corrugation angle θ. For each category, the nominal stress and SHSS have been plotted to investigate the fatigue strength. For each S-N curve the standard deviation, mean regression line and lower bound have been presented.

Table 5.3: *Evaluation of corrugation angle for different stress models.*

Nominal stress		
	Wang et al. (2013a)	R60
	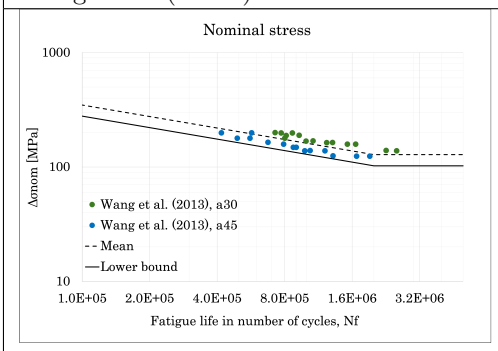	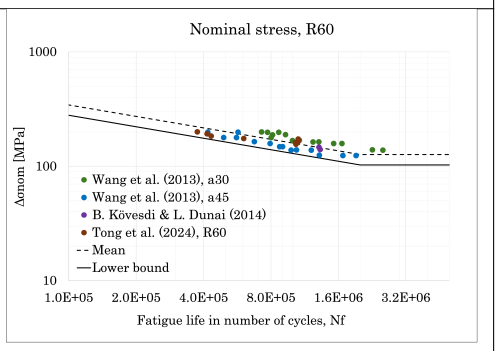
Standard deviation	0.149	0.139
Mean	$12.62 - 3 \cdot \log S$	$12.61 - 3 \cdot \log S$
Lower bound	$12.33 - 3 \cdot \log S$	$12.34 - 3 \cdot \log S$
DC	103	103
SHSS, $S_{principal}$		
	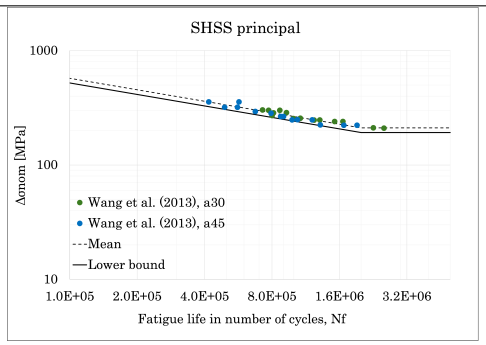	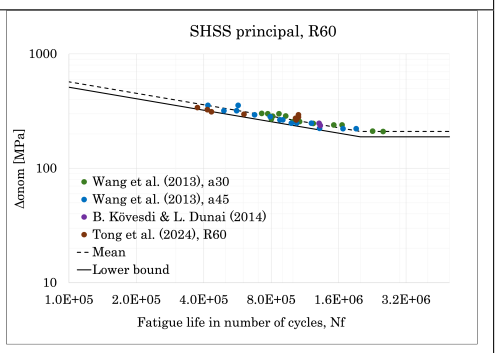
Standard deviation	0.063	0.073
Mean	$13.27 - 3 \cdot \log S$	$13.27 - 3 \cdot \log S$
Lower bound	$13.15 - 3 \cdot \log S$	$13.13 - 3 \cdot \log S$
DC	192	188

From the results of Wang et al.'s (2013a) CWT specimens (see Table 5.3) the nominal stress gave a standard deviation of 0.149, and for SHSS the standard deviation decreased to 0.063. The standard

deviation shows a big difference between the stress methods, meaning that the geometrical effect from the corrugation angle has a large effect on the scatter. Further it can be seen that the corrugation angle has a larger impact on the standard deviation than the bending radius stated in previous section. The mean and lower bound curves increased between the nominal stress and SHSS which indicates a higher fatigue strength for SHSS. The detail category for nominal stress is DC103 and DC192 for SHSS.

To ensure the consistency of results, all CWT and CWG specimen having R 60 mm was evaluated. The standard deviation decreases between nominal stress and SHSS, now from 0.139 to 0.073, which amplifies the conclusion made on Wang et al.'s (2013a) CWT specimens. This shows the geometrical effect coming from the corrugation angle since the corrugation angles plotted are $\theta = 30°$, $\theta = 39°$ and $\theta = 45°$. As for Wang et al. (2013a), the mean and lower bound curves increases between the two stress methods. Lastly, the detail category for nominal stress became DC103 and DC188 for SHSS.

Since the geometrical effect coming from the corrugation angle was shown to be considerable, the results from the nominal stresses has been divided into three different detail categories based on the corrugation angle. Visualized in Figure 5.5a; corrugation angle $\theta = 30°$ gives DC131, $\theta = 39°$ DC118 and $\theta = 45°$ DC101. However, using the SHSS method, the detail categories for different corrugation angles are presented in Figure 5.5b; corrugation angle $\theta = 30°$ gives DC199, $\theta = 39°$ DC199 and $\theta = 45°$ DC177. For corrugation angle 45° the standard deviation is larger being 0.10 compared to $\theta = 30°$ having a standard deviation of 0.05 and $\theta = 39°$ having a standard deviation of 0.04. This is because $\theta = 45°$ category includes the CWT specimens with R 60 mm from Tong et al. (2024) which showed large scatter from fatigue testing. This could be the reason for the differences in detail categories for different corrugation angles in SHSS. In Figure 5.6 the different corrugation angles are presented.

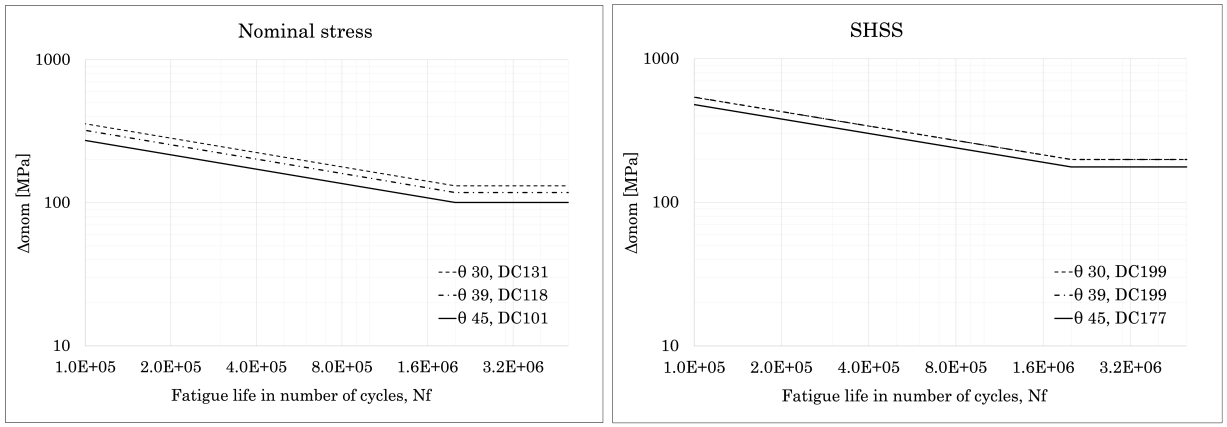

(a) *Detail category for corrugation angle $\theta = 30°$, 39° and 45° based on nominal stresses.*

(b) *Detail category for corrugation angle $\theta = 30°$, 39° and 45° based on SHSS.*

Figure 5.5: *Detail category for different corrugation angles using nominal stress method and SHSS method.*

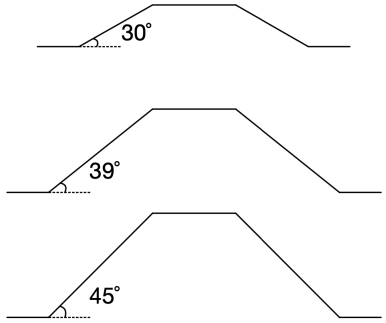

Figure 5.6: *Corrugation angle* $\theta = 30^\circ$ *,* 39° *and* 45°*.*

6 Discussion

Throughout the thesis, observations have been obtained regarding the corrugated web girders and different fatigue design methods. Based on the observations made during the thesis, results and uncertainties will be analysed and discussed in the following chapter.

6.1 Reliability of the FE studies

The specimens were modelled to study the structural behaviour obtained in the experimental studies in more detail. However, to obtain a FE model that mimics the experiments, some assumptions have been required since there was a lack of information reported regarding the experiments. A validation has been performed to verify that the assumptions regarding the boundary conditions and type of loading are sufficient and lastly to ensure the reliability of the model.

Further, to obtain a result corresponding to the experiment, the stresses must be collected for the same location where the experimental specimen cracked. However, this depends on the amount of information provided on where the fatigue crack appears. Not all authors has explained such, instead the location having the largest stress has been identified and further analysed.

In Chapter 2.2.3 it is stated that the detail category for a longitudinal weld is DC125. Based on the results on nominal stresses, DC131 for corrugation angle $\theta = 30°$ was obtained. Which exceeds the upper limit of the detail category for an inclined weld. This could depend on the limited amount of specimens evaluated in the thesis.

6.2 The use of sub-models

The sub-models are an useful tool to capture the stress concentrations at the welded detail of the web-to-flange connection. The purpose of the sub-models is to capture the weld geometry and the stress concentrations appearing due to the geometric discontinuities. Sub-modelling results in a smaller part that needs to be meshed, which could reduce computational time. However, depending on the chosen stress method, the mesh density might still be rather high, which in turn affects the computational time. Therefore, the sub-model should be sufficient enough to capture the stress concentration, with a reasonable mesh size and computational time.

6.3 Linear extrapolation vs quadratic extrapolation for SHSS evaluation

To evaluate the structural hot-spot stress that appears by the weld toe, two different extrapolation methods have been investigated, linear- and quadratic extrapolation. The main difference has been the number of reference points used to find the SHSS. The conclusion obtained in Section 4.4 was that the quadratic extrapolation having three reference points gave a slightly larger stress compared to the linear extrapolation with two reference points. Table 6.1, presents that the $S_{principal}$ stress is 7.05% larger when using quadratic compared to linear extrapolation. According to Al-Emrani and Aygül (2014), linear extrapolation may lead to non-conservative results in some cases and the more accurate method with quadratic extrapolation procedure is recommended. Therefore, the quadratic extrapolation method was used.

Table 6.1: *SHSS extrapolation analysis for Tong et al's (2024) CWT R30.*

	Linear extrapolation, $S_{principal}$ [MPa]	Quadratic extrapolation $S_{principal}$ [MPa]	Difference [%]
Tong et al. (2024), CWT, R30	228.0	245.3	7.05%

6.4 Stress components S_{11} and $S_{principal}$ in SHSS

In Section 2.3.2 it is stated that in an multi-axial stress state, the maximum principal stress should be used if the angle between the maximum principal stress and the normal vector to the weld is less than 60° and if the angle is larger than 60°, the stress perpendicular to the weld should be used, see Figure 2.11a and Figure 2.11b.

The results shows that the maximum principal stress and S_{11} is very close and has less than 1% difference in Table 6.2. Which means that the maximum principal stress has the same direction as S_{11} and both can be used for the assessment of the fatigue life.

Since all the girders in this thesis have a corrugation angle in the range $\theta = 30° - 45°$ the angle between the principal stress and ther normal to the weld will be less than 60° and both $S_{principal}$ or S_{11} can be used.

Table 6.2: *Stress comparison for Tong et al.'s (2024) CWG.*

	S_{11} [MPa]	$S_{principal}$ [MPa]	Difference [%]
Tong et al. (2024), CWG	202.3	204.1	0.90 %

7 Conclusion

The aim of this thesis was to analyse different stress methods used for evaluating the fatigue strength of corrugated web girders. Due to the lack of information regarding these stress methods in Eurocode, the nominal stress-, structural hot-spot stress-, and effective notch stress method have been investigated. Further, the geometrical parameters, including bending radius and corrugation angle was analysed separately. The following conclusions are based on the result in Chapter 5 and are presented in Section 7.1. Also, suggestions for further studies are presented in Section 7.2

7.1 Concluding remarks

In the following section, concluding remarks have been made and are presented in bullet lists. The conclusions have been divided into three categories, detail categories, geometrical parameters and local approaches.

Detail categories

- Based on the nominal stress method, the results for the corrugated web girders fit well with DC100.
- If nominal stresses are to be used, the fatigue strength can be determined by DC131 for corrugation angle 30°, DC118 for corrugation angle 39° and DC101 for corrugation angle 45°.
- The results from structural hot-spot stress method for principal stresses fit well with DC160, so using DC100 as proposed in Eurocode would be very conservative.
- The results fit well with DC225 for principal stress using the effective notch stress method.
- The results fit well with DC200 for von Mises stress using the effective notch stress method.

Geometrical parameters

- Based on the result of the scatter, the geometrical effects from the corrugation angle on the fatigue life are more considerable in comparison to the bending radius.

Local approaches

- In regards to the finite element modelling in SHSS, quadratic extrapolation, the number of elements 3, 4 and 2 between each reference points $0.4t$, $0.9t$ and $1.4t$ respectively, was considered sufficient enough.
- A remarkable decrease in the scatter appears when going from the nominal stress method to the SHSS method.
- In regards to the finite element modelling in ENS, the mesh size 0.25 mm at effective notch at the weld toe was suitable.
- The scatter increases between SHSS and ENS, which needs to be further investigated.
- The most representative method according to the results is SHSS with the lowest scatter.

7.2 Suggestions for further studies

- There are plenty of other geometrical parameters that have not been evaluated in this thesis. Other corrugation parameters could be further investigated using the effective notch stress method to see the effect of different parameters on the stress concentration factor.

- Also, other ranges of the corrugation angle and bending radius could be further evaluated.

- Due to the lack of time, the stresses from the local coordinate system was not fully investigated. For future studies it would be interesting to analyse the stress components from the local coordinate system.

- Further investigations on the effective notch stress method could be performed in order to evaluate the scatter and standard deviation resulting from this method.

References

Abbas, H. H., Sause, R., & Driver, R. G. (2007a). *Analysis of flange transverse bending of corrugated web i-girders under in-plane loads* [Article]. Auburn University, Lehigh Univeristy, and Univeristy of Alberta.

Abbas, H. H., Sause, R., & Driver, R. G. (2007b). *Simplified analysis of flange transverse bending of corrugated web i-girders under in-plane moment and shear* [Article]. Auburn University, Lehigh Univeristy, and Univeristy of Alberta.

Akhlaghi, F. Z. (2009). *Fatigue life assessment of welded bridge details using structural hot spot stress method: A numerical and experimental case study* [Master thesis]. Chalmers University of Technology.

Al-Emrani, M. (2023). *Steel structures* (Book). Chalmers Univeristy of Technology.

Al-Emrani, M., & Aygül, M. (2014). *Fatigue design of steel and composite bridges* [Article]. Chalmers University of Technology.

Anami, K., Sause, R., & Abbas, H. (2005). *Fatigue of web-flange weld of corrugated web girders: 1. influence of web corrugation geometry and flange geometry on web-flange weld toe stresses* [Article]. Kochi University of Lehigh University.

Baláž, I., & Koleková, Y. (2012). *Influence of transverse bending moment in the flange of corrugated i-girders* [Article]. Slovak Univeristy of Technology.

Chenung, M., & Li, W. (2003). *Probabilistic fatigue and fracture analyses of steel bridges.* [Article]. Department of Civil Engineering, University of Ottawa, Department of Civil, and Environmental Engineering, Carleton University. https://www.sciencedirect.com/science/article/pii/S016747300200067X?via%3Dihub

Drebenstedt, K., & Euler, M. (2018). *Statistical analysis of fatigue test data according to eurocode 3* [Article]. Institute of Structural Design, University of Stuttgart.

Elamary, A. S., Saddek, A. B., & Alwetaishi, M. (2017). *Effect of corrugated web on flexural capacity of steel beams.* https://www.ripublication.com/ijaer17/ijaerv12n4_09.pdf

EN1993-1-5. (2006). *Eurocode 3: Design of steel structures - part 1:5: Plated structural elements* (EN:1993-1-5). European Committee for Standardization.

EN1993-1-9. (2005). *Eurocode 3: Design of steel structures - part 1:9: Fatigue* (EN:1993-1-9). European Committee for Standardization.

Eriksson, K. (2010). *Utmattning av stålkonstruktioner enligt eurokod 3.* https://media.sbi.se/securepdfs/2020/02/Utmattning_stalkonstruktioner.pdf

Hobbacher, A. (2008). *Recommendations for fatigue desing of welded joints and components* [Article]. International Institute of Welding.

Hobbacher, A. F. (2016). *Recomendations for fatigue design of welded joints and components: Second edition* [Book]. International Institute of welding.

Ibrahim, S. A. (2001). *Fatigue analysis and instability problems of plate girders with corrugated webs* [Article]. Drexel University.

Ibrahim, S. A., El-Dakhakhni, W. W., & Elgaaly, M. (2006a). *Behavior of bridge girders with corrugated webs under monotonic and cyclic loading* [Article]. Ain Shams Univeristy, McMaster Univeristy, and Drexel Univeristy. https://doi.org/10.1016/j.engstruct.2006.03.026

Ibrahim, S. A., El-Dakhakhni, W. W., & Elgaaly, M. (2006b). *Fatigue of corrugated-web plate girders: Experimental study* [Article].

Jonsson, B., Dobmann, G., Hobbacher, A. F., Kassner, M., & Marquis, G. (2016). *Iiw guidelines on weld quality in relationship to fatigue strength.*

Karakas, Ö., Baumgartner, J., & Susmel, L. (2020). *On the use of a fictitious notch radius equal to 0.3 mm to design against fatigue welded joints made of wrought magnesium alloy az31* [Article]. Pamukkale Univeristy, Fraunhofer Institute for Structural Durability, System Reliability LBF, and The Univeristy of Sheffield. https://doi.org/10.1016/j.ijfatigue.2020.105747

Kotaki, N., Ichikawa, A., Sasaki, E., Miki, C., & Yasuzaka, T. (2003). *Proposal of ripple web and its fatigue strength* [Article]. Tokyo Institue of Technology.

Kövesdi, B., & Dunai, L. (2014). *Fatigue life of girders with trapzodially corrugated webs: An experimental study* [Article]. Budapest University of Technology and Economics.

Kövesdi, B., Jáger, B., & Dunai, L. (2012). *Stress distribution in the flanges of girders with corrugated webs* [Article]. Budapest Univeristy of Technology and Economics.

Lindqvist, A., & Nilsson, H. (2016). *Effective notch stress analysis of transverse attachments in steel bridges: A parametric fatigue life assessment* [Thesis]. Chalmers University of Technology.

Pedersen, M. (2015). *Multiaxial fatigue assessment of welded joints using the notch stress approach* [Article]. , Department of Energy Technology, Aalborg University.

Rodriguez, R. (2000). *Stress distribution and bearing stiffeners details related to fatigue and fracture of steel girders with corrugated webs* [Thesis]. Drexel University.

Sause, R., Abbas, H. H., Driver, R. G., Anami, K., & W.Fisher, J. (2003). *Fatigue resistance of corrugated web girders* [Article]. Lehigh University.

Sause, R., Anami, K., & Abbas, H. H. (2005). *Fatigue of web-flange weld of corrugated web girders: 1. influence of web corrugation geometry and flange geometry on web-flange weld toe stresses* [Article]. Kochi University of Technology and Lehigh University.

Save, E., & Åkermo, K. (2020). *Fatigue performance of welded steel girders with corrugated webs* [Master thesis]. Chalmers University of Technology.

Tong, L., Zhao, Z., Zuo, G., Wang, H., & Pan, C. (2024). *Experimental study on fatigue behavior of trapezoidal corrugated-web girders based on t-section members.* [Article]. Tongji University, Qianshan Steel Structure of Xingtai Road and Bridge Construction Co., China Construction Industrial Energy Engineering Group Co., Tongji Zhejiang College.

Wang, Z., Wang, Q., & Jiang, R. (2015). *Finite element based fatigue assessment of corrugated steel web beams in highway bridges* [Article]. Sichuan University.

Wang, Z., Wang, Q., & Tan, L. (2013a). *Fatigue strength evalutaion of welded structual details in corrugated steel web girders* [Article]. Sichuan University.

Wang, Z., Wang, Q., & Zhang, Y. (2013b). *Fatigue strength of longitudinal welded joints with steel corrugated plates* [Article]. Sichuan University.

Xu, J., Sun, H., Cai, S., Sun, W., & Zhang, B. (2019). *Fatigue testing and analysis of i-girders with trapezoidal corrugated webs* [Article]. Tongji University, Chongqing University, and Shanghai Municipal Maintenance Management Co.

A Calculations for validation of the FE models

Ibrahim (2001)

Beam subjected to four-point bending
Vertical deflection and stresses

Material parameters

$v := 0.3$ Poisson's ratio
$E := 200\ GPa$ Youngs's Modulus

$G := \frac{E}{2 \cdot (1+v)} = 76.923\ GPa$ Shear Modulus of elasticity

Geometry

$a_s := 2170\ mm$ Shear span
$b := 1519\ mm$ Distance between two load application points

$b_f := 150\ mm$ Width, flange
$t_f := 12.7\ mm$ Thickness, flange

$h_w := 500\ mm$ Height, web
$t_w := 3\ mm$ Thickness, web

$L_0 := 5859\ mm$ Distance between supports

$b_s := 150\ mm$ Width, stiffner
$t_s := 10\ mm$ Thickenss, stiffner

Sectional constants

$A_w := h_w \cdot t_w = 0.002\ m^2$ Area of corrugated web
$A_f := b_f \cdot L_0 = 0.879\ m^2$ Area of flange
$A_s := b_s \cdot t_s = 0.002\ m^2$ Area of stiffner

$I_R := \left(\frac{b_f \cdot {t_f}^3}{12} + (b_f \cdot t_f) \cdot \left(\frac{h_w}{2} + \frac{t_f}{2} \right)^2 \right) \cdot 2 = (2.504 \cdot 10^{-4})\ m^4$ Moment of inertia for the flanges (neglecting the contribution from the web)

Applied load

$P_{FE} := 178\ kN$ Assigned load in FE-model

$P := 2 \cdot P_{FE} = 356\ kN$ Total load applied on the beam

Deflection

$$\Delta := \frac{P \cdot a_s}{8 \cdot E \cdot I_R} \cdot \left(\frac{4}{3} \cdot a_s{}^2 + 2 \cdot a_s \cdot b + \frac{b^2}{2} \right) + \frac{\left(\frac{P}{2} \right) \cdot a_s}{G \cdot A_w} = 30.387 \ \textbf{mm}$$

$\Delta_{FE} := 30.785 \ \textbf{mm}$ Results from ABAQUS, U3

$diff_{deflection} := \frac{\Delta - \Delta_{FE}}{\Delta} \cdot 100 = -1.309$

Stresses

$\sigma_{applied} := \frac{P_{FE}}{A_s} = 118.667 \ \textbf{MPa}$ Stress applied in FE-model

$M_{max} := P_{FE} \cdot a_s = 386.26 \ \textbf{kN} \cdot \textbf{m}$ Four-point bending

$z := \frac{h_w}{2}$ Distance from the neutral axis to the top of the bottom flange

$\sigma := \frac{M_{max}}{I_R} \cdot z = 385.602 \ \textbf{MPa}$ Stresses at the top of the bottom flange

$\sigma_{FE} := 371.70 \ \textbf{MPa}$ Results from ABAQUS, S11

$diff_{stress} := \frac{\sigma - \sigma_{FE}}{\sigma} \cdot 100 = 3.605$

Measure stress at mid-span at top face of tension flange:
24.8 ksi = 171 MPa
(load of 40 kips = 178 kN)
Ibrahim 2001

Sause et al. (2003)

Material parameters

$v := 0.3$
$E := 202.5\ \mathit{GPa}$

$G := \frac{E}{2 \cdot (1+v)} = 77.885\ \mathit{GPa}$

Geometry

$L_0 := 7\ \mathit{m}$ distance between support

$bf := 227\ \mathit{mm}$ width flange
$tf := 20\ \mathit{mm}$ thickness flange
$hw := 1200\ \mathit{mm}$ height web
$tw := 6\ \mathit{mm}$ thickness web
$ts := 20\ \mathit{mm}$ thickness stiffner
$bs := 206\ \mathit{mm}$ width stiffner

$a1 := 2\ \mathit{m}$ shear span distance
$b_{load} := 3\ \mathit{m}$ distance between applied load

Sectional constants

$I_R := \left(\frac{bf \cdot tf^3}{12} + bf \cdot tf \cdot \left(\frac{hw}{2} + \frac{tf}{2} \right)^2 \right) \cdot 2 = 0.003\ \mathit{m}^4$

$Aw := hw \cdot tw = 0.007\ \mathit{m}^2$

$Af := tf \cdot bf = 0.005\ \mathit{m}^2$

$As := ts \cdot bs = 0.004\ \mathit{m}^2$

Applied load

$P_{FE} := 100\ \mathit{kN}$

$P := 2 \cdot P_{FE} = 200\ \mathit{kN}$

Deflection

$$\Delta := \frac{P \cdot a1}{8 \cdot E \cdot I_R} \cdot \left(\frac{4}{3} \cdot a1^2 + 2 \cdot a1 \cdot b_{load} + \frac{{b_{load}}^2}{2} \right) + \frac{\left(\frac{P}{2}\right) \cdot a1}{G \cdot Aw} = 1.952 \ mm$$

$\Delta_{FE} := 2.199 \ mm$ Results from Global model, Abaqus (U3)

$$diff_{\Delta} := \left(\frac{\Delta - \Delta_{FE}}{\Delta} \right) \cdot 100 = -12.648$$

Stresses

$\sigma_{applied} := \frac{P_{FE}}{As} = 24.272 \ MPa$ Stresses applied in FE-model

$M_{max} := P_{FE} \cdot a1 = 200 \ m \cdot kN$ Four point bending

$z := \frac{hw}{2} = 0.6 \ m$

$\sigma_{max} := \left(\frac{M_{max}}{I_R} \right) \cdot z = 35.514 \ MPa$ Stress at the top of the bottom flange

$\sigma_{FE} := 40.789 \ MPa$ Result from Global model, Abaqus (S11)

$$diff_{\sigma} := \left(\frac{\sigma_{max} - \sigma_{FE}}{\sigma_{max}} \right) \cdot 100 = -14.854$$

Sause et al. (2003)

Material parameters

$v := 0.3$
$E := 202.5\ \mathit{GPa}$

$G := \frac{E}{2 \cdot (1+v)} = 77.885\ \mathit{GPa}$

Geometry

$L_0 := 7\ \mathit{m}$ distance between support

$bf := 227\ \mathit{mm}$ width flange
$tf := 20\ \mathit{mm}$ thickness flange
$hw := 1200\ \mathit{mm}$ height web
$tw := 6\ \mathit{mm}$ thickness web
$ts := 20\ \mathit{mm}$ thickness stiffner
$bs := 206\ \mathit{mm}$ width stiffner

$a1 := 2\ \mathit{m}$ shear span distance
$b_{load} := 3\ \mathit{m}$ distance between applied load

Sectional constants

$I_R := \left(\frac{bf \cdot tf^3}{12} + bf \cdot tf \cdot \left(\frac{hw}{2} + \frac{tf}{2} \right)^2 \right) \cdot 2 = 0.003\ \mathit{m}^4$

$Aw := hw \cdot tw = 0.007\ \mathit{m}^2$

$Af := tf \cdot bf = 0.005\ \mathit{m}^2$

$As := ts \cdot bs = 0.004\ \mathit{m}^2$

Applied load

$P_{FE} := 100\ \mathit{kN}$

$P := 2 \cdot P_{FE} = 200\ \mathit{kN}$

Deflection

$$\Delta := \frac{P \cdot a1}{8 \cdot E \cdot I_R} \cdot \left(\frac{4}{3} \cdot a1^2 + 2 \cdot a1 \cdot b_{load} + \frac{{b_{load}}^2}{2} \right) + \frac{\left(\frac{P}{2}\right) \cdot a1}{G \cdot Aw} = 1.952 \ \textbf{mm}$$

$\Delta_{FE} := 2.199 \ \textbf{mm}$ Results from Global model, Abaqus (U3)

$$diff_{\Delta} := \left(\frac{\Delta - \Delta_{FE}}{\Delta} \right) \cdot 100 = -12.648$$

Stresses

$\sigma_{applied} := \frac{P_{FE}}{As} = 24.272 \ \textbf{MPa}$ Stresses applied in FE-model

$M_{max} := P_{FE} \cdot a1 = 200 \ \textbf{m} \cdot \textbf{kN}$ Four point bending

$z := \frac{hw}{2} = 0.6 \ \textbf{m}$

$\sigma_{max} := \left(\frac{M_{max}}{I_R} \right) \cdot z = 35.514 \ \textbf{MPa}$ Stress at the top of the bottom flange

$\sigma_{FE} := 40.789 \ \textbf{MPa}$ Result from Global model, Abaqus (S11)

$$diff_{\sigma} := \left(\frac{\sigma_{max} - \sigma_{FE}}{\sigma_{max}} \right) \cdot 100 = -14.854$$

Kövesdi et al. (2014)

Material parameters

$v := 0.3$
$E := 200\ \mathit{GPa}$

$G := \frac{E}{2 \cdot (1 + v)} = 76.923\ \mathit{GPa}$

Geometry

$L_0 := 6.750\ \mathit{m}$	distance between support
$bf := 225\ \mathit{mm}$	width flange
$tf := 20\ \mathit{mm}$	thickness flange
$hw := 500\ \mathit{mm}$	height web
$tw := 6\ \mathit{mm}$	thickness web
$ts := 6\ \mathit{mm}$	thickness stiffner
$bs := 225\ \mathit{mm}$	width stiffner

Sectional constants

$I_R := \left(\frac{bf \cdot tf^3}{12} + bf \cdot tf \cdot \left(\frac{hw}{2} + \frac{tf}{2} \right)^2 \right) \cdot 2 = \left(6.087 \cdot 10^{-4} \right)\ \mathit{m}^4$

$Aw := hw \cdot tw = 0.003\ \mathit{m}^2$

$Af := tf \cdot bf = 0.005\ \mathit{m}^2$

$As := ts \cdot bs = 0.001\ \mathit{m}^2$

Applied load

$P_{FE} := 230\ \mathit{kN}$

Deflection - 3 point bending

$$\Delta := \frac{P_{FE} \cdot {L_0}^3}{48 \cdot E \cdot I_R} + \frac{P_{FE} \cdot \frac{L_0}{2}}{2 \cdot G \cdot hw \cdot tw} = 13.787 \ mm$$

$\Delta_{FE} := 13.736 \ mm$ Results from Abaqus (U3)

$$diff_\Delta := \left(\frac{\Delta - \Delta_{FE}}{\Delta} \right) \cdot 100 = 0.369$$

Stresses

$\sigma_{applied} := \frac{P_{FE}}{As} = 170.37 \ MPa$ Stresses applied in FE-model

$M_{max} := P_{FE} \cdot \frac{L_0}{4} = 388.125 \ m \cdot kN$ Three point bending

$z := \frac{hw}{2} = 0.25 \ m$

$\sigma_{max} := \left(\frac{M_{max}}{I_R} \right) \cdot z = 159.407 \ MPa$ Stress at the top of the bottom flange

$\sigma_{FE} := 150.053 \ MPa$ Result from Abaqus (S11)

$$diff_\sigma := \left(\frac{\sigma_{max} - \sigma_{FE}}{\sigma_{max}} \right) \cdot 100 = 5.868$$

Tong et al. (2024) (CWG, Entire girder, 4-p bending)

Material parameters

$v := 0.3$
$E := 200\ \boldsymbol{GPa}$

$G := \frac{E}{2 \cdot (1 + v)} = 76.923\ \boldsymbol{GPa}$

Geometry

$L_0 := 3.420\ \boldsymbol{m}$ distance between support

$bf := 150\ \boldsymbol{mm}$ width flange
$tf := 16\ \boldsymbol{mm}$ thickness flange
$hw := 500\ \boldsymbol{mm}$ height web
$tw := 5\ \boldsymbol{mm}$ thickness web
$ts := 5\ \boldsymbol{mm}$ thickness stiffner
$bs := 150\ \boldsymbol{mm}$ width stiffner

$a1 := 1.08\ \boldsymbol{m}$ shear span distance
$b_{load} := 1.26\ \boldsymbol{m}$ distance between applied load

Sectional constants

$I_R := \left(\frac{bf \cdot tf^3}{12} + bf \cdot tf \cdot \left(\frac{hw}{2} + \frac{tf}{2} \right)^2 \right) \cdot 2 = \left(3.196 \cdot 10^{-4} \right)\ \boldsymbol{m^4}$

$Aw := hw \cdot tw = 0.003\ \boldsymbol{m^2}$

$Af := tf \cdot bf = 0.002\ \boldsymbol{m^2}$

$As := ts \cdot bs = \left(7.5 \cdot 10^{-4} \right)\ \boldsymbol{m^2}$

Applied load

$P_{FE} := 240\ \boldsymbol{kN}$

$P := 2 \cdot P_{FE} = 480\ \boldsymbol{kN}$

Deflection

$$\Delta := \frac{P \cdot a1}{8 \cdot E \cdot I_R} \cdot \left(\frac{4}{3} \cdot a1^2 + 2 \cdot a1 \cdot b_{load} + \frac{{b_{load}}^2}{2} \right) + \frac{\left(\frac{P}{2}\right) \cdot a1}{G \cdot Aw} = 6.488 \ mm$$

$\Delta_{FE} := 6.841 \ mm$ Results from Abaqus (U3)

$$diff_{\Delta} := \left(\frac{\Delta - \Delta_{FE}}{\Delta} \right) \cdot 100 = -5.439$$

Stresses

$\sigma_{applied} := \frac{P_{FE}}{As} = 320 \ MPa$ Stresses applied in FE-model

$M_{max} := P_{FE} \cdot a1 = 259.2 \ m \cdot kN$ Four point bending

$$z := \frac{hw}{2} = 0.25 \ m$$

$\sigma_{max} := \left(\frac{M_{max}}{I_R} \right) \cdot z = 202.747 \ MPa$ Stress at the top of the bottom flange

$\sigma_{FE} := 189.918 \ MPa$ Result from Abaqus (S11)

$$diff_{\sigma} := \left(\frac{\sigma_{max} - \sigma_{FE}}{\sigma_{max}} \right) \cdot 100 = 6.328$$

B Crack location of each specimen in the FE models

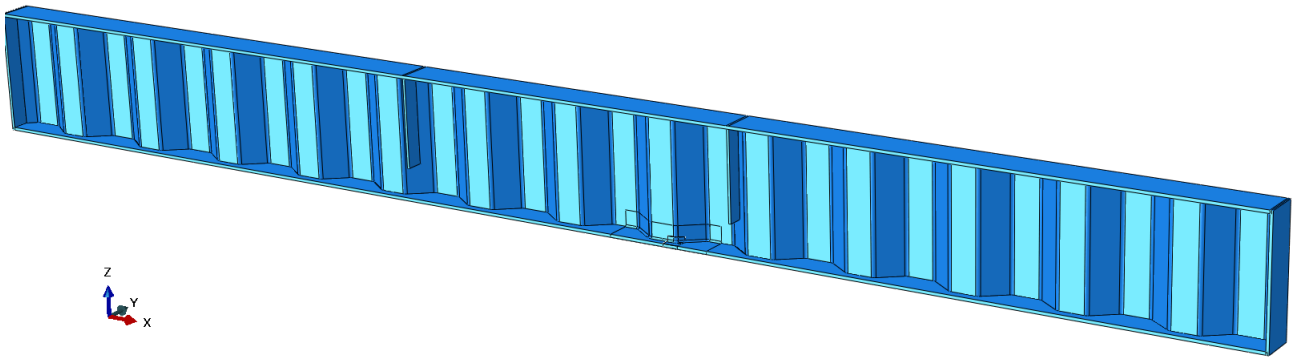

Figure B.1: *Crack location Ibrahim (2001).*

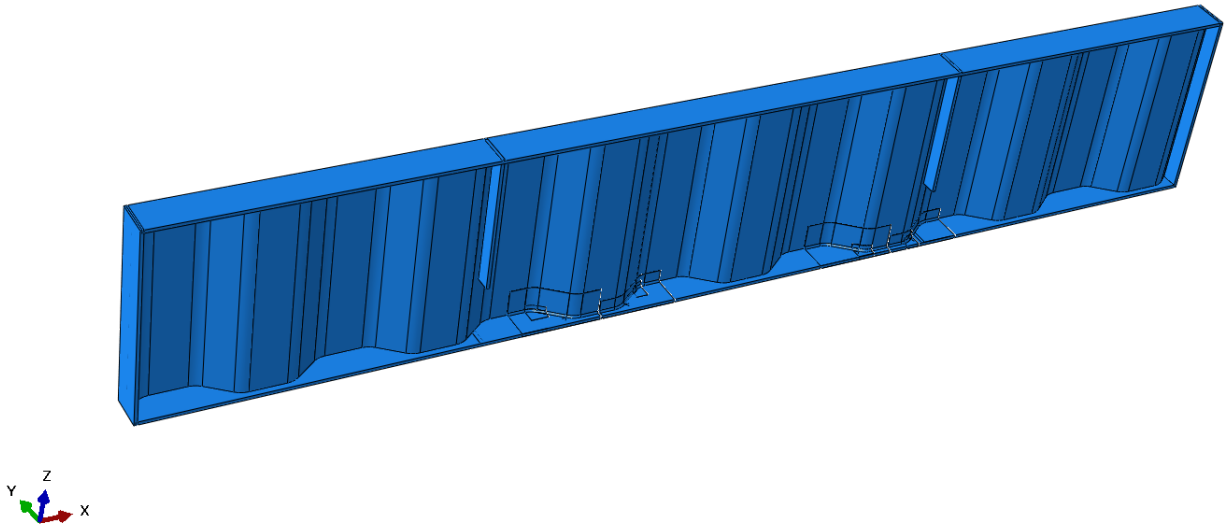

Figure B.2: *Crack location Sause et al. (2003).*

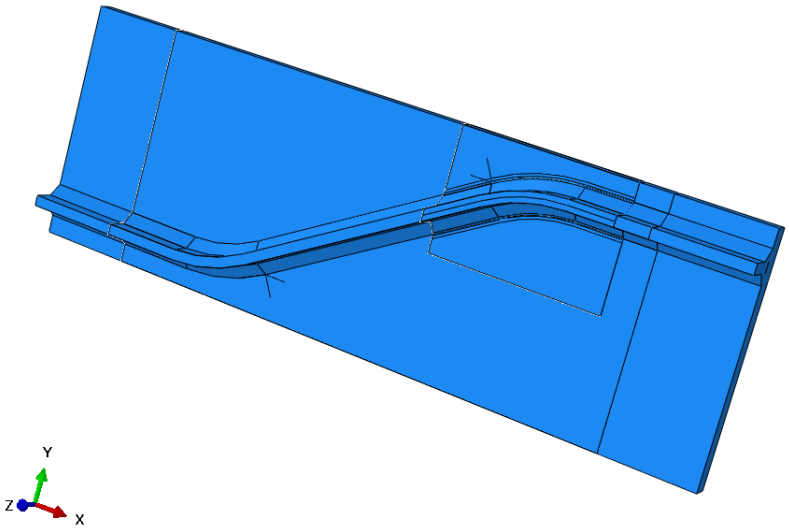

Figure B.3: *Crack location Wang et al. (2013) corrugation angle* 30°.

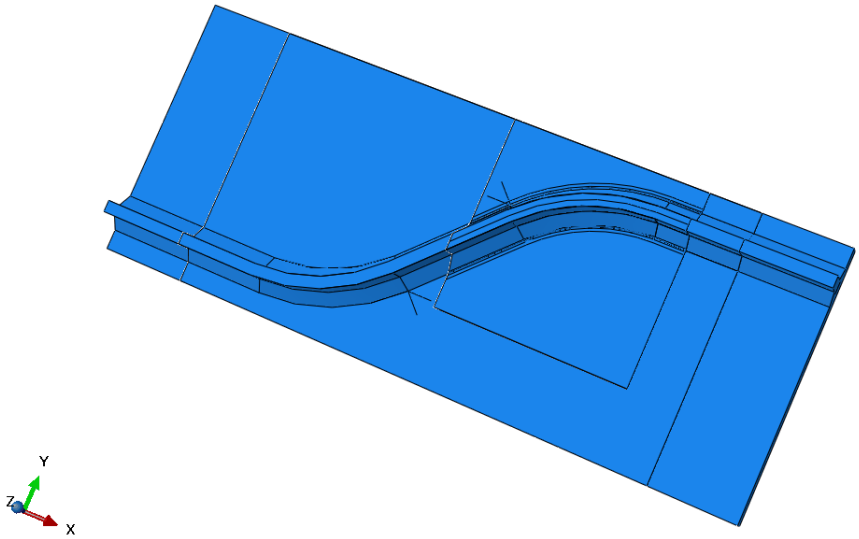

Figure B.4: *Crack location Wang et al. (2013) corrugation angle* 45°.

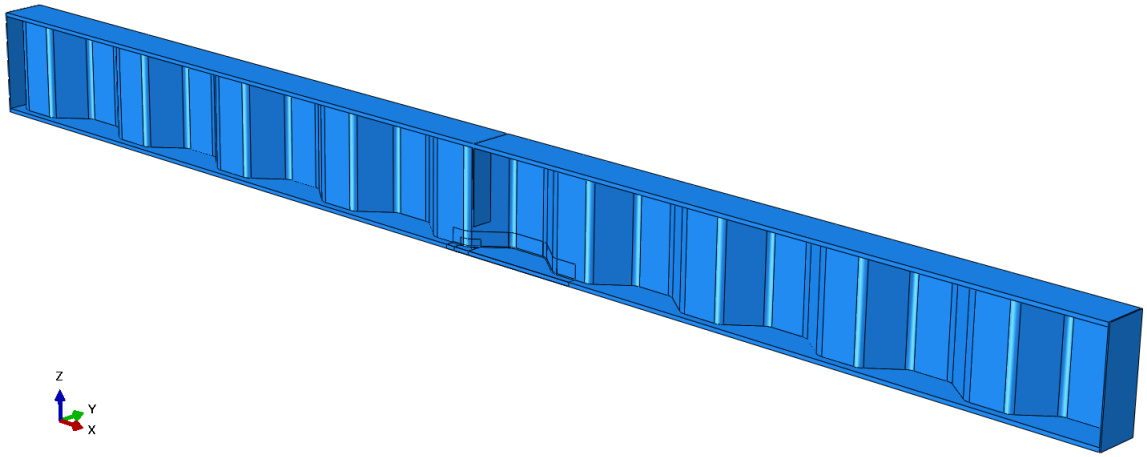

Figure B.5: *Crack location Kövesdi & Dunai (2014) weld size* 3*mm.*

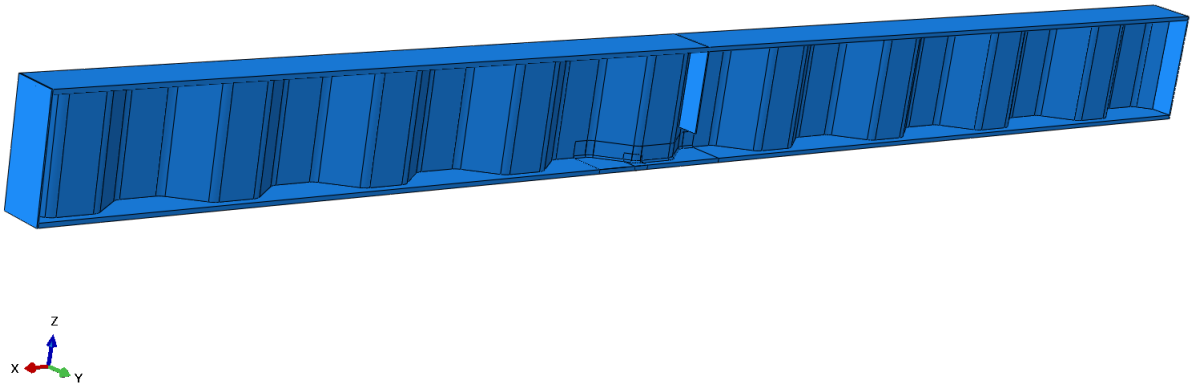

Figure B.6: *Crack location Kövesdi & Dunai (2014) weld size* 6*mm.*

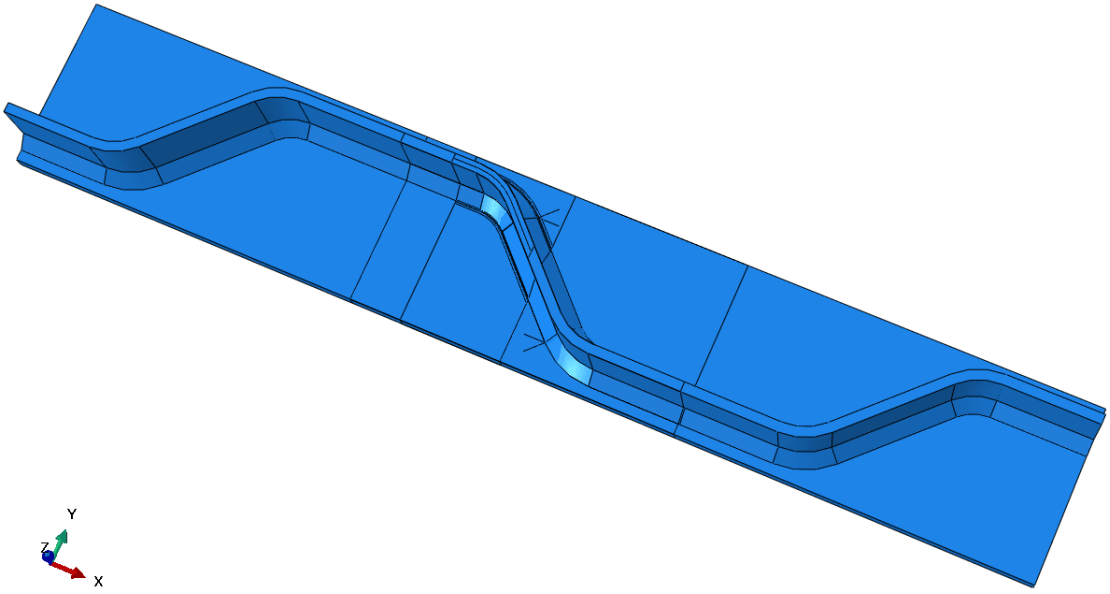

Figure B.7: *Crack location Tong et al. (2024) R*30.

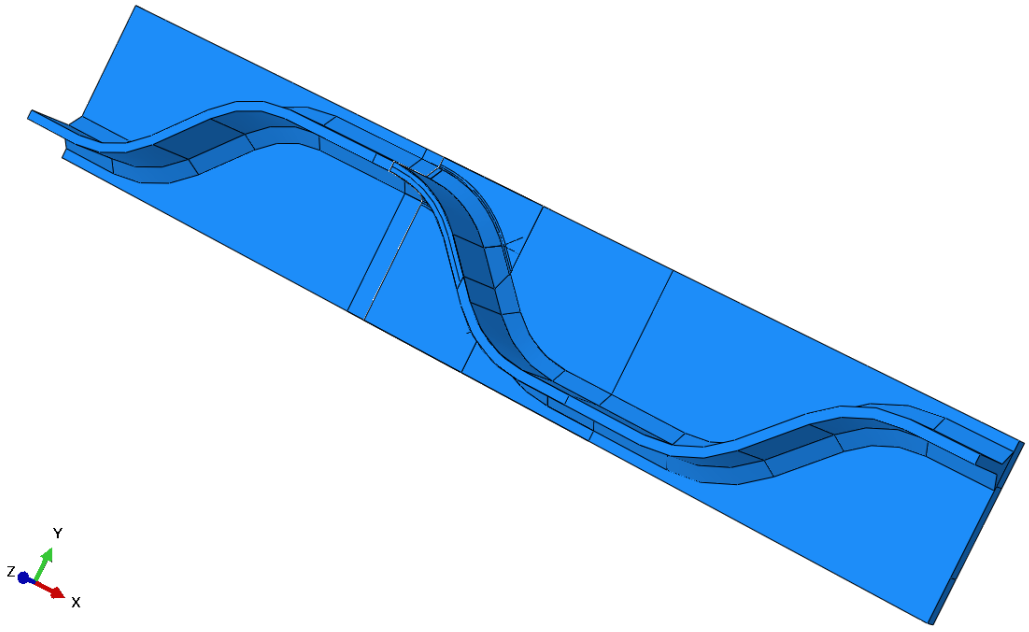

Figure B.8: *Crack location Tong et al. (2024) R*60.

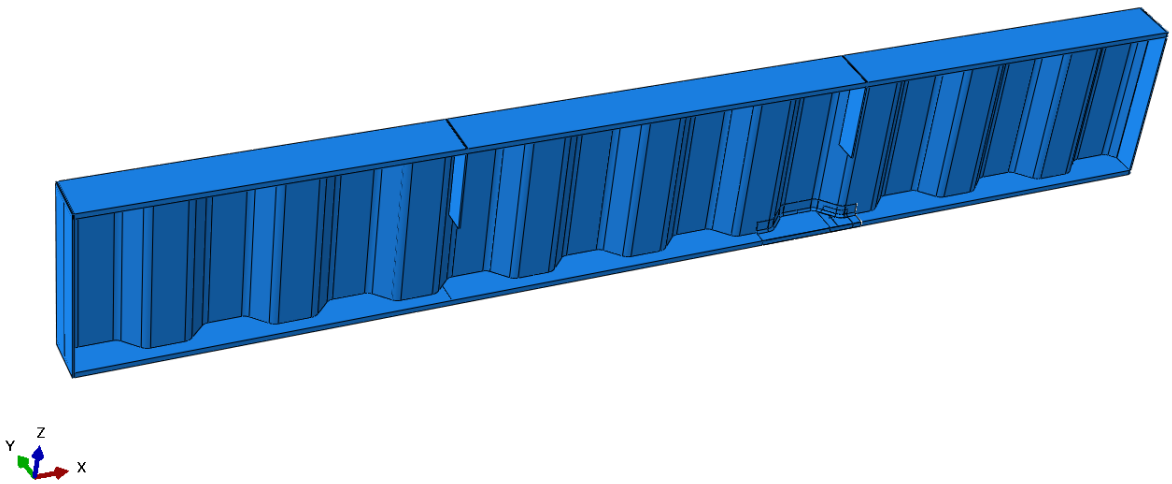

Figure B.9: *Crack location Tong et al. (2024) CWG.*

C All results obtained from numerical analysis

Table C.1: Stresses received from the experimental- and numerical analysis for each specimen.

Reference	Nf	Consider	sub-model (SHSS-model)				sub-sub-model (ENS-model)					Experiment	
			S11 [MPa]	S principal [MPa]	S'11 [MPa]	S'12 [MPa]	S principal [MPa]	S11 [MPa]	S'11 [MPa]	S'12 [MPa]	S von Mises [MPa]	Δσnom [MPa]	ΔσSHSS [MPa]
Ibrahim (200	2160000	0	0	0	0	0	0	0	0	0	0	0	
	1.8E+07	0	0	0	0	0	0	0	0	0	0	0	
	1595000	1	210.19	213.82	100.36	99.62	358.91	325.49	207.93	164.23	350.02	142.41	
	1806100	1	202.56	206.06	96.71	96.01	345.88	313.67	200.38	158.27	337.31	137.24	
	1235100	1	238.87	243.00	114.05	113.22	407.88	369.90	236.30	186.64	397.78	161.84	
	9339000	0	0	0	0	0	0	0	0	0	0	0	
Sause et al. (2003)	1418000	1	268.21	273.04	114.20	130.07	471.72	428.03	277.77	74.91	476.01	138.00	
	1448000	1	215.27	230.89	101.98	114.33	390.15	350.98	237.69	1.89	391.48	138.00	
	1304000	1	208.99	211.96	91.51	104.99	379.32	340.90	207.82	-182.97	381.56	138.00	
	2563000	1	183.80	186.18	76.66	90.24	321.06	297.68	178.28	157.42	324.77	103.00	
Wang et al. (2013), a30	2529298	1	204.71	209.46	66.85	89.57	268.57	247.13	113.14	2.53	273.06	138.36	
	2269865	1	206.13	210.91	67.32	90.19	270.43	248.85	113.93	2.55	274.95	139.32	
	1659587	1	233.96	239.38	76.41	102.37	306.94	282.44	129.31	2.89	312.07	158.12	
	1524053	1	233.96	239.38	76.41	102.37	306.94	282.44	129.31	2.89	312.07	158.12	
	1309182	1	241.62	247.22	78.91	105.72	317.00	291.70	133.55	2.99	322.29	163.31	
	1233105	1	241.07	246.66	78.73	105.48	316.27	291.03	133.24	2.98	321.55	162.93	
	1071519	1	250.11	255.91	81.68	109.44	328.14	301.95	138.24	3.09	333.62	169.04	
	997700	1	248.39	254.15	81.12	108.68	325.88	299.87	137.29	3.07	331.32	167.88	
	801678	1	263.72	269.83	86.13	115.39	345.98	318.37	145.76	3.26	351.77	178.24	
	928966	1	279.99	286.48	91.44	122.51	367.33	338.01	154.75	3.46	373.47	189.23	
	812831	1	278.70	285.16	91.02	121.94	365.64	336.46	154.04	3.45	371.75	188.36	
	866962	1	293.18	299.98	95.75	128.28	384.64	353.94	162.04	3.63	391.07	198.15	
	772681	1	293.18	299.98	95.75	128.28	384.64	353.94	162.04	3.63	391.07	198.15	
	726106	1	295.21	302.06	96.41	129.17	387.30	356.39	163.17	3.65	393.78	199.53	
Wang et al. (2013), a45	1918669	1	220.76	222.08	117.80	107.26	310.94	293.41	188.53	42.58	310.22	124.17	
	1674943	1	220.76	222.08	117.80	107.26	310.94	293.41	188.53	42.58	310.22	124.17	
	1315225	1	222.29	223.62	118.62	108.00	313.09	295.44	189.83	42.87	312.37	125.03	
	1210598	1	246.00	247.47	131.26	119.52	346.47	326.94	210.07	47.44	345.68	138.36	
	1039920	1	247.13	248.61	131.87	120.07	348.07	328.45	211.04	47.66	347.28	139.00	
	984011	1	246.00	247.47	131.26	119.52	346.47	326.94	210.07	47.44	345.68	138.36	
	901571	1	263.59	265.17	140.65	128.07	371.25	350.33	225.10	50.84	370.40	148.25	
	874984	1	263.59	265.17	140.65	128.07	371.25	350.33	225.10	50.84	370.40	148.25	
	792501	1	281.14	282.82	150.02	136.60	395.98	373.66	240.09	54.22	395.07	158.12	
	674528	1	291.69	293.44	155.65	141.72	410.84	387.68	249.10	56.26	409.90	164.06	
	561048	1	316.90	318.80	169.10	153.97	446.35	421.18	270.63	61.12	445.32	178.24	
	492040	1	316.90	318.80	169.10	153.97	446.35	421.18	270.63	61.12	445.32	178.24	
	417830	1	353.12	355.24	188.43	171.57	497.36	469.32	301.56	68.11	496.22	198.61	
	570164	1	353.12	355.24	188.43	171.57	497.36	469.32	301.56	68.11	496.22	198.61	
Kövesdi , Dunai (2014)	1310000	1	245.46	247.30	112.91	114.40	433.78	395.84	244.73	30.63	418.97	146.70	
	1326000	1	234.70	236.46	107.96	109.39	414.77	378.49	234.00	29.29	400.61	140.27	
	3272000	0	0	0	0	0	0	0	0	0	0	0	
Tong et al. (2024), CWG	1385900	1	202.27	204.11	113.08	99.72	391.60	358.17	257.28	60.51	390.05	115.50	
Tong et al. (2024), R30	320000	1	347.43	351.46	202.57	167.89	553.88	519.88	338.06	82.77	551.89	200	326
	370000	1	330.06	333.88	192.44	159.49	526.19	493.89	321.15	78.63	524.29	190	310
	789000	0	0	0	0	0	0	0	0	0	0	0	0
	763000	1	295.32	298.74	172.18	142.71	470.80	441.90	287.35	70.36	469.11	170	277
	972000	1	277.94	281.16	162.05	134.31	443.10	415.90	270.45	66.22	441.51	160	261
	1138000	1	269.26	272.38	156.99	130.11	429.26	402.91	261.99	64.15	427.71	155	253
	1140000	0	0	0	0	0	0	0	0	0	0	0	0
	3000000	0	0	0	0	0	0	0	0	0	0	0	0
	2280000	0	0	0	0	0	0	0	0	0	0	0	0
	3000000	0	0	0	0	0	0	0	0	0	0	0	0
Tong et al. (2024), R60	375000	1	302.78	339.29	169.75	147.97	517.92	438.62	266.83	4.75	466.46	200	308
	415000	1	290.66	325.72	162.96	142.05	497.20	421.07	256.15	4.56	447.81	192	296
	672000	0	0	0	0	0	0	0	0	0	0	0	0
	433000	1	278.55	312.15	156.17	136.13	476.48	403.53	245.48	4.37	429.15	184	283
	605000	1	264.93	296.88	148.53	129.47	453.18	383.79	233.47	4.15	408.16	175	270
	1059000	1	261.90	293.49	146.83	127.99	448.00	379.40	230.81	4.10	403.49	173	266
	1059000	1	249.79	279.92	140.04	122.07	427.28	361.86	220.13	3.92	384.83	165	254
	419000	0	0	0	0	0	0	0	0	0	0	0	0
	1028000	1	243.73	273.13	136.65	119.11	416.92	353.09	214.80	3.82	375.50	161	248
	1035000	1	236.17	264.65	132.40	115.41	403.98	342.12	208.13	3.70	363.84	156	240